Space radiation cancer risk projections and uncertainties - 2010. Cucinotta FA, Kim MH, Chappell LJ.
https://three-jsc.nasa.gov/articles/TP2011_216155.pdf. Date Posted: 08-10-2011.

NASA/TP-2011- 216155

Space Radiation Cancer Risk Projections and Uncertainties – 2010

Francis A. Cucinotta
NASA Lyndon B. Johnson Space Center
Houston, Texas

Myung-Hee Y. Kim and Lori J. Chappell
U.S.R.A., Division of Space Life Sciences
Houston, Texas

July 2011

Space radiation cancer risk projections and uncertainties - 2010. Cucinotta FA, Kim MH, Chappell LJ.
https://three-jsc.nasa.gov/articles/TP2011_216155.pdf. Date Posted: 08-10-2011.

THE NASA STI PROGRAM OFFICE . . . IN PROFILE

Since its founding, NASA has been dedicated to the advancement of aeronautics and space science. The NASA Scientific and Technical Information (STI) Program Office plays a key part in helping NASA maintain this important role.

The NASA STI Program Office is operated by Langley Research Center, the lead center for NASA's scientific and technical information. The NASA STI Program Office provides access to the NASA STI Database, the largest collection of aeronautical and space science STI in the world. The Program Office is also NASA's institutional mechanism for disseminating the results of its research and development activities. These results are published by NASA in the NASA STI Report Series, which includes the following report types:

- TECHNICAL PUBLICATION. Reports of completed research or a major significant phase of research that present the results of NASA programs and include extensive data or theoretical analysis. Includes compilations of significant scientific and technical data and information deemed to be of continuing reference value. NASA's counterpart of peer-reviewed formal professional papers but has less stringent limitations on manuscript length and extent of graphic presentations.

- TECHNICAL MEMORANDUM. Scientific and technical findings that are preliminary or of specialized interest, e.g., quick release reports, working papers, and bibliographies that contain minimal annotation. Does not contain extensive analysis.

- CONTRACTOR REPORT. Scientific and technical findings by NASA-sponsored contractors and grantees.

- CONFERENCE PUBLICATION. Collected papers from scientific and technical conferences, symposia, seminars, or other meetings sponsored or cosponsored by NASA.

- SPECIAL PUBLICATION. Scientific, technical, or historical information from NASA programs, projects, and mission, often concerned with subjects having substantial public interest.

- TECHNICAL TRANSLATION. English-language translations of foreign scientific and technical material pertinent to NASA's mission.

Specialized services that complement the STI Program Office's diverse offerings include creating custom thesauri, building customized databases, organizing and publishing research results . . . even providing videos.

For more information about the NASA STI Program Office, see the following:

- Access the NASA STI Program Home Page at http://www.sti.nasa.gov

- E-mail your question via the Internet to help@sti.nasa.gov

- Fax your question to the NASA Access Help Desk at (301) 621-0134

- Telephone the NASA Access Help Desk at (301) 621-0390

- Write to:
  NASA Access Help Desk
  NASA Center for AeroSpace Information
  7121 Standard
  Hanover, MD 21076-1320

Space radiation cancer risk projections and uncertainties - 2010. Cucinotta FA, Kim MH, Chappell LJ.
https://three-jsc.nasa.gov/articles/TP2011_216155.pdf. Date Posted: 08-10-2011.

NASA/TP-2011-216155

Space Radiation Cancer Risk Projections and Uncertainties – 2010

Francis A. Cucinotta
NASA Lyndon B. Johnson Space Center
Houston, Texas

Myung-Hee Y. Kim and Lori J. Chappell
U.S.R.A., Division of Space Life Sciences
Houston, Texas

July 2011

Space radiation cancer risk projections and uncertainties - 2010. Cucinotta FA, Kim MH, Chappell LJ.
https://three-jsc.nasa.gov/articles/TP2011_216155.pdf. Date Posted: 08-10-2011.

Available from:

NASA Center for AeroSpace Information
7121 Standard Drive
Hanover, MD 21076-1320

National Technical Information Service
5285 Port Royal Road
Springfield, VA 22161

This report is also available in electronic form at http://ston.jsc.nasa.gov/collections/TRS

Space radiation cancer risk projections and uncertainties - 2010. Cucinotta FA, Kim MH, Chappell LJ.
https://three-jsc.nasa.gov/articles/TP2011_216155.pdf. Date Posted: 08-10-2011.

Contents

Executive Summary viii

1. Introduction. 1
1.1 Basic Concepts 5

2. Space Radiation Environments and Transportation Models 8
2.1 Galactic Cosmic Ray Models 9
2.1.1 Model of galactic cosmic rays charge and energy spectra 9
2.1.2 Isotopic composition of galactic cosmic rays 10
2.1.3 Solar modulation of the galactic cosmic rays 12
2.2 Solar Particle Events 14
2.2.1 Hazard function for solar particle event occurrence 16
2.2.2 Representation of solar particle event energy distribution 18
2.3 Physics Model Description of Organ Exposures 20
2.3.1 Comparisons of ground-based measurements to transport codes 22
2.3.2 Intercomparisons of transport codes 24
2.3.3 Space flight measurement comparisons to transport codes 26
2.3.4 Predictions for exploration missions 30
2.4 Probability Distribution Function for Space Physics Uncertainties 33

3. Cancer Risk Projections for Low-linear Energy Transfer Radiation 35
3.1 Cancer Mortality and Incident Rates 36
3.2 Adjustment for Low Dose-rates 38
3.3 Comparisons of Tissue-specific Risk Models 39
3.4 Age at Exposure Dependence of Cancer 39
3.5 Radiation Risks for Never-smokers 43

4. Uncertainties in Low-linear-energy-transfer Risk Model Factors 49
4.1 Life-span Study Dosimetry Errors 50
4.2 Statistical Errors 50
4.3 Errors from Reporting Bias 51
4.4 Dose and Dose-Rate Effectiveness Factor Uncertainties 51
4.5 Transfer Models Uncertainties 53
4.6 Baseline Cancer Rates and Life-table Data 54
4.7 Summary of Past Uncertainty Analysis for Low-linear Energy Transfer Radiation 55

5. Cancer Risks and Radiation Quality 56
5.1 Review of Radiobiology Data for Relative Biological Effectivenesses 57
5.1.1 Relative biological effectivenesses from human epidemiology studies 57
5.1.2 Animal carcinogenesis studies with heavy ions 58
5.1.3 Cellular studies on chromosomal aberrations and mutation 60
5.1.4 Delayed effects from in-vivo and in-vitro studies 62
5.1.5 Dose-rate and protraction effects for high-energy and charge nuclei 62
5.2 Biophysical Considerations 63
5.3 Biophysical Models of Relative Biological Effectiveness 69
5.3.1 Relative biological effectiveness in the non-targeted effects model 72
5.3.2 Saturation mechanisms in biological responses 76
5.4 Risk Cross Sections and Coefficients 76

6. Revised NASA Model for Cancer Risks and Uncertainties 80
6.1 Track-structure-based Risk Model 82
6.2 Updates to Radiation Transport Codes 84
6.3 Effective Dose and Tissue Weights 86
6.4 Revised Uncertainty Assessment 89
6.4.1 Uncertainties for never-smoker risk estimates 93
6.4.2 Uncertainties Due to Non-targeted Effects 94
6.5 Considerations for Implementation of New Methods 95

7. Conclusions 97

8. References 101

Appendix A 114
Appendix B 118

Glossary

ACE	Advanced Composition Explorer
AGS	alternating gradient synchtron
AIC	Akaiki information criteria
ALARA	as low as reasonably achievable
AML	acute myeloid leukemia
AU	astronomical unit
BEIR	(NAS) Committee on the Biological Effects of Ionizing Radiation
BFO	blood-forming organ
BIC	Bayesian information criteria
BNL	Brookhaven National Laboratory
CA	chromosomal aberrations
CAD	computer-aided design
CAF	computerized anatomical female
CAM	computerized anatomical man
CAMERA	computerized anatomical man model
CBA	carcinoma-bearing animal
CDC	Centers for Disease Control
CI	confidence intervals
CL	confidence level
CME	coronal mass ejection
CNS	central nervous system
CRIS	cosmic ray isotope spectrometer
D	dose
DDREF	dose and dose-rate reduction effectiveness factor
DLOC	dosimetry location
DNA	deoxyribonucleic acid
DREF	dose-rate effectiveness factor
DSB	double-strand break
E	kinetic energy
EAR	excess additive risk
EB	Empirical Bayes
ELR	excess lifetime risk
ERR	excess relative risk
ET	extra-thoracic
F	fluence (number of ions per unit area ions/cm^2)
GCR	galactic cosmic rays
GEOS	geostationary environmental operational satellite
GERMCode	GCR Event-based Risk Model
GM	geometric mean
GLE	ground-level enhancement
GSD	geometric standard deviation
Gy	Gray
HZE	high-energy and charge
ICRP	International Commission on Radiological Protection
ISS	International Space Station
kbp	kilobase pairs
LAR	lifetime attributable risk
LEO	low-Earth orbit
LET	linear energy transfer

LIS	local interplanetary spectrum
LQ	linear-quadratic
LSS	Life-span Study (of the Japanese atomic-bomb survivors)
LTV	lunar transfer vehicle
MARIE	Martian Radiation Environment Experiment
MFISH	multicolor fluorescence in-situ hybridization
MLE	maximum likelihood estimate
MOLA	Mars orbiter laser altimeter
NAS	National Academy of Science
NCI	National Cancer Institute
NCRP	National Council of Radiation Protection and Measurements
NEO	near-Earth object
NGDC	National Geophysical Data Center
NIH	National Institutes of Health
NOAA	National Oceanographic and Atmospheric Agency
NRC	National Research Council
NS	never-smokers [used only in table]
NSCLC	non-small cell lung carcinoma
NSRL	NASA Space Radiation Laboratory
NTE	non-targeted effects
PDF	probability distribution function
PEL	permissible exposure limit
PRA	probabilistic risk assessment
Q	quality factor
QF	quality factor
$Q(L)$	quality factor as a function of LET
QMSFRC	quantum multiple scattering fragmentation model
R_0	low-LET risk coefficient per unit dose
RBE	relative biological effectiveness
RBE_{max}	maximum relative biological effectiveness that assumes linear responses at low doses or dose-rates
REIC	risk of exposure-induced cancer
REID	risk of exposure-induced death
RERF	Radiation Effects Research Foundation
RMAT	p. 22
RMS	root mean square
RR	relative risk
SCLC	small cell lung carcinoma
SD	standard deviation
SEER	surveillance, epidemiology, and end results
SPE	solar particle event
SRP	Space Radiation Program
SSA	Social Security Administration
SSB	single-strand break
TE	targeted effects
TEPC	tissue-equivalent proportional counter
TLD	thermoluminescent dosimeter
UNSCEAR	United Nations Special Committee on the Effects of Atomic Radiation
Z	charge number
Z^*	effective charge number

α	coefficient of linear dose response term, Gy^{-1}
β	coefficient of quadratic dose-response term, Gy^{-2}
$\phi_j(x,E)$	number of particles of type j with energy, E at depth, x in shielding, 1/(MeV/u cm^2)
λ_I	gender- and age-specific cancer incidence rate, cancers/y
λ_M	gender- and age-specific cancer mortality rate, cancer deaths/y
κ	parameter in action cross section to determine most biologically effects Z^{*2}/β^2
σ	action cross section or probability of effect per unit fluence, μm^2
Σ	track structure derived risk cross section, μm^2

Executive Summary

Uncertainties in estimating health risks from galactic cosmic rays are a major limitation to the length of space missions and the evaluation of potential risk mitigations. NASA limits astronaut exposures to a 3% risk of exposure-induced death (REID) and protects against uncertainties in risks projections using an assessment of 95% confidence intervals in the projection model. Revisions to the NASA projection model for lifetime cancer risks from space radiation and new estimates of model uncertainties are described in this report. Our report first reviews models of space environments and transport code predictions of organ exposures, and characterizes uncertainties in these descriptions. We then summarize recent analysis of low linear energy transfer (LET) radio-epidemiology data, including revision to the Japanese A-bomb survivor dosimetry, longer follow-up of exposed cohorts, and reassessments of dose and dose-rate reduction effectiveness factors (DDREFs). We compare these newer projections and uncertainties with earlier estimates made by the National Council of Radiation Protection and Measurements (NCRP). Current understanding of radiation quality effects and recent data on factors of relative biological effectiveness (RBE) and particle track structure are then reviewed. Recent results from radiobiology experiments from the NASA Space Radiation Laboratory provide new information on solid cancer and leukemia risks from heavy ions, and radiation quality effects are described. We then consider deviations from the paradigm of linearity at low doses of heavy ions motivated by non-targeted effects (NTE) models.

The new findings and knowledge are used to revise the NASA risk projection model for space radiation cancer risks. Key updates to the model are:

1) Revised values for low-LET risk coefficients for tissue-specific cancer incidence. Tissue-specific incidence rates are then transported to an average U.S. population and used to estimate the probability of risk of exposure-induced cancer (REIC) and REID.
2) An analysis of lung cancer and other smoking-attributable cancer risks for never-smokers that shows significantly reduced lung cancer risks as well as overall cancer risks compared to risk estimated for the average U.S. population.
3) Derivation of track-structure-based radiation quality functions that depend on charge number, Z, and kinetic energy, E, in place of a dependence on LET alone.
4) The assignment of a smaller maximum in the quality function for leukemia than for solid cancers.
5) The use of the International Commission on Radiological Protection tissue weights is shown to overestimate cancer risks from solar particle events (SPEs) by a factor of 2 or more. Summing cancer risks for each tissue is recommended as a more accurate approach to estimate SPE cancer risks. However, gender-specific tissue weights are recommended to define Effective doses as a summary metric of space radiation exposures.
6) Revised uncertainty assessments for all model coefficients in the risk model (physics, low-LET risk coefficients, DDREF, and quality factors [QFs]), and an alternative uncertainty assessment that considers deviation from linear responses as motivated by NTE models.
7) A probabilistic risk assessment (PRA) model for SPEs is described.

Results of calculations for the average U.S. population show more restrictive dose limits for astronauts above age 40 y compared to NCRP Report No. 132, a modest narrowing of uncertainties if NTEs are not included, and much broader uncertainties if NTEs are included. Risks for never-smokers compared to the average U.S. population are estimated to be reduced by more than 20% and 30% for males and females, respectively. Lung cancer is the major contributor to the reduction for never-smokers, with additional contributions from stomach, bladder, oral cavity,

and esophageal cancers. **Table 6.9** summarizes the revised estimates for the number of "safe days" in space at solar minimum for heavy shielding conditions. Results from previous estimates are compared to estimates for both the average U.S. population and a population of never-smokers. Greater improvements in risk estimates for never-smokers are possible, and would be dependent on improved understanding of transfer models for the histological types of lung cancer (for eg, small cell lung cancers and non-small cell lung cancer) as well as data on QFs for these types of lung cancers.

Table 6.9. Estimates of safe days in deep space, which are defined as the maximum number of days with 95% CL [confidence level] to be below the NASA 3%REID limit. Calculations are for solar minimum with 20 g/cm^2 aluminum shielding. Values in parenthesis are for alternative assessment that assumes additional constraints on QF uncertainties as given by Eq(6.7).

a_E, y	NASA 2005	NASA 2010 U.S. Avg. Population	NASA 2010 Never-smokers
		Males	
35	158	140 (186)	180 (239)
45	207	150 (200)	198 (263)
55	302	169 (218)	229 (297)
		Females	
35	129	88 (120)	130 (172)
45	173	97 (129)	150 (196)
55	259	113 (149)	177 (231)

The dependence of radiation QFs or risk cross sections on particle type and energy likely varies in a tissue-specific manner, with the mechanisms of cancer induction, cell killing, and other factors. An alternate uncertainty assessment that presumes a high level of constraint on the radiation quality dependences of cancer risk as determined by existing radiobiological data is described, and shown to reduce uncertainties (values shown in parenthesis in **Table 6.9**) significantly. Improvements in understanding of radiation quality effects and space physics is partially negated by higher dosimetry and statistical errors assessments from more recent human radiation epidemiology assessments compared to the prior NCRP estimates. In this report, example calculations for International Space Station missions and deep space missions to near-Earth objects, the moon, and Mars are described. Cancer risk for each location on the martian surface is also described, which should be valuable for mission planning. The uncertainty assessments made in this report are an important component of the PRAs that are essential for exploration missions.

1. Introduction

Exposures to astronauts from galactic cosmic rays (GCR) — made up of high-energy protons and high-energy and charge (HZE) nuclei, and solar particle events (SPEs) — that are comprised largely of low- to medium-energy protons are a critical challenge for space exploration. Experimental studies have shown that HZE nuclei produce both qualitative and quantitative differences in biological effects compared to terrestrial radiation,[1-5] leading to large uncertainties in predicting exposure outcomes to humans. Radiation risks include carcinogenesis,[6] degenerative tissue effects such as cataracts[7,8] or heart disease,[9-11] and acute radiation syndromes.[6] Other risks, such as damage to the central nervous system (CNS), are a concern for HZE nuclei.[1,5] For International Space Station (ISS) missions and design studies of exploration of the moon, near-Earth objects (NEOs), and Mars, NASA uses the quantity risk of exposure-induced death (REID) to limit astronaut risks. A REID probability of 3% is the criteria for setting age- and gender-specific exposure limits, while protecting against uncertainties in risk projection models is made using estimates of the upper 95% confidence level (CL).

Risk projection models serve several roles, including: setting the age- and gender-specific exposure-to-risk conversion factors needed to define dose limits, projecting mission risks, and evaluating the effectiveness of shielding or other countermeasures. For mission planning and operations, NASA uses the model recommended in NCRP [National Council of Radiation Protection and Measurements] Report No. 132 to estimate cancer risks from space.[6] The model employs a life-table formalism to model competing risks in an average population, epidemiological assessments of excess risk in exposed cohorts such as the atomic-bomb survivors, and estimates of dose and dose-rate reduction factors (DDREFs) and linear energy transfer (LET)-dependent radiation quality factors (QFs) to estimate organ dose equivalents.

NASA recognizes that projecting uncertainties in cancer risk estimates along with point estimates is an essential requirement for ensuring mission safety, as point estimates alone have limited value when the uncertainties in the factors that enter into risk calculations are large. Estimates of 95% confidence intervals (CI) for various radiation protection scenarios are meaningful additions to the traditional point estimates, and can be used to explore the value of mitigation approaches and research that could narrow the various factors that enter into risk assessments. **Figure 1.1** illustrates the approach used at NASA as the number of days in space or an astronaut's career exposure accumulates. Because of the penetrating nature of the GCR and the buildup of secondary radiation in tissue behind practical amounts of all materials, we argued previously[12-14] that improving knowledge of biological effects to narrow CI is the most cost-effective approach to achieve NASA safety goals for space exploration. Furthermore, this knowledge is essential to perform cost-benefit analysis of mitigation measures, such as shielding approaches and biological countermeasures, and to practice the safety requirement embodied in the principle of as low as reasonably achievable (ALARA).

Uncertainties for low-LET radiation, such as γ-rays or x rays, have been reviewed several times in the past, and indicate that the major uncertainty is the extrapolation of cancer effects data from high to low doses and dose-rates.[15,16] The (National Academy of Science [NAS]) Committee on the Biological Effects of Ionizing Radiation (BEIR) VII[16] and United Nations Special Committee on the Effects of Atomic Radiation (UNSCEAR) committees[17] recently provided new assessments of low-LET radiation risks. Uncertainties consist of the transfer of risk across populations and the sources of error in epidemiology data, including dosimetry, recording bias, and statistical errors. Probability distribution functions (PDFs), described previously,[15] were used to estimate low-LET risk uncertainties. For space radiation risks, additional uncertainties occur related to

estimating the biological effectiveness of hydrogen, helium, and HZE nuclei, and to predicting particle energy spectra at tissue sites.[12] The limited understanding of heavy ion radiobiology is the largest contributor to the uncertainty for space radiation effects.[1,12]

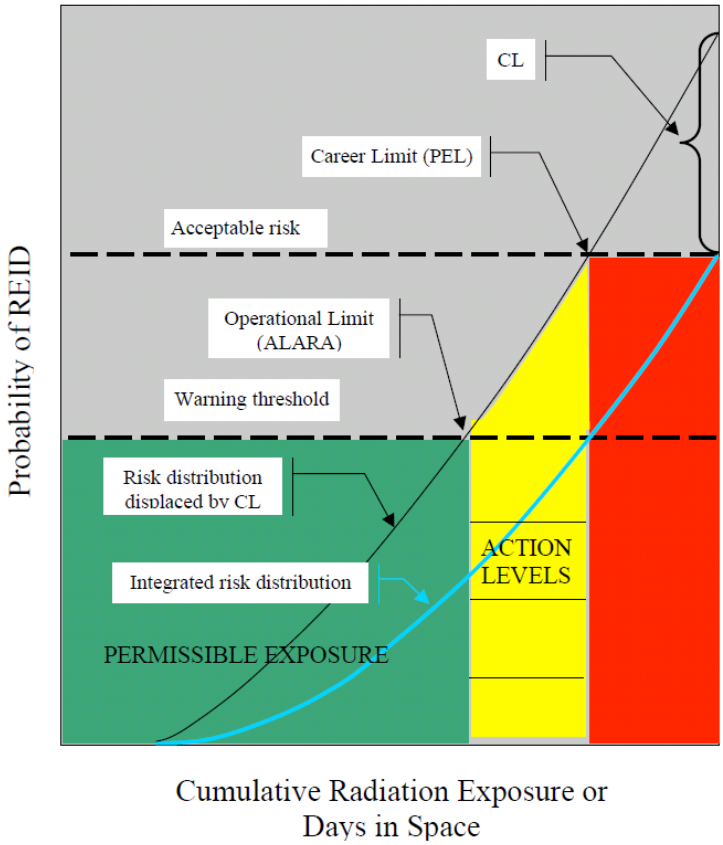

Figure 1.1. Risk management with ALARA and large uncertainties. The cumulative risk distribution function for an "acceptable" level of risk is displaced, so that the permissible exposure limit (PEL) is based on the 95% CL to take into account the uncertainties in projection models. ALARA practices and action levels are then also displaced dependent on the level of uncertainties.[18]

We discuss in this report modifications to the NASA model, which projects cancer risks and probability distributions that describe uncertainties for space missions, and apply the model to several exploration mission scenarios. Our estimates use REID as the basic risk quantity rather than excess lifetime risk (ELR) or lifetime attributable risk (LAR) to adjust for competing risks as well as for cancer deaths moved earlier in time by radiation.[19] To improve the transfer of cancer rates derived from exposed populations to a population of astronauts, we describe incidence-based risk transfer models and project mortality risks using adjustments between cancer mortality and incidence in the U.S. population as recommended by the BEIR VII report.[16] The impacts of smoking on population rates are assessed to make risk estimates for a population of never-smokers. Previous risks assessments was based on the use of a single parameter, LET, to describe the relative biological effectiveness of all cosmic rays with no specific dependence on charge number of velocity. LET is known to be a poor descriptor of energy depiction on a microscopic scale. A key hypothesis to our revised approach is that, to improve the extrapolation of radiobiological data and to optimize uncertainty reduction, greater emphasis on particle track

structure in describing energy deposition and subsequent biological events at the molecular, cellular, and tissue levels is required. We describe data and theoretical analysis that support the redefinition of radiation quality in terms of track structure parameters, and the assignment of distinct radiation QFs for solid cancer and leukemia with significantly lower values recommended for leukemia compared to solid cancer. The relationship between event- and fluence-based models and organ dose equivalent approaches is discussed.

We used Monte-Carlo simulations of subjective PDFs that represent current knowledge of factors that enter into risk assessments[2,12,15,20] to propagate uncertainties across multiple contributors. We can write a risk equation in a simplified manner as a product of several factors including the dose, D, quality factor, Q, a low-LET risk coefficient normally derived from the data of the atomic-bomb survivors, R_0, and the dose and dose-rate reduction effectiveness factor, *DDREF*, that corrects risk data for dose-rate modifiers. Monte-Carlo uncertainty analysis uses the risk equation, but the equation is modified by normal deviates that represent subjective weights and ranges of values for various factors that enter into a risk calculation. First, we define $X \in R(x)$ as a random variate that takes on quantiles $x_1, x_2, \ldots, x_n$ such that $p(x_i) = P(X=x_i)$ with the normalization condition $\Sigma\, p(x_i)=1$. $C(x_i)$ is defined as the cumulative distribution function, $C(x)$, which maps X into the uniform distribution $U(0,1)$, and we define the inverse cumulative distribution function $C(x)^{-1}$ to perform inverse mapping of $U(0,1)$ into x: $x=C(x)^{-1}$. Then we write for a simplified form of the risk equation for a Monte-Carlo trial, ξ:

$$Risk_{\xi} \quad = \quad R_0(age, gender)\frac{FLQ}{DDREF}\left\{\frac{x_{R_0}x_{phys}x_Q}{x_{D_R}}\right\}_{\xi} \tag{1.1}$$

where R_0 is the low-LET risk coefficient per unit dose, the absorbed dose, D, is written as the product of the particle fluence, F, and LET, L, and Q is the radiation QF. The x_R, x_{phys}, x_{Dr}, *and* x_Q are quantiles that represent the uncertainties in the low-LET risk coefficient, space physics models of organ exposures, dose-rate effects, and radiation quality effects, respectively. Monte-Carlo trials are repeated many times, and resulting values are binned to form an overall PDF taking into account the model uncertainties. In this report, updates to the risk coefficients and QFs as well as and the revised PDFs for the various factors are described based on recent data and findings. In practice, the risk model does not use the simple form of Eq(1.1). Instead, risk calculations are based on a double-detriment life-table calculation that considers age, gender, and tissue-specific, radiation-induced cancer rates within a competing risk model with all causes of death in an average population.[6,17]

The model of Eq(1.1) and similar models make several important assumptions that we note here:

1) Risk assessments are population-based calculations that are applied to individuals rather than individual-based calculations. Legal and ethical obstacles to individual-based risk assessment are being described elsewhere along with the current scientific limitations to such approaches for low dose-rate exposures .[21,22]
2) A linear and additive response over each the contribution of each particle to cumulative risk is assumed. The linearity and additivity of radiation component assumptions are embodied in the use of QFs, Q. QFs are subjective judgments of experimental determinations of maximum relative biological effectiveness (RBE) factors determined as the ratio of initial slopes for linear dose response curves for ions compared to γ-rays denoted as RBE_{max}. Under this assumption, the DDREF applies only to γ-rays. No dependence of space radiation risks on dose-rate is presumed.

3) The risk model implicitly assumes that only quantitative differences between low- and high-LET radiation are important for risk assessment, thereby neglecting any impacts from qualitative differences.

Ground-based research at the NASA Space Radiation Laboratory (NSRL) continues to document important quantitative and qualitative differences in the biological effects of HZE nuclei, including in the types of deoxyribonucleic acid (DNA) damages and chromosomal arrangements, gene expression, and signal transduction induced by radiation. Important differences between these processes at high vs. low doses have also been documented. Non-targeted effects (NTE), including bystander effects and genomic instability in the progeny of irradiated cells,[23,24] are currently of great interest in radiation protection as they challenge the traditional paradigm of dose responses, which increase in a manner proportional to dose without threshold. These assumptions are clearly motivated by a DNA mutation mechanism or other targeted DNA effects (targeted effects [TE]). NTEs often are suggestive of qualitative differences between low- and high-LET radiation. Ultimately, low-LET and simulated space radiation can be compared for the same endpoint, such as overall cancer risk or tissue-specific cancer risks, albeit there are both qualitative and quantitative differences in causative steps leading to these endpoints. However, elucidation of the biological importance of quantitative differences through mechanistic research is essential for improving current risk models. A long-time outstanding question is the use of dose-based models to describe cosmic-ray tracks as they pass through tissue. **Figure 1.2** illustrates some of the differences between dose-based risk models and particle track structure. Quantitative and qualitative differences occur, and the use of radiation QFs may not be justified in all or certain cases.

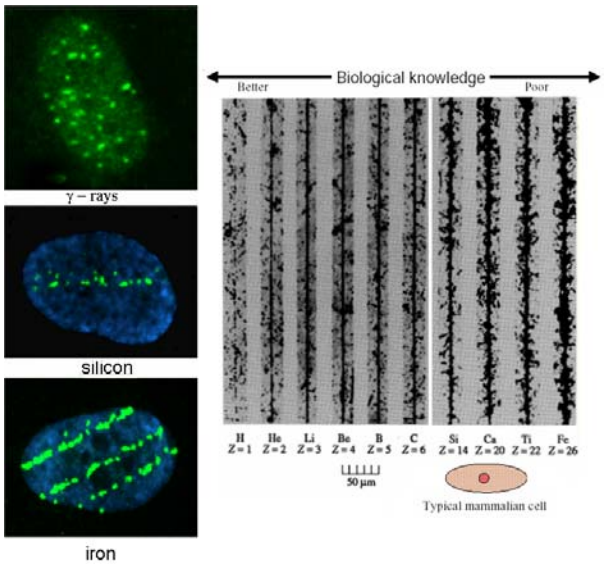

Figure 1.2. A comparison of particle tracks in nuclear emulsions and human cells. The right panel illustrates tracks of different ions, from protons to iron, in nuclear emulsions, clearly showing the increasing ionization density (LET=ΔE/Δx) along the track by increasing the charge Z. The left panel shows three nuclei of human fibroblasts exposed to γ-rays and Si- or Fe-ions, and immunostained for detection of γ-H2AX[14]. Each green focus corresponds to a DNA double-strand break (DSB). While the H2AX foci in the cell that is exposed to sparsely ionizing γ-rays are uniformly distributed in the nucleus, the cells that are exposed to HZE particles present DNA damage along tracks (one Si- and three Fe-particles, respectively), and the spacing between DNA DSB is reduced at very high LET.[2]

NASA radiation protection methods are based on recommendations issued by the NCRP[6,25] and the International Commission on Radiological Protection (ICRP)[26], but independent approaches have been developed and continue to be developed that lead to better implementation in the context of space exploration. In those instances, details of NASA practice differ from these recommendations. For example, NASA uses cancer-mortality-based career limits rather than limits that are based on overall health detriment, as recommended by the ICRP, and gender-specific career limits calculated for individual astronaut mission exposure histories rather than attained age. Distinct short-term limits are followed originating in recommendations from the National Research Council (NRC) (1970). NASA continued to use $Q(L)$ (ie, QF as a function of LET) rather than ICRP radiation weighting factors based on NCRP recommendations,[6,25] and also uses distinct RBEs for non-cancer risks instead of the QFs employed in estimating cancer risks. NASA estimates the 95% CLs as a requirement for dose limits, and recently considered limits for the CNS and heart disease.[27] Dosimetry[28] and ALARA implementation for space missions, including the timing of spacewalks,[29] and operational biodosimetry[30] also distinguish NASA procedures from terrestrial radiation protection procedures.

While the revised approach described in this report for space radiation cancer risk assessments leads to additional modifications from prior methods recommended by NCRP or ICRP; it is nevertheless consistent with the overall principles of NCRP and ICRP because the higher risk levels of long-term space missions require more accurate assessments than are used in most ground-based scenarios. To quote the ICRP from its recent assessment of QFs:[31]

> *"Accurate determinations may seem to be an academic issue in radiation protection. Under routine circumstances, where exposures are substantially below the limits, this is indeed the case. Then there is no need for accurate assessments. However, in radiological protection, as in other formally adopted and legally binding protection or safety systems, a limit must also be rigorously defined quantity because exposures must, in certain critical cases, be assessed accurately. Looseness that can involve uncertainties by a factor of 2 or more is tolerable under many routine conditions, but it will make the system inoperable in exactly those critical circumstances where compliance with regulatory limits is in question and must be reliably quantified."* [p. 68, para. 230]

Thus, the required accuracy for radiation projection for long-term space travel makes many of the methodologies recommended by the ICRP and the NCRP inadequate for NASA. However, the approach described in the present report is consistent with the NCRP overall recommended principles of risk justification, risk limitation, and ALARA. In the final section of this report, we will discuss predictions for space missions as well as changes to dosimetry and computer codes procedures that result from our recommended changes to the NASA cancer projection model.

1.1 Basic Concepts

Radiation exposures are often described in terms of the physical quantity absorbed dose, D, which is defined as the energy deposited per unit mass. Dose has units of Joule/kg that define the special unit, 1 Gray (Gy), which is equivalent to 100 rad (1 Gy = 1 rad). In space, each cell within an astronaut is exposed every few days to a nuclear particle that comprises the GCR. The GCR is the nuclei of atoms accelerated to high energies in which the atomic electrons are stripped off. It is common to discuss the number of particles per unit area, called the fluence, F, with units of $1/cm^2$. As particles pass through matter, they lose energy at a rate dependent on their kinetic energy, E, and charge number, Z, and approximately the average ratio of charge to

mass, (Z_T/A_T) of the materials they traverse. The rate of energy loss is called the LET, which, for unit density materials such as tissue, is given in units of keV/μm. Dose and fluence are related by $D = \rho F LET$, where ρ is the density of the material (eg, 1 g/cm^3 for water or tissue). The dependence of energy loss on the Z_T/A_T ratio implies that hydrogen, with its ratio equal to 1, is the optimal material for slowing particles. There is a broad energy range for the cosmic rays, and the spectra of particles is denoted as the fluence spectra, $\phi_j(E)$, where j refers to the particle type described by Z and the mass number, A. The particle velocity scaled to the speed of light, denoted as β, is related to the kinetic energy. E and β are related using the formula $\gamma=1 + E/m$ where m is the nucleon rest mass (938 MeV) and $\beta=(1-1/\gamma^2)^{-1/2}$. Kinetic energies are often expressed in units of MeV per atomic mass unit (u), MeV/u because particles with identical E then have the same β. The total kinetic energy of the particle is then A times E.

The GCR of interest has a charge number, Z from 1 to 28, and energy from less than 1 MeV/u to more than 10 000 MeV/u with a median energy of about 1000 MeV/u. The GCR with energies less than about 2000 MeV/u is modulated by the 11-y solar cycle, with more than two times higher GCR flux at solar minimum when the solar wind is weakest compared to the flux at solar maximum. The most recent solar minimum was in 2008-2009, and the next will occur in about 2019. SPEs occur about 5 to 10 times per year, except near solar minimum, and consist largely of protons with kinetic energies below 1 MeV up to a few hundred MeV. However, most SPEs lead to small doses (<0.01 Gy) in tissue; and only a small percentage (<10%) would lead to significant health risks if astronauts were not protected by shielding. At this time there is very little capability to predict the onset time and determine whether a large or small SPE will occur until many hours after an SPE has commenced. Mission disruption many thus occur for many SPEs, although the health risks are very small.

Nuclear and atomic interactions in materials are best described using the material thickness, x, described as an areal density, $t = x\rho$, where ρ is the atomic density of the material with values for common materials of ρ = 1.0, 2.7, and 0.96 for tissue, aluminum, and high-density polyethylene, respectively. The range of a particle is defined as the average distance traveled before the particle loses all of its kinetic energy and stops. The range increases with E and is a few g/cm^2 at 50 MeV/u, and more than 100 g/cm^2 at 1000 MeV/u. Nuclear reactions, which occur through interactions of cosmic rays with the nuclei of atoms in shielding materials or tissue, lead to the production of secondary radiation, including neutrons and charged particles from the atoms of the shielding material or tissue. The mean free path for a nuclear reaction increases with the mass of the cosmic ray; about 10 g/cm^2 for heavy nuclei such as iron (A=56; Z=26), and more than 20 g/cm^2 for protons (A=1; Z=1). Shielding thickness of 10 to 20 g/cm^2 is sufficient to protect against most SPEs; however, thicknesses of several hundred g/cm^2 are needed to significantly reduce organ doses from GCR, making shielding impractical as an efficient method of protection.

Energy loss by cosmic rays occurs through ionization and excitation of target atoms in the shielding material or tissue. The ionization of atoms leads to the liberation of electrons that often have sufficient energy to cause further excitations and ionizations of nearby target atoms. These electrons, which are called δ-rays, can have energies more than 1 MeV for ions with E>1000 MeV/u. About 80% of the LET of a particle is due to ionizations leading to δ-rays. The number of δ-rays created is proportional to Z^{*2}/β^2, where Z^* is the effective charge number that adjusts Z by atomic screening effects important at low E and high Z. The lateral spread of δ-rays, called the track-width (illustrated in **Figure 1.2**) of the particle, is dependent on β but not on Z being determined by kinematics. At 1 MeV/u, the track-width is about 100 nm (0.1 μm); and at 1000 MeV/u, the track-width is about 1 cm. A phenomenological approach to describing atomic ionization and

excitation is to introduce an empirical model of energy deposition. Some definition of a characteristic target volume is needed to apply this model. A diverse choice of volumes is used in radiobiology, including volumes with diameters <10 nm to represent short DNA segments, and of diameters from a few to 10 microns to represent cell nuclei or cells. Energy deposition is the sum of energy transfer events due to ionizations and excitations in the volume including those from δ-rays. For large target volumes, energy deposition and energy loss (LET) become approximately the same. Two particles with different Z and identical LET will have different values for E and, therefore, different track-widths. The particle with lower Z will have a narrower track-width and more localized energy deposition, and in many experiments has been shown to be have a higher biological effectiveness than a particle with higher Z. In tissue, however, the higher Z nuclei often have a larger range and can traverse more cell layers than the lower Z nuclei at the same LET.

The biological effects of different types of particles are usually compared using the ratio of doses that leads to an identical effect. This ratio is called the RBE factor. Human data for low-LET radiation, such as γ-ray or x-ray exposures leading to increased cancer risk, have been studied in the survivors of the atomic-bombs in Japan during World War II, medical patients exposed therapeutically to radiation, and nuclear reactor works. However, there are no human data for high-LET radiation such as cosmic rays with which to make risk estimates. Therefore, RBEs in which the dose in the numerator is that of γ-rays and the dose in the denominator of a nuclear particle being studied, are often used to compare results from biological experiments with nuclei created at particle accelerators to the results of epidemiological studies in humans exposed to γ-rays or x rays. RBEs vary widely with the biological endpoint, cell or animal system, type of radiation, and doses used in experiments. Traditionally, it has been the role of advisory panels to make a subjective judgment of available RBE data to make estimates for human risk. Such judgment is used to define a radiation QF. For terrestrial radiation exposures QFs, Q has been defined uniquely by LET, Q(LET). Values of Q from 1 to 30 have been used in the past for different LET values with Q=1 below 10 keV/μm and Q=30 at 100 keV/μm used at this time. For the more complex radiation environments in space, however, the inaccuracy of LET as a descriptor of biological effects has been a long-standing concern. Multiplication of the absorbed dose by the QF is referred to as the dose equivalent, $H = Q(LET)\ D$, which has units denoted as 1 Sv (1 Sv = 100 rem; of 1 mSv = 0.1 rem). For calculating cancer risks, radiation transport codes are used to describe the atomic and nuclear collisions that occur inside spacecraft and tissue. Resulting particle spectra, averaged over the tissues of concern for cancer risk (eg, lung, stomach, colon, bone marrow, etc.), are used to describe the organ dose equivalent, H_T.

Because human epidemiological data are predominantly for high dose-rates, methods to estimate cancer risks at low dose-rates are needed. The traditional approach to this problem has been to estimate a DDREF that reduces the high dose-rate risk estimate for its application to low dose and dose-rates. DDREF values from 1.5 to 2.5 have been recommended in the past. The use of radiation QFs and DDREFs is a major concern for space radiation risks because there are both quantitative and qualitative differences observed in experimental systems of cancer risks. It is unclear whether these quantities are sufficiently accurate to form a basis for risk estimates. NASA limits astronaut cancer risks to a lifetime REID of 3%. Because long space missions are projected to approach and exceed this risk limit, uncertainty analyses of the models and methods used to make risk estimates are performed, including values and descriptions of H_T, Q, and DDREF, which is the focus of this report.

2. Space Radiation Environments and Transport Models

In this section, we review models of the space radiation environments and organ exposures as well as recent developments in their physical characterization in support of human missions. To characterize uncertainties in physics models of space radiation the kinetic energy (*E*), mass number (*A*), and charge number (*Z*), the dependent fluence distribution *F(E,A,Z)* behind spacecraft and tissue shielding must be evaluated. The space physics uncertainty for estimating particle fluence distributions, *F(E,A,Z)*, at tissues of interest behind shielding has three components: space environments(x_{env}), radiation transport(x_{tran}), and spacecraft and tissue shielding descriptions (x_{shield}). Overall uncertainties contributing to Monte-Carlo trial, ξ can be written as:

$$F_{\xi}(E,A,Z) \quad = \quad F_M(E,A,Z)x_{env}x_{tran}x_{shield} \tag{2.1}$$

where F_M is a baseline model for the fluence distribution at sensitive tissues that is being estimated. We review each of these factors in the current section. There are also variability considerations to be addressed when considering organ exposures from space radiation. These variables include: orientation of crew members inside a vehicle, peculiarities of an individual's size and composition relative to the standard human geometry model used in calculations or perhaps phantom measurements, or the exact position in which a crew member's dosimetry is worn. Variability analysis can be made, employing similar methods to those used here for uncertainty analysis,[32] and considered in future reports.

The types and energies of particle radiation in space are summarized in **Figure 2.1**. The predominant types of particle radiation in the Earth environment are solar flare protons, trapped protons and electrons, and GCR. There are temporal variations as well as spatial distributions for each radiation source.

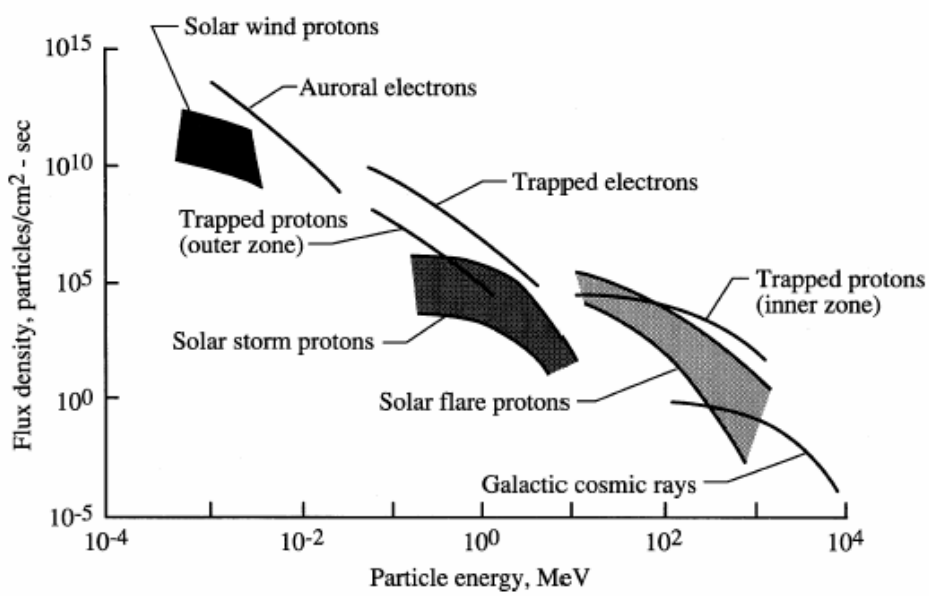

Figure 2.1. Schematic of energy ranges of space radiation environments.[33]

It is convenient to consider the particulate radiation in space as arising from these distinct sources as defined by their location: the solar particle radiation, the GCR, and the trapped particle radiation. We consider models of GCR and SPE next. The trapped radiation makes no contribution outside of low-Earth orbit (LEO) and only a very minor contribution for ISS organ exposures because here GCR dominates, representing more than 80% of organ dose equivalents.[30,34] The uncertainties in the trapped environments are not described here.

2.1 Galactic Cosmic Ray Models

The GCR pervades the near-Earth environment omnidirectionally, and has a range of energies that exceeds 10 GeV/u. The GCR consists of fully ionized nuclei because the electrons are stripped from the atoms during the acceleration of ions to high energies. Most cosmic rays probably originate in our galaxy, especially in supernova explosions,[35,36] although the highest energy components ($\geq 10^{17}$ eV amu^{-1}) may be of extragalactic origin.[37] The region outside the solar system in the outer part of the galaxy is believed to be filled uniformly with GCR. The GCR nuclei constitute approximately one third of the energy density of the interstellar medium and, on a galactic scale, form a relativistic gas whose pressure is important to take into account in the dynamics of galactic magnetic fields. GCR nuclei are the only direct and measurable sample of matter from outside the solar system. It is a unique sample since it includes all of the elements, from hydrogen to the actinides. The GCR arriving beyond the Earth magnetic field at the distance of the Earth from the sun (1 AU [astronomical unit]) is composed of approximately 98% nuclei and approximately 2% electrons and positrons.[38] In the energy range 10^8 to 10^{10} eV/u, where it has its highest intensity, the nuclear component consists roughly of 87% protons, approximately 12% helium nuclei, and a total of approximately 1% for all heavier nuclei from carbon to the actinides.[38]

Although GCR probably includes every natural element, not all GCR are important for space radiation protection purposes. The elemental abundances for species heavier than iron (atomic charge number $Z > 26$) are typically 2 to 4 orders of magnitude smaller than the elemental abundance for iron.[38] some elements such as the L nuclei (Li, Be, B), F, and several nuclei between Si and Fe are quite rare[38,39] in the solar system; whereas in the GCR flux, nuclei of these elements are present nearly as commonly as those of their neighbors. This shows that the GCR originates in the breakup of heavy particles during GCR propagation, which would not be present in the GCR at stellar sources.[40,41]

Experimental studies of high-charge (Z) and energy (E) nuclei (HZE) were made on the Pioneer, Voyager, and Ulysses spacecraft to measure the isotopic composition of GCR elements near Earth and in deep space.[40,42-47] In recent years, the Advanced Composition Explorer (ACE) has made substantial contributions to our understanding of GCR composition and solar modulation.[48] Data of the GCR and SPE near Mars were also collected by the Martian Radiation Environment Experiment [MARIE] on the Mars Odyssey spacecraft.[49]

2.1.1 Model of galactic cosmic rays charge and energy spectra

Badhwar and O'Neill[50] have developed a self-consistent solution to the Fokker-Plank equation for particle transport in the heliopause that has been fit to available GCR data. This model accurately accounts for solar modulation of each element (hydrogen through nickel) by propagating the local interplanetary spectrum (LIS) of each element through the heliosphere by solving the Fokker-Planck diffusion, convection, and energy loss boundary value problem. A single value of

the deceleration parameter, $\Phi(t)$, describes the level of solar cycle modulation and determines the GCR energy spectrum for all of the elements at a given distance from the sun. More recently O'Neill[51] reanalyzed the model using data from ACE.

The energy spectrum of each element at the outer heliosphere boundary is accurately described by a power law in total energy per nucleon. O'Neill[51] has shown that the ACE data demonstrate that inclusion of β, particle speed relative to the speed of light, in the simple power allows for very accurate agreement with GCR data for all elements down to energies of approximately 50 MeV/u.

$$j_{lis}(E) = j_0\, \beta^{\delta} \;/\; (E + E_0)^{\gamma} \tag{2.2}$$

where $j_{lis}(E)$ is the differential LIS for an element, E is the kinetic energy/nucleon of the particle, and E_0 is the rest energy/nucleon of the particle (~938 MeV/u). The free parameters are γ, δ, and j_0, which are determined from fits to the ACE data and differ for each element. By using this representation, the root mean square (RMS) error for the interstellar GCR composition of less than ±10% is found for all major GCR components. Because the LIS is constant over very long time scales, the largest uncertainty in models of GCR environments is describing solar modulation effects.

2.1.2 Isotopic composition of galactic cosmic rays

The GCR model of Badhwar and O'Neill[50,51] describes the elemental composition and energy spectra of the GCR, including its modulation by the magnetic field of the sun. only the most abundant GCR nucleus is considered for each element in this representation, and other isotopes of identical charge are counted as the abundant isotope. However, theoretical models and satellite measurements of the GCR also consider the isotopic composition of the GCR and its modification through transport in interstellar space where nuclear fragmentation occurs, including estimating the primary nuclear composition at stellar sources.[40,41,52] The isotopic description of the primary GCR may modify the neutron fluence at high energy because, in many cases, neutron-rich isotopes make important contributions in the near-Earth GCR.

The approach used by Cucinotta et al[39] is to estimate from satellite measurements an energy-independent isotopic fraction, f_j, that is constrained to obey the sum-rule as follows:

$$\phi(Z,E) \;=\; \sum_{A_j} f_j \phi(A_j, Z, E) \tag{2.3}$$

where the left side of Eq(2.3) is the elemental spectra from the Badhwar and O'Neill model and $\sum_j f_j = 1$. Experimental data on mass distributions of the GCR have included measurements on the Pioneer, Voyager, and Ulysses spacecraft. Since secondary fragment production is modulated by the transit time in the heliosphere, the isotopic fraction is dependent on the position in the solar cycle. However, we compared radiation shielding calculations in which the isotopic components were modulated over the solar cycle to calculations fixed by the Ulysses estimates near solar minimum and found the differences to be small. The Ulysses estimates are then used for the isotopic composition for radiation transport calculations, such as with the HZETRN code.[39]

Table 2.1 shows the LIS parameters and average model RMS in percentage for elements.[51]

Table 2.1. LIS parameters and average model RMS error in % for elements.[51]

Z	Element	γ	δ	J_0	#ION[1]	#DAYS[2]	% Φ_{ACE}[3]	% Φ_{CLI}[4]
1	Hydrogen	2.765	0.0	1.2500E-3	1000	7	9.3	12.0
2	Helium	3.053	0.0	4.0000E-5	1000	21	9.9	11.3
3	Lithium	2.704	0.887	2.8000E-7	N/A	365	5.6	5.9
4	Beryllium	2.776	1.196	1.4000E-7	N/A	365	8.9	7.5
5	Boron	3.040	0.369	1.8000E-7	1000	48	7.6	9.5
6	Carbon	2.835	0.0	1.3000E-6	2000	21	4.9	7.8
7	Nitrogen	2.973	0.250	2.2500E-7	1000	35	6.8	8.7
8	Oxygen	2.800	0.0	1.4000E-6	2000	18	4.5	7.3
9	Fluorine	2.882	0.816	2.2000E-8	200	74	11.6	13.6
10	Neon	2.823	0.0	1.8700E-7	1000	43	5.9	8.2
11	Sodium	2.803	0.0	3.8094E-8	500	79	6.2	7.5
12	Magnesium	2.826	0.0	2.4841E-7	1000	28	5.5	7.4
13	Aluminum	2.903	0.472	3.3718E-8	300	49	8.3	9.7
14	Silicon	2.823	0.0	1.8340E-7	1000	32	5.3	7.1
15	Phosphorus	2.991	1.399	5.3011E-9	100	95	12.5	14.2
16	Sulfur	2.838	0.690	3.7502E-8	300	54	8.7	9.5
17	Chlorine	3.041	1.929	5.0000E-9	100	101	16.8	16.7
18	Argon	2.918	1.291	1.3000E-8	100	43	13.0	11.6
19	Potassium	3.169	1.827	5.8000E-9	100	52	15.0	16.7
20	Calcium	2.910	0.996	2.8000E-8	200	36	9.5	10.3
21	Scandium	2.926	1.267	5.8351E-9	100	73	13.0	12.3
22	Titanium	2.790	0.532	2.4982E-8	200	45	10.8	11.4
23	Vanadium	3.028	0.617	5.6000E-9	100	48	13.1	13.5
24	Chromium	2.945	0.582	1.4400E-8	200	43	10.2	11.1
25	Manganese	2.794	0.0	1.2000E-8	200	66	11.7	12.5
26	Iron	2.770	0.0	1.4000E-7	1000	32	6.1	6.7
27	Cobalt	2.764	0.0	9.4052E-10	30	94	22.5	21.5
28	Nickel	2.712	0.0	8.3950E-9	100	64	13.7	14.2

[1]Minimum number of ions per channel collected to define the interval data point.
[2]Average collection time.
[3]Average model – ACE % error from solar minimum (1997.6) to solar maximum (2000.9) using the value of $\Phi_{ACE}(t)$ determined from the ACE cosmic ray isotope spectrometer (CRIS) oxygen fit.
[4]Average model – ACE error with the value of $\Phi_{CLI}(t)$ determined from the CLIMAX neutron monitor used instead of that from fit to Oxygen.

For the *Z*=1 and Z=2 ions, the following empirical formula can be used to estimate the primary (near-Earth) ^{2}H and ^{3}He spectra:[39]

$$\phi_{3He}(E) = \left\{0.0764 + 0.097\exp[-0.5(\ln(E/1660)/1.306)^2]\right\}\phi_{4He}(E) \quad (2.4a)$$

$$\phi_{^2H}(E) = 0.2\phi_{^4He}(E) \quad (2.4b)$$

where $\phi_{3He}(E)$ and $\phi_{2H}(E)$ are subtracted from the Badhwar and O'Neill model spectra for $\phi_{4He}(E)$ and $\phi_{1H}(E)$, respectively. Primary ^{3}H and neutron spectra are not considered because of their short half-lives. Examples of the GCR energy spectra for hydrogen and helium are shown in **Figure-2.2a** and for the isotopes of Ne, Si, and Fe at solar minimum in **Figure-2.2b**.

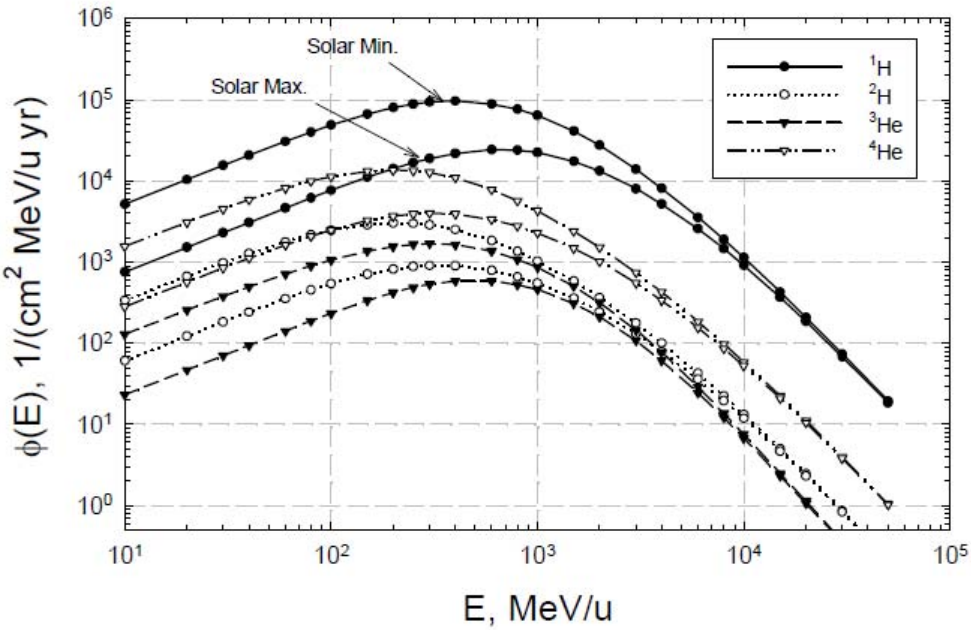

Figure 2.2.a. Energy spectra near solar minimum (Φ=428 MV) and solar maximum (Φ=1050 MV) for primary GCR light ions.

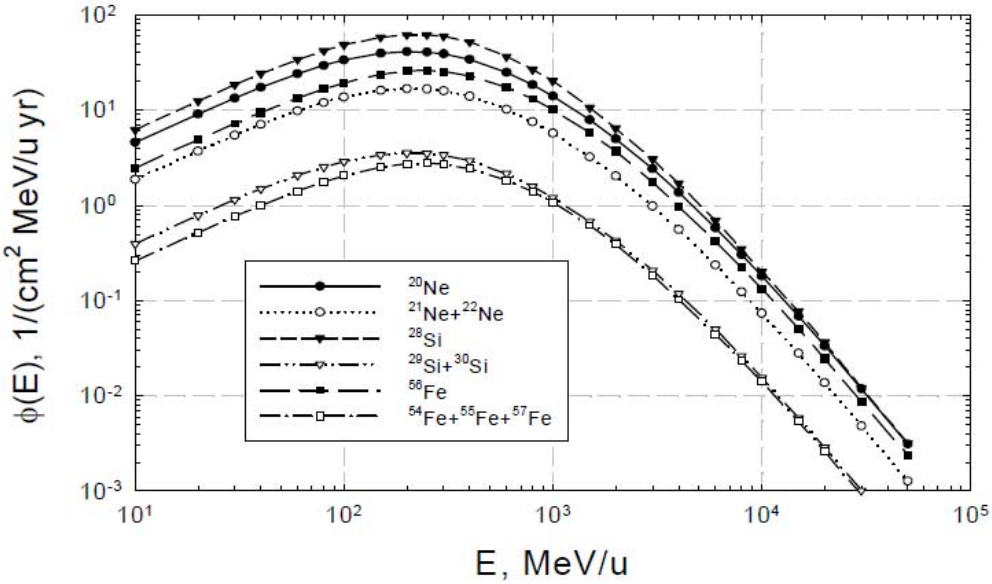

Figure 2.2b. Energy spectra near solar minimum (Φ=428 MV) for primary GCR isotopes of Ne, Si, and Fe.

2.1.3 Solar modulation of the galactic cosmic rays

The intensity of the GCR flux varies over the approximately 11-y solar cycle due to changes in the interplanetary plasma that originates in the expanding solar corona.[50,53] The intensity and energy of GCR entering the heliosphere is lowered as the rays are scattered by irregularities in

the interplanetary magnetic field embedded in the solar wind. Parker[52] showed that the steady-state, spherically symmetric Fokker-Planck equation accurately accounts for diffusion, convection, and adiabatic deceleration of these particles. The Fokker-Planck equation is readily solved numerically to propagate the LIS for each element to a given radius from the sun. A single diffusion coefficient, Eq(2.5), was used by Badhwar and O'Neill as well as by others to describe the effect of the magnetic field of the sun on particles entering the heliosphere.

$$k(r,t)=(k_0/V_{SW})\beta P[1+(r/r_0)^2]/\Phi(t)) \tag{2.5}$$

where V_{SW} is the constant solar wind speed (400 km/s), r is distance from the sun in AU, t is time in years, k_0 is constant, β is particle speed relative to the speed of light, P is particle rigidity in MV, and $\Phi(t)$ is solar modulation parameter in MV.

In the Badhwar and O'Neill model the effect of magnetic field, including disturbances and the radial gradient, is described by the diffusion coefficient. An inverse square law (for 1/k(r, t)) for a spherical cavity is assumed. To fit each of the various elements from hydrogen to nickel with the simple analytical LIS form, the modulation cavity scaling parameter r_0 was set to be 4.0 AU by O'Neill.[51] The physical significance of the 4 AU cavity scaling is not yet clear; the actual boundary of the cavity was set at 50 AU. The single-fit parameter that determines the level of solar modulation is $k_0/\Phi(t)$. O'Neill[51] and others set k_0 to a constant ($k_0 = 1.6\times10^{21}$ cm^2/s) and then determined the value of $\Phi(t)$ that fits the measured spectra. The $\Phi(t)$ is related to the energy and rigidity required for interstellar particles to propagate through the heliosphere to the radius of interest.

The modulation parameter at solar minimum or maximum varies to some extent for each solar cycle.[54] A worst-case solar minimum, based on the 1977 minima, has been widely used for shielding design studies. The most recent solar minima (2009) was reported as slightly deeper with a modulation parameter of Φ~410 MV compared to 428 MV for 1977. For solar maximum a wide range of modulation parameters values is observed for each cycle; and, more importantly, the occurrence of large SPEs is not well predicted relative to the position in the solar cycle as described below. Therefore, a modulation parameter of about 1100 MV provides a reasonable GCR background to investigate SPE risks.

Defining a worst-case GCR environment for mission design studies entails several considerations. We note that most NASA design studies have used a GCR environment representing the 1977 solar minimum to correspond to the worst case. Each solar cycle will have a distinct solar modulation and will depend on the polarity of the solar field, which itself switches from positive to negative polarity on a 22-y cycle. Negative polarity cycles are more likely to show deeper solar minima (smaller modulation parameters). As mission length increases, using a single-modulation parameter would overestimate the conditions at solar minimum. **Figure 2.3** shows the GCR modulation averaged over increasing mission length, which describes the impact of using a fixed-modulation parameter.[55] On the one hand, solar modulation over recent cycles does not reflect historical periods. Castagnoli et al[56] made estimates based on a sunspot number that suggests much deeper minima in past centuries, as shown in **Figure 2.4**. (Note that there is a shift in the modulation parameter of about 70 MV due to the method of estimate in the Catagnoli approach compared to that of Badhwar and O'Neill). On the other hand, we note that no error bars are given for such estimates, and, more importantly, the modulation is for lower energy particles that have smaller penetration depth in shielding and tissue. The effect of increased modulation beyond that of the 1977 solar minimum decreases with increasing

shielding depth, perhaps representing a 10% increase in GCR organ dose equivalents when comparing 428 MV to, say, 350 MV based on our earlier analysis.[57]

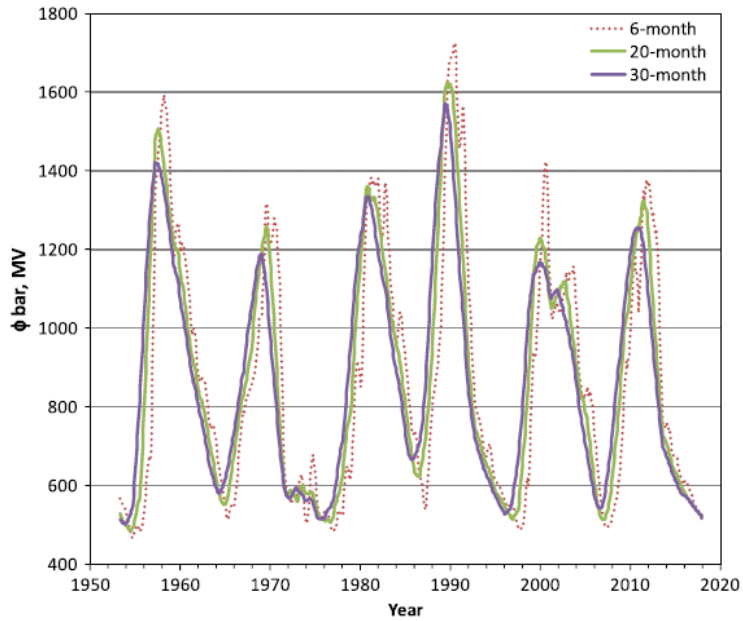

Figure 2.3. The average GCR deceleration (modulation) parameter for increasing mission length, as if a mission started at any time in a solar cycle and lasted for the indicated period.

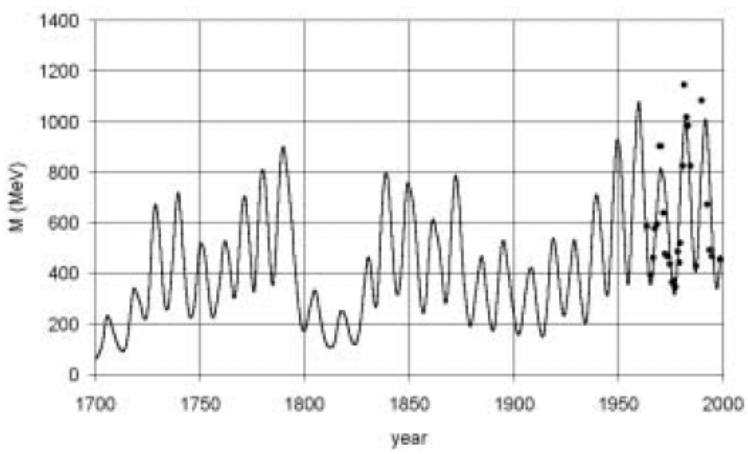

Figure 2.4. A reconstruction of the GCR solar modulation parameter described by Castagnoli et al[56] (2003). Filled circles are experimental values calculated from the GCR spectra measured with balloons and spacecraft.

2.2 Solar Particle Events

Radiation protection from SPEs can be divided into the pre-mission design phase and real-time responses during the mission (not discussed herein). The SPE frequency and total particle fluence, energy spectra, and duration must be described for mission design assessments. A solar flare is an intense local brightening on the face of the sun close to a sunspot. The solar abnormality results in an alteration of the general outflow of solar plasma at moderate energies and

local solar magnetic fields carried by that plasma. An important source for SPEs is energetic ions accelerated to higher energies by interplanetary shocks generated by coronal mass ejections (CMEs).[5] As solar plasma envelops the Earth, the magnetic screening effects inherent in plasmas act to shield the Earth from the GCR (this is known as a Forbush decrease.[58] In fact, for most solar events, ISS crew doses are lowered by the Forbush effect, which leads to a decrease in GCR doses that offsets any increase in organ dose equivalents from solar protons.

For solar cycles 19-21 (1955-1986), the list of major SPEs and the proton fluences have been assembled by Shea and Smart,[59] who placed all available flux and fluence data in a useful continuous database. An SPE list and the geostationary operational environmental satellite (GOES) measurements of the 5-minute average integral proton flux (from 1986 to the present [solar cycles 22 and 23]) can be obtained through direct access to the National Oceanographic and Atmospheric Agency (NOAA) National Geophysical Data Center (NGDC). **Table 2.2** lists the large SPEs in the past five solar cycles for which the omnidirectional proton fluence with energy above 30 MeV, Φ_{30}, exceeded 10^9 protons/cm^2. Only 13 events with at least this size occurred in nearly 60 y of observation. As described below, this probability is similar to the probability for all events dating back to the 15th century.[60] Between the years 1561 and 1950, 71 SPEs with $\Phi_{30} > 2\times10^9$ protons cm^{-2} (Ref. 61) were also identified from impulsive nitrate enhancements in polar ice cores. About 40 other SPEs with lower cutoff of 10^8 protons/cm^2 occurred in the same time period. As a rule of thumb, events of size below a 30-MeV fluence of 10^8 protons per cm^2 would present organ doses less than about 0.01 Gy for nominal shielding (even smaller doses in LEO) and, therefore, have only small health consequences to astronauts. We show the relationship between the SPE event date and size with the GCR solar modulation parameter in **Figure 2.5**. It has been demonstrated that an increase in SPE occurrence is associated with increasing solar activity; however, no recognizable pattern has been identified. Large events have definitely occurred during solar active years, but these events have not occurred exactly during months of solar maximal activity. Moreover, they are more likely to take place in the ascending or declining phases of the solar cycle.[62] This sporadic behavior of SPE occurrence is a major operational problem in planning for missions to the moon and Mars.

Table 2.2. Summary of $\Phi_{30} > 10^9$ protons/cm^2 values for the largest SPEs during solar cycles 19 through 23.

Solar Cycle	SPE	Φ_{30}, protons/cm^2
19	11/12/1960	9.00 x 10^9
20	8/2/1972	5.00 x 10^9
22	10/19/1989	4.23 x 10^9
23	7/14/2000	3.74 x 10^9
23	10/26/2003	3.25 x 10^9
23	11/4/2001	2.92 x 10^9
19	7/10/1959	2.30 x 10^9
23	11/8/2000	2.27 x 10^9
22	3/23/1991	1.74 x 10^9
22	8/12/1989	1.51 x 10^9
22	9/29/1989	1.35 x 10^9
23	1/16/2005	1.04 x 10^9
19	2/23/1956	1.00 x 10^9

2.2.1 Hazard function for solar particle event occurrence

More than 90% of the SPEs that occurred in solar cycles 19-23 would pose a small health risk, these can nevertheless result in significant mission disruption. This suggests that a probabilistic risk assessment (PRA) model is needed for mission design. Kim et al[60] have used survival analysis to develop a model of SPE size and frequency for a standard solar cycle that provides such a PRA tool. The model considers all SPEs for solar cycles 19-23 (1955-1986) and the ice-core nitrate estimates of large events since the 15th century, and assembles the available flux and fluence data in the form of a continuous database (**Figure 2.5**). A total of 370 SPEs were identified during solar cycles 19–23. Events were found to be statistically differ significantly in overall distribution of Φ_{30} from cycle to cycle. However, fluence data of Φ_{30} were combined over all five cycles to estimate an overall probability distribution of an average cycle. **Figure 2.6** shows sample cumulative tail probabilities of Φ_{30} for cycles 19-23 and the overall cumulative tail probability (thick line). Also included in **Figure 2.6** are the probabilities of the impulsive nitrate events of 71 SPEs with $\Phi_{30} > 2\times10^9$ protons cm^{-2} (Ref. 61) with and without seasonal correction, and they do not differ significantly from the modern sets of large Φ_{30} data.[60] **Table 2.3** lists all of the available database of SPEs for the omnidirectional proton fluence of Φ_E, where E = 10, 30, 50, 60, or 100 MeV. While the expected frequency of SPEs is strongly influenced by solar modulation, the SPE occurrences themselves are chaotic in nature. **Figure 2.7** shows the onset times of all SPEs in solar cycles 19-23.

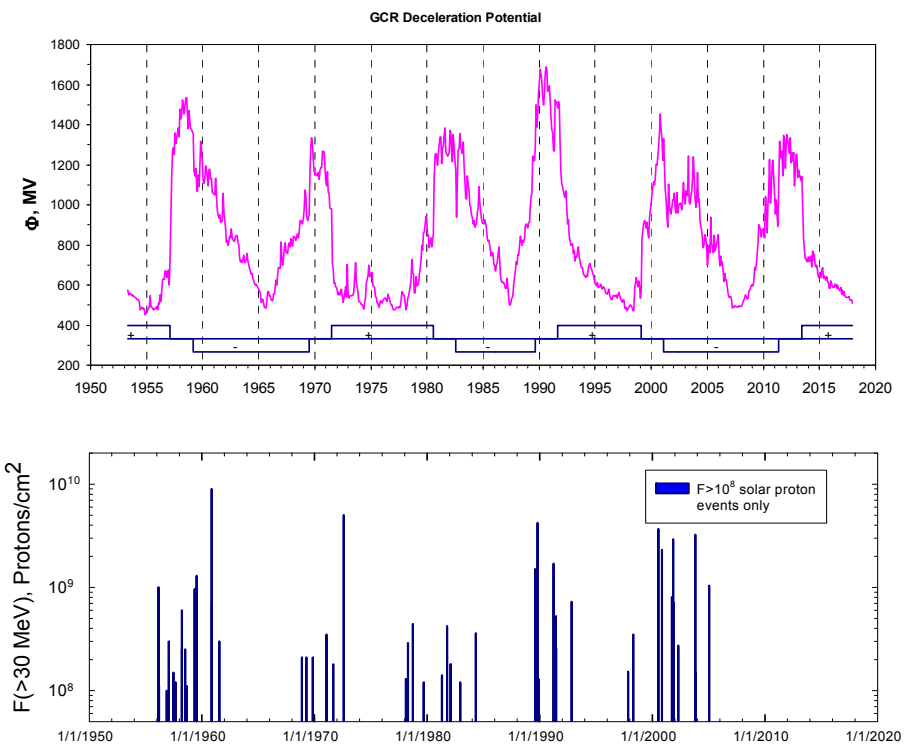

Figure 2.5. Historical data on fluence of protons above 30 MeV per cm^2 (F(>30 MeV) from large SPEs relative to solar modulation parameter (Φ). Only events with $\Phi_{>30\ \mathrm{MeV}} > 10^8$ particles per cm^2 are shown in the lower graph**.**

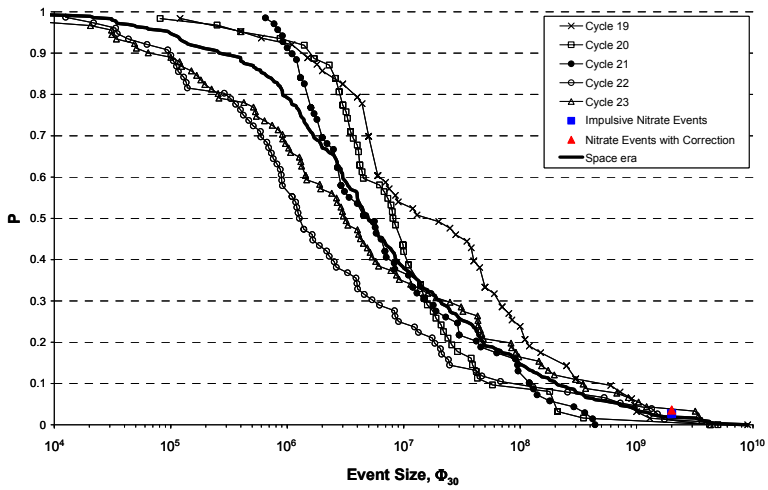

Figure 2.6. Probability (P) of an SPE event exceeding the displayed threshold Φ_{30}.

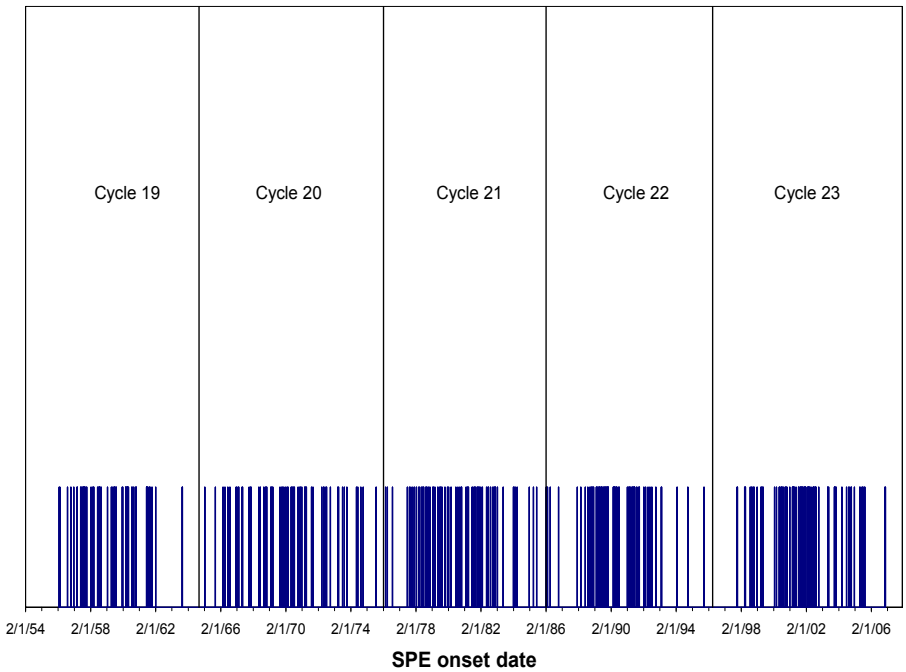

Figure 2.7. The onset dates of SPEs occurring between January 1, 1956 and December 31, 2007.

Observations over solar cycles 19-23 were represented by a hazard function for the probability of SPE occurrence for a given mission length as a function of time within a cycle. Because there are typically more SPEs near the middle of cycles than there are near the beginning and end of cycles, the hazard function should take on relatively low values at the ends of each solar cycle and reach a peak somewhere near the middle of each solar cycle. After studying different models for the hazard function and assessing goodness of fit, the functional form best explaining all SPEs was found as:[60]

$$\lambda(t) = \frac{\lambda_0}{4000} + \frac{K}{4000}\frac{\Gamma(p+q)}{\Gamma(p)\Gamma(q)}\left(\frac{t}{4000}\right)^{p-1}\left(1-\frac{t}{4000}\right)^{q-1} \tag{2.6}$$

for a "typical" nonspecific cycle of 4000 days duration ($0 < t < 4000$), where λ_0, K, p, and q are parameters to be estimated. Resulting maximum-likelihood parameter estimates were λ_0 = 19.52, K = 55.89, p = 4.073 and q = 4.820. From Eq(2.6), it can also be shown that μ, the time of peak hazard, is $4000(p-1)/(p+q-2)$ days into a cycle. For the observed data, μ was estimated at 1783 days.

Table 2.3. Published databases of recorded SPEs.

Solar Cycle	# of SPE	# of Day	Period	Φ_E
Cycle 23	92	4262	5/1/1996-12/31/2007*	$\Phi_{10,30,50,60,100}$ (NGDC 2010)
Cycle 22	77	3742	2/1/1986-4/30/1996	$\Phi_{10,30,50,60,100}$ (a)
Cycle 21	70	3653	2/1/1976-1/31/1986	$\Phi_{10,30}$ (b)
Cycle 20	63	4140	10/1/1964-1/31/1976	$\Phi_{10,30}$ (b) and $\Phi_{10,30,60}$ (c)
Cycle 19	68	3895	2/1/1954-9/30/1964	$\Phi_{10,30,100}$ (b) and $\Phi_{10,30}$ (d)
Impulsive Nitrate Events	71	390 y	1561 – 1950	Φ_{30} (e)

*The end of cycle 23 estimated.[59,61,63-65]

The expected number of events for a mission in a time interval (t_1, t_2), $N(t_1, t_2)$ were estimated more accurately by using the basic properties of a Poisson process and the estimated $\lambda(t)$ at time t of a solar cycle than could be obtained by simple counting of cases in the SPE data occurring in a given time period (t_1, t_2). For conservatism, missions can be assumed to take place centered on the time of greatest hazard, μ = 1783 days into a solar cycle, so that $t_1 = 1783 - d/2$ and $t_2 = 1783 + d/2$, where d is mission length (days).

2.2.2 Representation of solar particle event energy distribution

Wilson et al[66] studied typical spacecraft shielding to show that protons with energies up to about 200 MeV or more are needed to fully characterize SPE organ doses. Unfortunately, only fluence at 100 MeV or below is reported for many historical events, which leads to inaccuracies in transport code predictions of SPE risks. Common functional forms to represent spectra are exponential or power law functions in rigidity, the Weibull function, and more recently a double power-law for studying high-energy SPEs where ground level enhancements (GLEs) were observed with neutron monitors (the so-called Band function[67,68]). **Figure 2.8** compares two of the extreme examples of differences that occur in extrapolating energies beyond measurements with different functional forms. The best fit for the functional forms is shown in the upper panel, and predictions of Effective doses vs. shielding depth are shown in the lower panels. Models are smaller for many other SPEs differences between energy spectra; however, the comparison of **Figure 2.8** shows the importance of accurate determination of proton energy spectra from major SPEs.

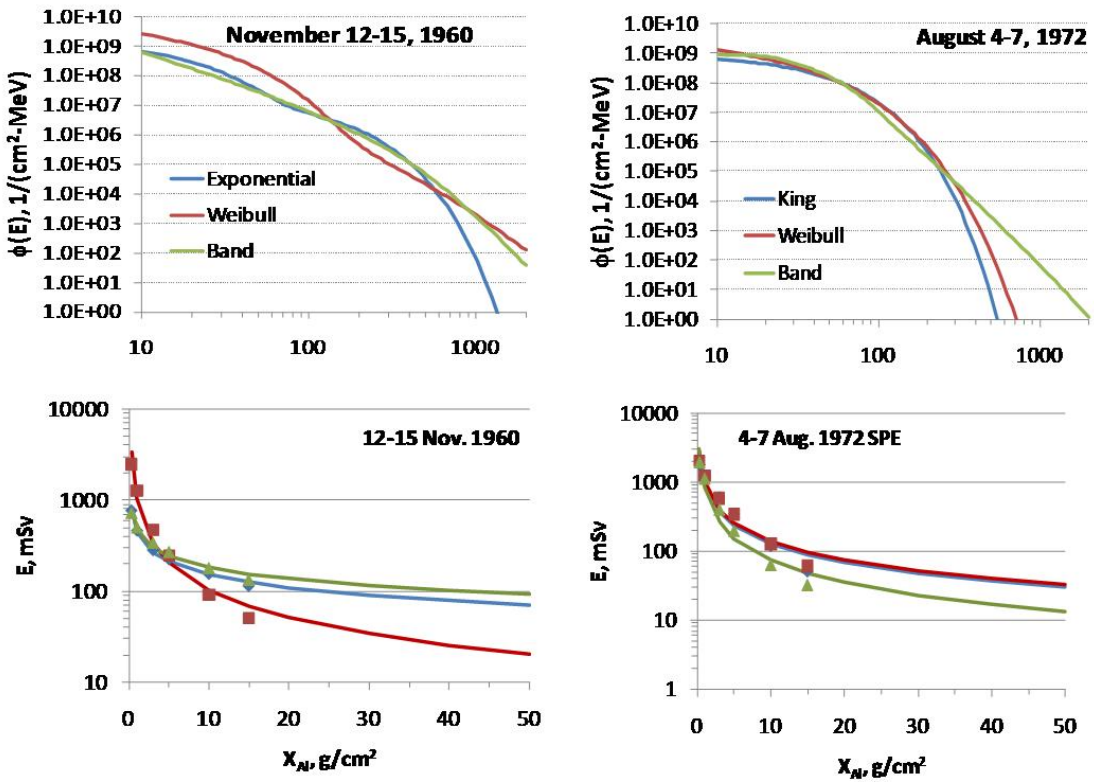

Figure 2.8. Comparison of exponential, Weibull, or Band functions fit to proton fluence measurements for the November 1960 and August 1972 events (upper panels) and the resulting predictions of Effective doses (lower panels).

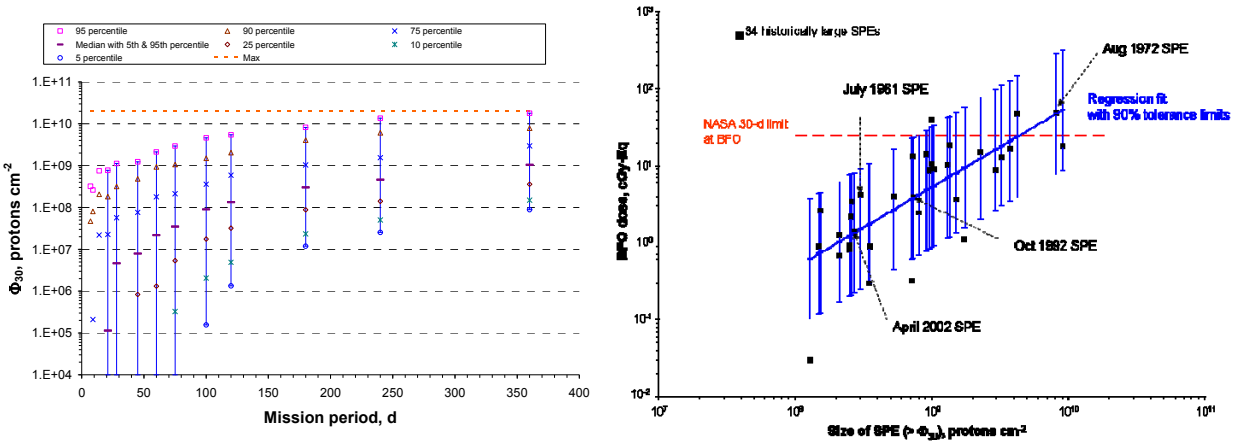

Figure 2.9. (Left panel) Simulated distribution of integral proton fluence above 30 MeV, Φ_{30} as a function of increasing mission length. (Right panel) The blood-forming organ (BFO) dose behind 5 g/cm^2 aluminum shields from the 34 largest SPEs in the Space Age ranked by 30-MeV proton integral fluence, $F_{>30\ MeV}$ calculated by the BRYTRN code.[60] The black circles show the doses from each of the 34 events. The error bands show the 90% CLs due to the variability of the proton energy spectra of the 34 events. The red dashed line shows the NASA 30-day dose limit for the BFO.

A recognizable pattern of event size distribution during the past 5 solar cycles has not been identified, and the event size Φ_{30} is independent of elapsed time between two consecutive events.[60] Therefore, the individual event size Φ_{30} for each SPE occurrence must be independent of the expected number of events for a given mission duration, $N(d)$. For the randomness of individual event size, Φ_{30} was simulated with a random draw from a gamma distribution. An empirical distribution of total fluence Φ_{30} ranging from 5th to 95th percentile is shown in **Figure 2.9** for a range of potential mission lengths. With the expected number of events, which took into account the randomness of SPE occurrences, total event sizes of Φ_{30} in a mission period have been simulated ranging from its 5th to 95th percentile. Intense SPEs were considered as potentially debilitating events. Also shown in **Fig. 2.9** are the resulting BFO doses taking into account the actual proton spectra for the 34 largest events in cycles 19 through 23. Very few SPEs would exceed the NASA 30-day limit for acute risks with minimal shielding, leaving the residual cancer risks the major concern. In assessing radiation risk from SPEs during a given mission period, the simulation illustrates that risk assessors must take into account not only the randomness of SPE occurrences and each event size of Φ_{30}, but also the variation of energy spectra for the SPEs, because the detailed SPE energy spectrum is the important parameter.

2.3 Physics Model Description of Organ Exposures

Descriptions of the fluence for each particle type and energy at each tissue of interest must be characterized before risk projections can be made. Fortunately, radiation transport codes validated by extensive measurements have been combined with accurate descriptions of the space environment to make accurate predictions of exposures to sensitive tissue sites behind spacecraft shielding or on planetary surfaces. Radiation transport codes were studied extensively in the past, and currently there are only minor scientific questions that lead to errors in the assessment of space radiation environments. Boltzmann equation solvers or Monte-Carlo algorithms can be used for this purpose when they are combined with models of the space environment as well as spacecraft and organ shielding. Monte-Carlo codes require long computational times to describe spacecraft with thousands of parts. Complex geometries are typically handled with simplifications in the representation by combining parts and material composition, thus negating any advantages compared to the one-dimensional transport methods that could be found by treatment of detailed three-dimensional effects. Boltzmann equation solvers such as the HZETRN code[69] are able to use ray-tracing techniques to consider a very detailed geometry in a one-dimensional approach that is adequate for fast ions, especially for the omnidirectional radiation sources in space. The relative contribution from low-energy charged ions that deviate from the straight-ahead approximation can be solved by quadratures, leaving only the angular deflections of neutrons and intermediate energy light ions with sufficient energy to produce nuclear reactions to be addressed when considering a deviation from one-dimensional transport. However, their relative contribution to a GCR space transport problem may be small, reducing the significance of any errors due to a one-dimensional approach.

The underlying physical processes described by transport codes are atomic energy loss, straggling, and nuclear collisions. For describing atomic processes, the LET (stopping power), range, and energy straggling parameters are known to ±5% accuracy.[33] A wide range of nuclear interactions occurs in GCR transport leading to a diverse range of secondary particles as described in **Table 2.4**.[5,70] The nuclear cross sections needed for space radiation transport include nuclear absorption, heavy ion fragmentation, light ion scattering, and particle production cross sections. Nuclear absorption cross sections are well described by current models with accuracies of ±5% for most collision pairs of interest.[71] Fragmentation cross sections for heavy fragments are known

to about a ±25% accuracy[39,72] with most of the error localized to a nearby to a fragment with a similar A, Z, and kinetic energy, thus reducing the impact of errors in estimating biological effects.

Table 2.4. Reaction products in nuclear collisions important in study of space radiation studies.

Type[1]	*Secondary*	*Mechanism*	*Comment*
N-A, A-A	Nucleon	Knockout, cascade	Low LET, Large R
N-A, A-A	Nucleon	Evaporation	Medium or high LET, small R
N-A, A-A	Light ion	KO, Evaporation, Coalescence	Low to medium LET, small to large R
N-A	Heavy ion	Elastic or TF	Small R, High LET
A-A	Heavy ion	PF	Large R
A-A	Heavy ion	TF	Small R, High LET
N-A, A-A	Meson, γ-ray, e^-, etc.	Inelastic NN	Large R, low LET

[1]N is the nucleon (proton or neutron), A is nucleus, PF is projectile fragment, TF is target fragment, and R is range.

For lighter secondaries (A<5), details on the energy spectra and angular distributions are also needed, which have been extensively studied since the 1950s and well described by the various Monte-Carlo transport models. However, cross-section data are sparse for some projection-target combinations, especially above 1,000 MeV/u, and improvements in how differential cross sections are represented in transport codes is required.

While three-dimensional aspects of transport from angular scattering are a small correction for high-energy ions, they should be considered for neutrons and other light0mass ions. Estimates of neutron contributions to organ dose equivalents in space from as little as 5% to as much as 50% have appeared in the literature. Neutrons are secondary radiation produced largely by cosmic ray protons and helium particles because of their larger abundances compared to heavy ions, and tertiary or higher-order effects between neutrons and charged particles are frequent behind shielding. Differences in interpretation of neutron contributions often arise due to differential measurement techniques or scoring approaches in transport codes. However, the consistent agreement between physical dosimetry and biological dosimetry from space shuttle and ISS crew[30] as well as the HZETRN code reported in the past[73] suggests that the contributions of neutrons are reasonably well understood. This topic is discussed in more detail below. Mesons, e-, and γ-rays are also secondary radiation that are not always considered in transport models. However, because they are low-LET radiation with small QFs, and exploration spacecraft with current launch capabilities will be mass constrained with average shielding of approximately 10 g/cm^2, their impact on overall risks should be small.

Three approaches to assessing uncertainties in transport models describing exposures to sensitive tissue sites behind spacecraft shielding from space radiation exist:

1) Comparison of ground-based measurements for defined beams on thin and thick targets for different material compositions and amounts
2) Intercomparison of radiation transport codes using matched configurations and environments
3) Comparison of transport codes to space flight measurements[74]

We summarize recent results in each of these areas next.

2.3.1 Comparisons of ground-based measurements to transport codes

Extensive thin target measurements and theoretical calculations were made in the past to describe proton-, neutron-, and heavy-ion-induced nuclear collisions. NCRP Report No. 153[5] reviews this information, including experimental data for cross sections and theoretical reaction models. Several important data sets on heavy-ion interactions and neutron cross sections have occurred since this report further improves databases for transport code calculations. We therefore do not review thin target data accuracies in this report. Instead, we will discuss recent thick target measurements, which further document the accuracy of radiation transport code models. The NSRL has made extensive measurements for a variety of HZE nuclei of the Bragg ionization curve in polyethylene or aluminum shielding. A recently developed Monte-Carlo-based transport code, the GCR Event-based Risk Model (GERMCode), uses the quantum multiple scattering fragmentation model (QMSFRG) of nuclear interaction database, and the range-energy subroutines denoted as RMAT from HZETRN to describe the NSRL beam line for radiobiology applications.[70] **Figure 2.10** compares the NSRL measurements with the GERMCode for ^{28}Si, ^{37}Cl, ^{48}Ti, and ^{56}Fe nuclei. Excellent agreement between the model and the measurements is seen at all depths, including past the Bragg peak or primary ion range to which only secondary radiation contributes. In **Figure 2.11** we show comparisons of the GERMCode measurements by Zeitlin et al[75] to elemental distributions of secondary fragments at two depths in polyethylene shielding for 1-GeV/u Fe beams. Agreement between theory and measurements is typically within ±20%. Energy loss in silicon detectors has been measured behind graphite-epoxy. Data were compared to calculations of the GRNTRN code,[76] which has many important overlaps with the HZETRN code. The results in **Figure 2.12** show good agreement between code and measurement.[77]

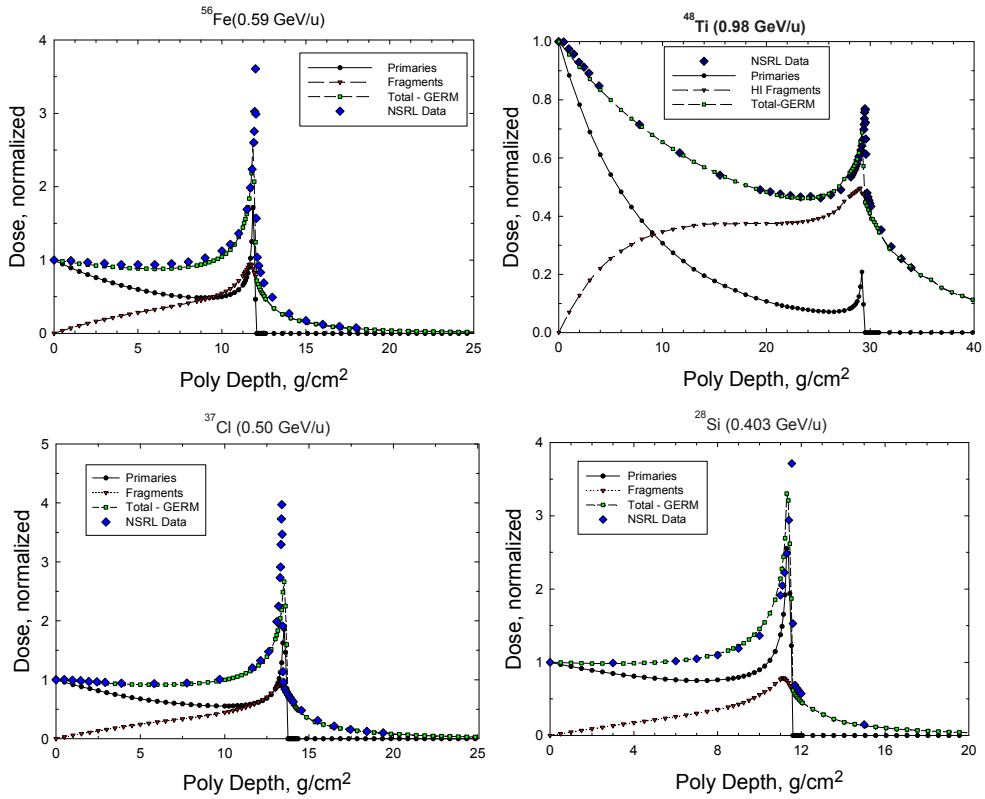

Figure 2.10. Comparisons of the GERMCode[70] to NSRL measurements (www.bnl.gov) for depth-dose in polyethylene for nearly monoenergetic ^{56}Fe(0.59 GeV/u), ^{48}Ti (0.98 GeV/u), ^{37}Cl(0.5 GeV/u), and ^{28}Si(0.403 GeV/u) nuclei.

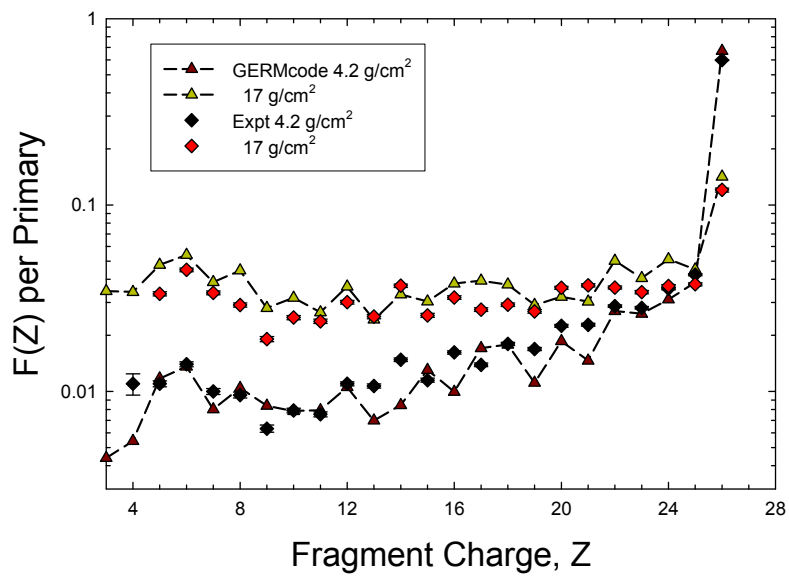

Figure 2.11. Comparison of the GERMcode with QMSFRG nuclear cross-section model to thick target data from Zeitlin et al[75] for fragmentation of 1-GeV/u ^{56}Fe beam at two depths of polyethylene.

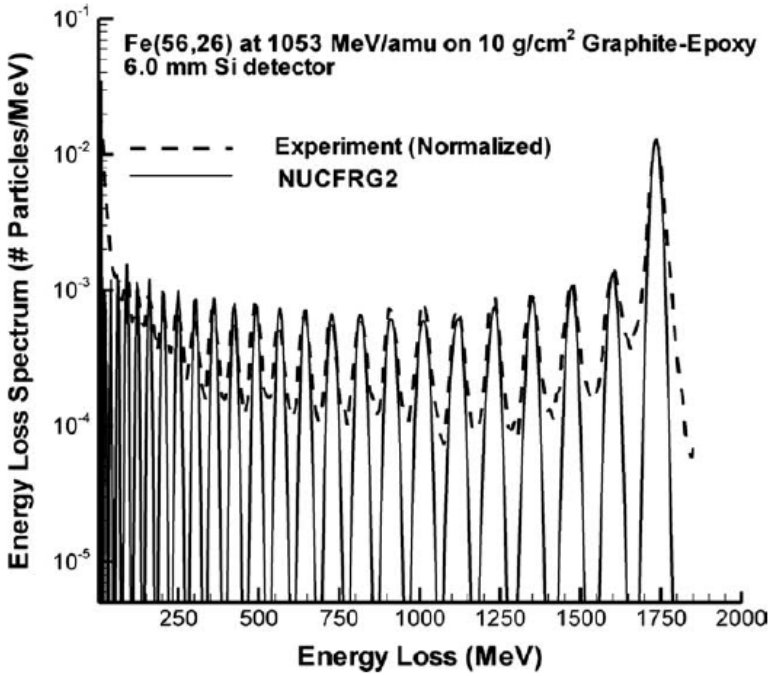

Figure 2.12. Comparisons of GRNTRN code to measurements for the summed energy loss in a silicon detector from fragments of a 1053-MeV/u ^{56}Fe beam behind 10 g/cm^2 graphite-epoxy (51%/49%) (reproduced from Walker et al).[77]

2.3.2 Intercomparisons of transport codes

Recently Wilson (private communications, 2009) has organized intercomparisons of the HZETRN code to several Monte-Carlo codes for well-defined shielding configurations and identical source energy spectra for GCR and SPEs. The Monte-Carlo codes considered were HETC-HEDS,[78] FLUKA,[79] and PHITS.[80] These results, as summarized in both **Figure 2.13** and **Figure 2.14**, are in very good agreement for depth-dose, depth-dose-equivalent, and light-particle energy spectra. Some of the comparisons on organ doses did not consider all of the contributions from target fragments that introduce minor differences. These comparisons show that overall agreement between transport code predictions, when compared with identical source spectra and shielding configuration, is quite high. A possible minor discrepancy is the mesons, electrons, and γ-rays that may contribute 5% to 10% of the absorbed dose from GCR behind ISS levels of shielding, and 1% to 3% of the dose equivalent because of their small QFs or RBEs compared to HZE nuclei, or to stopping protons and helium nuclei. These processes have not been fully integrated into all versions of the various existing codes, and should be considered for deep-shielding predictions (>50 g/cm^2).

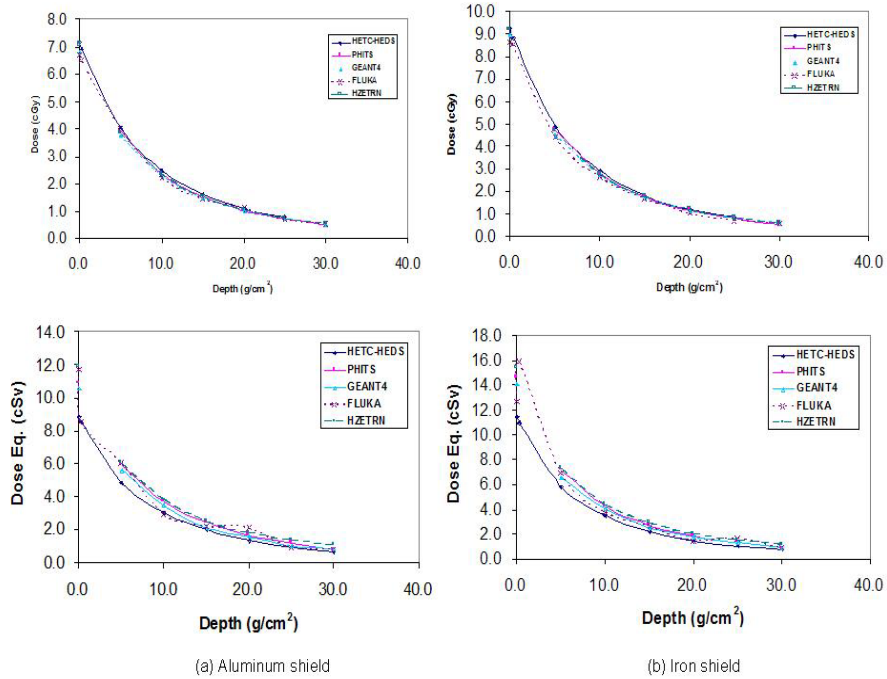

Figure 2.13. Intercomparison of several transport codes for SPE depth dose and depth dose equivalent for aluminum and iron shielding (J Wilson, private communication).

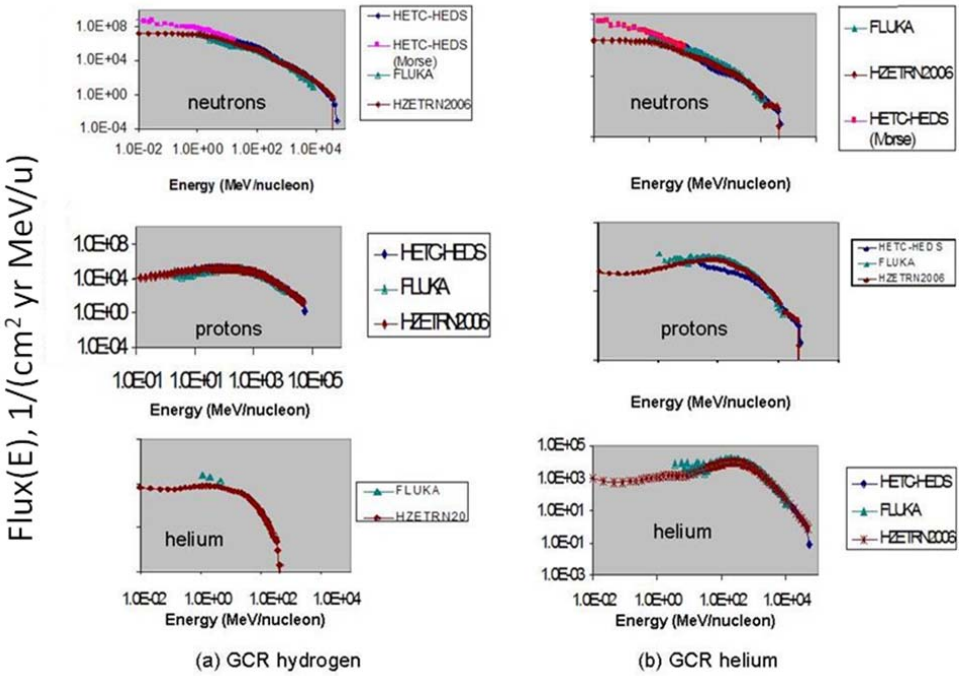

Figure 2.14. Intercomparison of secondary light particle spectra calculated with several space radiation transport codes for 20-g/cm^2 aluminum shielding (J. Wilson, private communication).

2.3.3 Space flight measurement comparisons to transport codes

Organ doses and dose equivalents can be estimated from space radiation transport models assuming they were made up of the following components: the GCR, solar particles, or trapped protons including their secondary components (protons, neutrons, etc.). Shielding amounts are described by the areal density, x, in units of g/cm^2, which represents the physical thickness, t in units of cm, times the material density, ρ, in units of g/cm^3, or $x=\rho t$. The GCR contribution varies slowly with the amount of shielding, but the SPE or trapped proton dose decreases rapidly with increasing depth-making small contributions relative to GCR to the Effective dose at large shielding depth (>20 g/cm^2). We used the HZETRN code with nuclear interaction cross sections generated by the QMSFRG model to make various predictions to space flight data. The QMSFRG model provides an accurate database with an agreement of over 85% of the measured heavy ion fragmentation cross sections <±25% error,[39,72] and a smaller error for the total absorption cross sections <±5% error. A two-dimensional matrix, corresponding to the vehicle and tissue shielding thicknesses, can be computed for the flux of ion j of energy, E (units of MeV/u) for the thickness x (units of g/cm^2) in spacecraft shielding, and thickness z (units of g/cm^2) of tissue denoted as $\phi_j(E,x,z)$ (units of ions per cm^2 per MeV/u per mission time). The absorbed dose and dose equivalent are evaluated by:

$$D(x,z) = \sum_j \int dE \phi_j(E,x,z) S_j(E) \tag{2.7}$$

$$H(x,z) = \sum_j \int dE \phi_j(E,x_j,z) S_j(E) Q(S_j(E)) \tag{2.8}$$

where $S_j(E)$ is the ion LET, which depends on kinetic energy and mass and charge of nuclei. A unit conversion coefficient is ignored in Eq(2.7) and Eq(2.8), and throughout this report in similar equations. Organ doses for a tissue, T, are evaluated using computerized male and female geometry models and averaged over shielding at a spacecraft location, n, as

$$H_T(n) = \sum_j \sum_x a_x \sum_z b_z \int dE \phi_j(E,x,z) S_j(E) Q(S_j(E)) \tag{2.9}$$

where a_x and b_z are shielding fractions of equal solid angle intervals from a shielding model for the spacecraft or organ. The so-called "point" dose, $D_{pt,}$ is defined by Eq(2.7) for z=0. In radiation protection practices, the Effective dose[25,26] is defined as an average of organ dose equivalents using tissue weighting factors, w_T, as

$$E_T = \Sigma w_T \; H_T \tag{2.10}$$

The tissue weights, which are gender-averaged, include contributions for the gonads for hereditary risk. Contributions from largely nonlethal cancers such as nonmelanoma skin and thyroid cancers are included in the ICRP definition. **Because of the large attenuation of SPE doses at deep-seated organs compared to skin, thyroid, and gonad organ dose equivalents, SPE Effective doses can be dominated by such doses such that the use of Effective dose may lead to a substantial overestimation of cancer mortality risk. The usage of gender and age averaging for tissue weights leads to further inaccuracies, and can be avoided as described later in this report.**

Table 2.5 compares the physical dosimetry to transport code assessments of point dose and dose equivalent inside the shuttle orbiter for a multitude of missions. Very good agreement is

found. Phantom torsos comprised of realistic distributions of human tissue-equivalent materials have been flown on several space shuttle missions, as reported earlier by Badhwar et al[81] for organ-absorbed doses and Yasuda et al[82] for organ dose equivalents estimated using a combined thermoluminescent dosimeter (TLD) and CR-39 plastic track detector methodology. **Table 2.6a** shows absolute predictions of the HZETRN/QMSFRG model (without any scaling to dosimetry) to the measurements of Yasuda et al[82] on space shuttle mission STS-91, which flew in a 51.6-deg inclination orbit to the Russian *Mir* space station on a similar orbit as was flown by ISS. The comparisons show excellent agreement between measurements and models. The NASA phantom torso experiment that was flown on STS-91 was reflown on ISS Increment 2 in 2001. This experiment included several small, active silicon detectors located at critical organs to provide time-dependent dose data. The correlation of the time-dependent data to the ISS trajectory allows for separation of individual contributions from trapped protons and GCR to organ doses. **Table 2.6b** shows absolute comparison of the HZETRN/QMSFRG results (without scaling) to the measurements, indicating very good agreement.[73] The results show that the ratio of the GCR to trapped proton absorbed dose is about 1.5:1. Average QFs without tissue shielding for GCR (~3.5) are more than twice as high that of the trapped protons (~1.5);[34,73] these results therefore support the conclusion that organ dose equivalents for ISS missions and many space shuttle missions are predominantly from GCR (>80%). The resulting transport code predictions have been used to estimate Effective doses for all space missions (through 2008)[73] as shown in **Figure 2.15.** More recent phantom data have been collected by Reitz et al.[83]

Table 2.5. Comparison of HZETRN code to space flight measurements of absorbed dose or dose equivalent behind various shielding amounts and several space missions.

Mission	DATE	Inclination	Altitude	Shielding	Dose, mGy/d			Dose Eq., mSv/d		
					Measured	Theory	%Difference	Measured	Theory	%Difference
STS-40	1991	39	293	Dloc2	0.052	0.048	7.7	0.13	0.16	-23.1
STS-49	1992	28.5	358	Dloc2	0.05	0.048	4.0	0.127	0.155	-22.0
STS-51	1993	28.5	296	Payload Bay	0.044	0.048	-9.1	0.144	0.154	-6.9
STS-57	1993	57	298	Payload Bay	0.113	0.109	3.5	0.422	0.434	-2.8
STS-57	1993	57	298	DLOC-2	0.138	0.11	20.3	0.414	0.37	10.6
Mir-18	1995	51.6	390	P	0.142	0.141	0.7	0.461	0.526	-14.1
STS-81	1997	51.6	400	0-sphere	0.147	0.135	8.2	0.479	0.521	-8.8
STS-81	1997	51.6	400	Poly 3-in	0.138	0.138	0.0	0.441	0.400	9.3
STS-81	1997	51.6	400	Poly 5-in	0.129	0.118	8.5	0.316	0.368	-16.5
STS-81	1997	51.6	400	Poly 8-in	0.128	0.113	11.7	0.371	0.323	12.9
STS-81	1997	51.6	400	Poly 12-in	0.116	0.111	4.3	0.290	0.298	-2.8
STS-89	1998	51.6	393	0-sphere	0.176	0.148	15.8	0.561	0.614	-9.4
STS-89	1998	51.6	393	Al 3-in	0.167	0.159	4.8	0.445	0.488	-9.7
STS-89	1998	51.6	393	Al 7-in	0.149	0.161	-8.1	0.529	0.617	-16.6
STS-89	1998	51.6	393	Al 9-in	0.171	0.162	5.3	0.492	0.541	-10.0

Table 2.6.a. Comparison of measured organ dose equivalent for STS-91 mission by Yasuda et al.[82] using combined CR-39/TLD method to predictions from the HZETRN/QMSFRG space transport model.

	Organ Dose Equivalent, mSv		
Tissue	**Measured**	**HZETRN/QMSFRG**	**Difference (%)**
Skin	4.5 ±0.05	4.7	4.4
Thyroid	4.0 ±0.21	4.0	0
Bone surface	5.2 ±0.22	4.0	-23.1
Esophagus	3.4 ±0.49	3.7	8.8
Lung	4.4 ±0.76	3.8	-13.6
Stomach	4.3 ±0.94	3.6	-16.3
Liver	4.0 ±0.51	3.7	-7.5
Bone marrow	3.4 ±0.40	3.9	14.7
Colon	3.6 ±0.42	3.9	8.3
Bladder	3.6 ±0.24	3.5	-2.8
Gonad	4.7 ±0.71	3.9	-17.0
Chest	4.5 ±0.11	4.5	0
Remainder	4.0 ±0.57	4.0	0
Effective dose	4.1 ±0.22	3.9	-4.9

Table 2.6.b. Comparison of small active dosimetry data from ISS Increment 2 phantom torso (for July-August 2001) to predictions from the HZETRN/QMSFRG model.[73]

Organ	*Trapped, mGy/d*		*GCR, mGy/d*		*Total Dose, mGy/d*		*Difference*
	Expt.	Model	Expt.	Model	Expt.	Model	*(%)*
Brain	0.051	0.066	0.076	0.077	0.127	0.143	13.3
Thyroid	0.062	0.072	0.074	0.077	0.136	0.148	9.4
Heart	0.054	0.061	0.075	0.076	0.129	0.137	6.7
Stomach	0.050	0.057	0.076	0.077	0.126	0.133	5.5
Colon	0.055	0.056	0.073	0.076	0.128	0.131	2.5

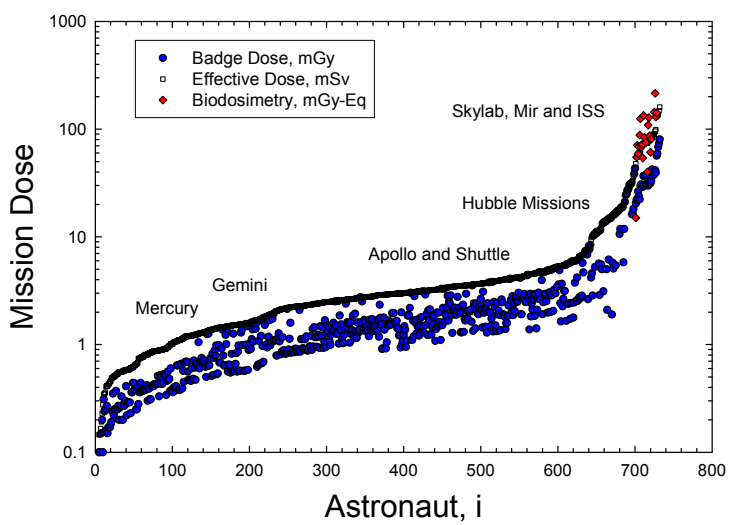

Figure 2.15. Summary of mission badge dose, Effective dose, and population average biological dose equivalent for astronauts on all NASA space missions, including Mercury, Gemini, Apollo, Skylab, Apollo-Soyuz, space shuttle, NASA-*Mir* and ISS missions.[73]

Energy spectra for light particles measured with particle hodoscopes are in good agreement with the HZETRN code as shown in **Figure 2.16**.[84] Measurements of heavy-ion spectra require a large area detector, and very few such measurements have been made in human-rated vehicles because of mass requirements. Other space flight measurements of LET or microdosimetry measurements of lineal energy spectra using tissue-equivalent proportional counters (TEPCs) have also been shown to be in good agreement with transport codes.[85,86] Agreement is obviously improved when models of detector response are used to make such comparisons. Corrections of measurements often involve model-dependent assumptions, such as the conversion from silicon to tissue-equivalent LET spectra in which the conversion factor is dependent on energy and charge number. Also, the combined TLD plus CR-39 method for estimating dose equivalent[82] involves corrections on the high-LET sensitivity of TLDs and the low-LET sensitivity of CR-39. Comparisons of codes to TEPCs data requires the conversion of energy and charge spectra into lineal energy spectra, which differ substantially from LET spectra. Comparisons of models to measurements of neutron spectra on the Russian *Mir* space station were in good agreement **(Fig. 2.17)**. The major fraction of the neutron dose is for energies >10 MeV, with a smaller fraction <10 MeV. At these higher energies, secondary recoil nuclei produced by neutrons are very similar in Z and E to those produced by high-energy protons. Therefore, at equal fluence, high-energy protons are more biologically effective than neutrons of the same energy because of the charge carried by protons.

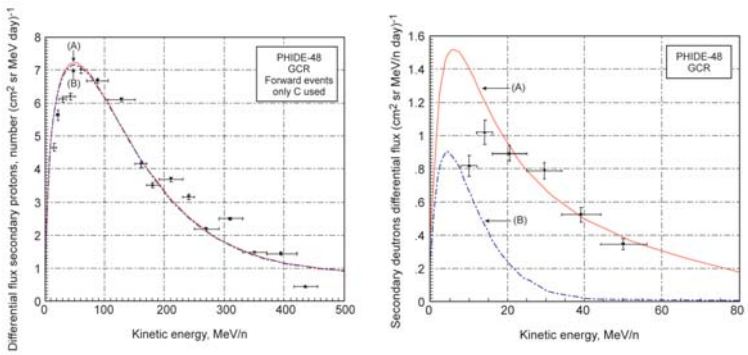

Figure 2.16. Comparisons of proton (Panel A) and Deuteron (Panel B) energy distributions from GCR on the STS-48 mission to HZETRN results.[84] The dash line and solid line are without or with cluster knockouts, respectively.

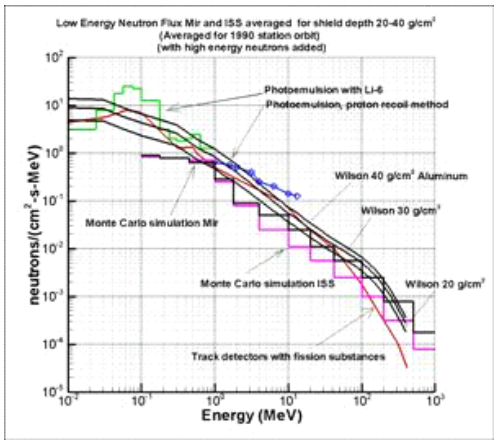

Figure 2.17. Comparisons of transport codes to ISS neutron spectra measurements.[87]

2.3.4 Predictions for exploration missions

We show the organ doses for GCR at solar minimum and the 1972 SPE for depths of 5 and 20 g/cm^2 diameter in aluminum spheres In **Table 2.7**. The 1972 solar event is represented by the protons fluence spectrum derived by King.[65] SPE spectra are greatly attenuated with shielding and show important variations in doses between tissue types, while GCR produces only a modest variation between organs at both depths. The point doses shown correspond to the dose without tissue shielding. Values of point doses are well above organ doses for SPEs and similar to organ doses for GCR. Doses to the skin can be several times higher than those of the internal organs for SPEs.[88] Average skin doses do not properly describe the risk to specific skin loci, which are highly variable. Annual GCR Effective doses are calculated in **Figure 2.18** for various charge groups inside a spacecraft of 50g/cm^2 aluminum from GCR at solar minimum in interplanetary space (blue bars). These heavy nuclei are a concern for radiation risks because they have the highest biological effectiveness and leave columns of damage at the molecular level as they traverse a biological system, and because a plausible mitigation measure by shielding is impossible due to the high penetration power of energetic particles of GCR.

Table 2.7. Organ doses for males inside aluminum shields for 1972 SPE and GCR at solar minimum.

(a) 5-g/cm^2 aluminum

Organ/tissue		August 1972 SPE			Annual GCR at solar minimum		
		D mGy	G mGy-Eq	H mSv	D mGy	G mGy-Eq	H mSv
Avg. Skin		2692.3	4052.1	4259.7	198.8	375.8	832.3
Avg. BFO		306.9	462.5	442.1	185.7	337.2	614.0
Stomach		112.3	169.6	168.0	182.2	324.4	547.6
Colon		251.4	379.0	363.8	185.6	336.4	606.2
Liver		174.1	262.7	255.0	183.1	327.9	566.6
Lung		205.6	310.1	299.4	184.5	332.9	590.9
Esophagus		195.4	294.8	285.0	184.0	331.3	584.4
Bladder		118.7	179.2	176.8	181.6	322.5	540.8
Thyroid		333.2	502.1	479.0	186.8	341.1	632.7
Chest/Breast		1615.9	2430.6	2323.9	194.1	365.6	770.2
Gonads/Ovarian		748.1	1125.7	1072.2	186.5	339.7	640.9
Front brain		571.7	860.9	816.4	190.6	354.4	696.9
Mid brain		279.6	421.5	403.9	187.7	344.1	640.2
Rear brain		557.5	839.6	796.2	190.5	354.0	695.2
Lens		1959.0	2946.2	2829.4	196.2	372.4	806.3
Gallbladder		118.7	179.2	176.8	181.6	322.5	540.8
Remainder		406.3	611.9	585.9	186.1	338.2	619.5
Point Dose		5389.0	8125.0	8663.0	218.2	434.4	1140.7
E, mSv	w_T (ICRP 1991)			612.3			611.1
	w_T (ICRP 2007)			676.2			620.7

(b) 20-g/cm^2 aluminum

Organ/tissue		August 1972 SPE			Annual GCR at solar minimum		
		D mGy	G mGy-Eq	H mSv	D mGy	G mGy-Eq	H mSv
Avg. Skin		87.8	132.8	144.0	193.5	342.3	599.8
Avg. BFO		23.4	35.7	42.9	182.0	314.9	494.2
Stomach		12.1	18.6	25.5	179.1	306.4	465.5
Colon		21.0	32.1	39.4	181.9	314.6	491.3
Liver		15.6	23.8	30.7	179.8	308.6	473.6
Lung		18.3	28.0	35.2	180.9	312.0	484.4
Esophagus		17.5	26.8	34.0	180.5	310.9	481.4
Bladder		12.0	18.4	25.0	178.6	305.0	462.2
Thyroid		25.7	39.1	46.5	182.9	317.5	502.5
Chest/Breast		67.2	101.9	107.0	189.0	333.8	558.7
Gonads/Ovarian		37.5	57.0	62.5	182.5	316.1	503.3
Front brain		37.6	57.1	64.8	186.1	326.6	530.5
Mid brain		24.0	36.7	44.8	183.7	319.8	506.9
Rear brain		37.0	56.4	64.0	186.0	326.4	529.8
Lens		76.7	116.1	120.9	190.8	338.4	574.0
Heart*		18.3	28.0	35.2	180.9	312.0	484.4
Gallbladder		12.0	18.4	25.0	178.6	305.0	462.2
Remainder		26.0	39.6	46.5	182.3	315.6	496.3
Point Dose		164.7	248.9	267.8	210.7	384.3	751.4
E, mSv	w_T (ICRP 1991)			45.83			492.48
	w_T (ICRP 2007)			48.45			496.74

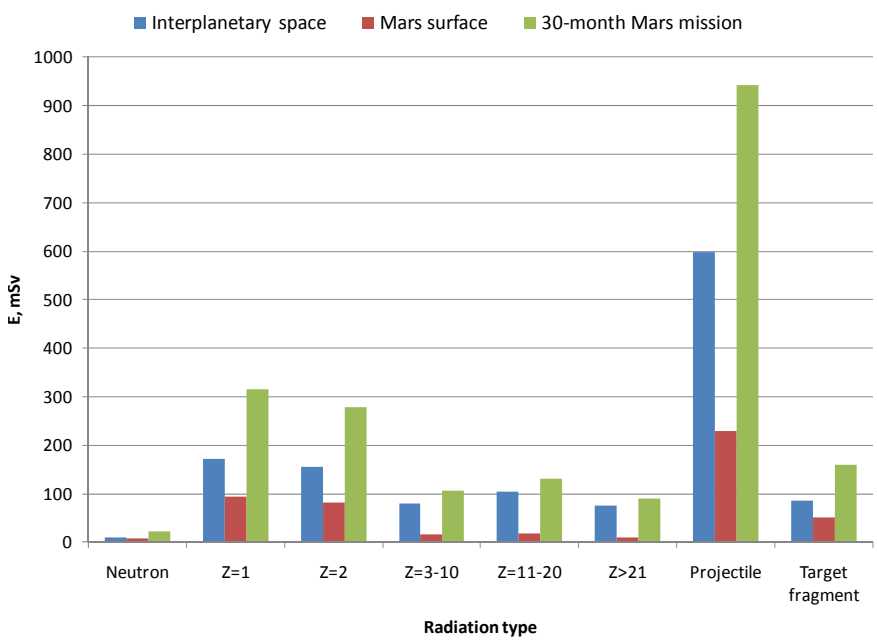

Figure 2.18. Effective doses for GCR charge groups, overall projectile-like dose (primaries and projectile fragments), and target fragments inside a spherical spacecraft of 5-g/cm^2 aluminum shield thickness: Annual exposure in interplanetary space, Mars surface, and for a 30-month Mars mission as solar minimum.

The interplanetary GCR fluxes at solar minimum on the martian surface were propagated through the martian atmosphere of 16 g/cm^2 carbon dioxide. Annual Effective doses are shown in the same figure on the martian surface (red bars) from GCR at solar minimum, in which radiation protection by martian atmospheric shielding and the shadow effect of Mars itself were estimated.[89] Also shown in **Figure 2.17** is the estimate of Effective dose for males during the 30-month Mars mission (green bars), which is composed of interplanetary transit to/from Mars for 6 months each way and a Mars surface stay for 1.5 y. Organ doses for males and females show small differences due to the variations in body shielding of the various organs. Total Effective dose is estimated at about 1.1 Sv for a male crew member inside a 5-g/cm^2 aluminum sphere at solar minimum.

The steep dose gradients of SPEs make the ICRP-defined tissue weights, w_T, used in the calculation of Effective doses inaccurate for NASA applications. SPEs lead to skin, thyroid, breast, and gonad doses that are much larger than the doses for the tissues that comprise the majority of cancer risks such as lung, colon, and stomach. Thus an overestimation of cancer mortality risks by several fold occurs when Effective doses are combined with total cancer risk coefficients to estimate risk. This is illustrated by calculations for the August 1972 SPE **Table 2.7** in which, at 5-g/cm^2 aluminum shielding, the Effective dose is more than 3-fold higher than the lung dose equivalent. Further examples were shown by Kim et al[90] using the NASA Space Radiation Program ProE ray tracer,[91] which is a computer-aided design (CAD) engineering design model, and the BRYNTRN transport code to calculate organ dose equivalents and Effective doses inside a four-person crew capsule similar to the Orion capsule (**Fig. 2.19**). Results shown in **Table 2.8** are at locations of the four crew persons inside the capsule (dosimetry locations [DLOCs] 1 to 4), where a more than 2-fold difference between Effective dose and deep-seated organ dose equivalents occurs. The August 1972 event is about the 70th percentile in spectral hardness of SPEs observed in the Space Age. This implies that the ICRP approach is even less accurate for fatal cancer risk estimates for most other SPEs compared to results for the 1972 event because the dose gradient is larger for the many “softer” SPE spectra.

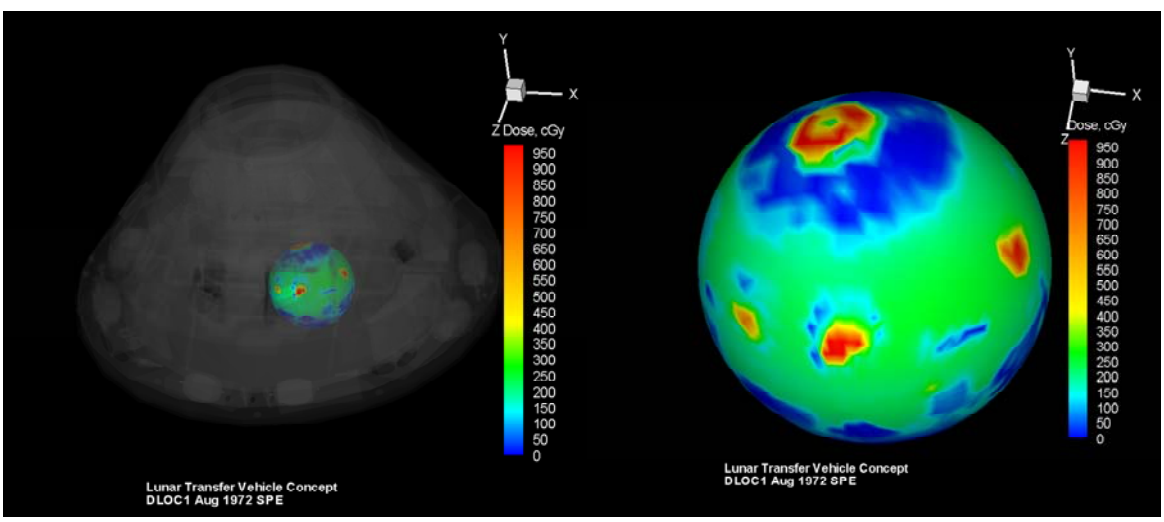

Figure 2.19. Visualization of detailed directional dose assessment at a dosimetry location (DLOC1) inside a conceptual spacecraft representative of a lunar transfer vehicle (LTV). The spacecraft is shown in a translucent view to reveal the exact dosimetry location (left), and the same directional dose assessment is shown separately in the large view (right).

Table 2.8. August 1972 SPE organ dose quantities for males using the fully automated ProE structural distribution model LTV, the computerized anatomical man model (CAMERA), and the BRYNTRN codes. The King spectra for the SPE is used. Calculations are at the location of each crew member in the LTV.

		Organ Dose Equivalent, mSv			
		DLOC1	DLOC2	DLOC3	DLOC4
Al-Eq x_{avg}, g/cm^2		15.18	15.08	15.85	15.33
CAM organ dose	Avg. skin	1266	1211	1041	1086
	Eye	868	844	736	771
	Avg. BFO	169	168	152	159
	Stomach	73.8	73.7	67.7	70.3
	Colon	144	144	130	136
	Liver	104	103	94.1	98.0
	Lung	122	121	110	115
	Esophagus	116	116	105	110
	Bladder	75.4	75.3	69.0	717
	Thyroid	184	183	166	173
	Chest	722	706	619	648
	Gonads	353	347	308	322
	Front brain	295	293	263	275
	Mid brain	162	162	147	153
	Rear brain	289	287	258	270
Effective Dose, mSv		213	210	188	196
Point Dose Eq., mSv		2557	2427	2079	2168

2.4 Probability Distribution Function for Space Physics Uncertainties

The above comparisons show good agreement between ground-based and space flight measurements with predictive transport code models. We did not review shielding models such as ray tracers and combinatorial geometry models for spacecraft or geometry models, including voxel-based models for organ shielding. However, the comparisons described suggest overall agreement for a combined environment (x_{env}), transport(x_{tran}), and shielding (x_{shield}) model to be within ±15% for Effective dose comparisons. The HZETRN model does not appear to be systematically higher or lower to the various measurements in such comparisons. It could be argued that past flight measurements have not been sufficiently robust, or other assignments of radiation QFs may increase particle components not emphasized in the current ICRP 60 model[26] used in Effective dose calculations. We therefore will assign a slightly higher overall physics model uncertainty than our estimate of ±15%. Below we will consider particle track-structure models to describe radiation quality effects. Particle track-structure and energy deposition in biomolecules, cells, and tissues is naturally described by the parameter Z^{*2}/β^2, where Z^* is the effective charge number of the ion and β is the velocity scaled to the speed of light. We will describe new recommendations for radiation QFs that replace the LET dependence from ICRP Report 60[26] with one that depends on Z^{*2}/β^2 for light- and heavy-charge particle groups.

The PDF for describing the uncertainty in radiation exposures at tissue sites is described in **Table 2.9.** Uncertainty analysis will be made using the HZETRN code with QMSFRG nuclear cross sections and the Badhwar and O'Neill GCR environment model.[39,51,69] We will consider uncertainties for the fluence distributions of two groups of ions: light ions with charge numbers of Z=1 to 4; and heavy ions with charge numbers of Z=5 to 28. The HZETRN code used in this

analysis does not consider photons and mesons, which are low-LET radiation, and therefore slightly underestimates fluence spectra at low values of Z^{*2}/β^2. HZETRN also tends to underestimate low-energy neutrons (E<1 MeV) compared to Monte-Carlo based codes, which predominantly produce biological damage through light ion recoils and photons. For the PDF for light ion contributions to the fluence spectra, $F(Z^{*2}/\beta^2)$, we assume a normal distribution with a mean shifted to higher values (M=1.05), and the standard deviation (SD) of 0.33 for light ions compared to heavy ions in which the SD is assigned as 0.25. These choices are consistent with the good agreement found between transport codes and laboratory and flight measurements. Individual components may have higher SDs; however in an earlier report,[14] we noted the importance of the constraints implied by transport codes comparisons flight measurements of dose and dose equivalent when defining PDFs for particle spectra uncertainties. For considering deep-shielding conditions (for eg, thicker shielding than the ISS) with average shielding of 20 g/cm^2 from which the uncertainty assessment was made, a larger physics uncertainty should be considered. However, we note that the ISS is likely to contain more mass than exploration spacecraft because of the higher costs to launch mass outside of LEO.

Table 2.9. Assessment of physics uncertainties for light and heavy particles using a Gaussian distribution with median (M) and SDs.

$F(Z^{*2}/\beta^2)$	Median (M)	Standard Deviation (SD)
Light ions (Z≤4)	1.05	1/3
Heavy ions (Z>4)	1.0	1/4

3. Cancer Risk Projections for Low-linear Energy Transfer Radiation

The current radiation cancer risk projection model used at NASA is based on NCRP Report No. 132;[6] however, this has been updated by NASA (PELs, 2006) to use the solid cancer mortality analysis made in LSS [Life-span Study of the Japanese atomic-bomb survivors] Report 13.[9] These methods form the basis by which to calculate the current dose limits used at NASA; ie, age- and gender-specific Effective dose to reach a probability of 3% for REID. In recent years there have been important new analyses of human epidemiology data by the BEIR VII Committee,[16] UNSCEAR,[17] Preston et al,[92] National Cancer Institute (NCI),[93] Little et al,[10,94] Pawel et al,[95] and others. Important changes since NCRP Report No. 132 include a reevaluation of the A-bomb survivor doses denoted as DS02.[96] Longer follow-up studies of the exposed cohorts with the most recent incidence data from the LSS from the Radiation Effects Research Foundation (RERF) cover the years 1958 through 1998.[92] Meta-analysis of different exposed cohorts for specific tissues such as breast and thyroid cancers has been reported. Application of new methodologies includes Bayesian analysis of dosimetry errors[10] and empirical Bayes methods for tissue-specific cancer risk uncertainties.[95] New analyses of the DDREF were made by the BEIR VII and Jacobs et al[97] from a meta-analysis of 12 published radiation worker studies. An important change advocated by the BEIR VII report is to estimate cancer mortality risks by the transfer of incidence rates in exposed cohorts to populations under study (eg, the U.S.), and then to estimate mortality risks using the ratio of host population cancer mortality and incidence rates. Previous recommendations from the NCRP used mortality-based risk transfer models.[6] In this section, we will review the mathematical approaches to calculate low-LET cancer risks and intercompare recent fits to the most recent LSS data.

The instantaneous incidence rate of cancer, $\lambda(t)$, is defined in terms of the probability distribution function, *F(t)*, of the time to cancer occurrence. The survival function, *S(t)*, is the probability of being cancer-free at age *t* (the interval [0,*t*]), and is given by *1-F(t)*. The probability density function, *f(t)*, is then *dF(t)/dt*. The hazard rate is the instantaneous incidence rate as is given by

$$\lambda(t) = \frac{f(t)}{1-F(t)} \tag{3.1}$$

The cumulative hazard, $\Lambda(t)$, also known as the cumulative incidence rate, is

$$\Lambda(t) = \int_0^t \lambda(z)dz \tag{3.2}$$

The survival probability is related to the cumulative hazard function by

$$S(t) = \exp[-\Lambda(t)] \tag{3.3}$$

To model radiation risk along with radiation hazard rates, the age- and gender-specific survival probability (often represented by a life-table) must be described because of the role of competing causes of death. For multiplicative risk models (described below), the age- and gender-specific hazard rates for cancer incidence or mortality in the population under study also must be defined.

The instantaneous cancer rate (mortality or incidence) can be a function of dose, D, or dose-rate, D_r, gender, age at exposure, a_E, attained age, a, or latency, which is the time after exposure, $L=a-a_E$. These dependencies may vary for each cancer type that could be increased by radiation exposure. Hazard rates for cancer incidence, λ_I, and cancer mortality, λ_M, can be modeled with similar approaches. The REID is calculated by folding the probability of surviving to time, t, which is represented as the survival function, $S_0(t)$, for the background population times into the probability for radiation cancer death at a previous time with the instantaneous radiation cancer mortality rate and then integrating over the remainder of a lifetime:

$$REID(a_E, D) \quad = \quad \int_{a_E} dt \lambda_M(a, a_E, D) S_0(t) e^{-\int_{a_E}^{t} dz \lambda_M(z, a_E, D)} \tag{3.4}$$

Similarly, the risk of exposure-induced cancer incidence (REIC) uses a radiation cancer incidence rate folded with the probability to survive to time, t, and integrated over the remainder of a lifetime:

$$REIC(a_E, D) \quad = \quad \int_{a_E} dt \lambda_I(a, a_E, D) S_0(t) e^{-\int_{a_E}^{t} dz \lambda_M(z, a_E, D)} \tag{3.5}$$

The BEIR VII report[16] uses the quantity lifetime attributable risk (LAR) instead of REID as the primary measure of risk. Others committees[98] have used the quantity ELR. (Note: NCRP Report No. 132 discusses results in terms of ELR; however, the formula on page 127 of the report suggests that REID was calculated in the report.) The LAR and ELR risk measures have important deficiencies and are not used at NASA. The ELR ignores cancer deaths that would have occurred anyway in a population but are moved to an earlier time point due to radiation exposure. ELR therefore underestimates risks. The LAR ignores the radiation contribution to the survival probability in Eq(3.4) or Eq(3.5). It thus leads to an overestimation of risk, especially at high doses, and also can lead to errors in uncertainty analysis when large risk values are sampled in Monte-Carlo trials.

3.1 Cancer Mortality and Incidence Rates

Radiation cancer incidence (or mortality) rates are most often modeled in the multiplicative risk model that is also denoted as the excess relative risk (ERR) model in which the radiation cancer rates are proportional to background cancer rates given by:

$$\lambda_I(a, a_E, D) \quad = \quad \lambda_{I0}(a)[1 + ERR(a, a_E, D)] \tag{3.6}$$

where $\lambda_{i0}(a)$ is the age-specific (and tissue- and gender-specific) cancer rate from background cancers in the population under study. A second model is also used; this study, denoted as the excess additive risk (EAR) model, does not explicitly depend on the background cancer rates given by:

$$\lambda_I(a, a_E, D) \quad = \quad EAR(a, a_E, D) \tag{3.7}$$

Radiation cancer rates can be fitted to data on all cancers or various sub-categories including tissue-specific cancer rates. Overall cancer incidence data have lower statistical uncertainties than overall mortality data because of higher counts. Projecting tissue-specific cancer incidence probabilities has higher statistical uncertainties due to lower counts compared to fitting grouped data such as all solid cancers and leukemias. However, projections based on tissue-specific incidence data offer many advantages including the possibility to apply tissue-specific transfer models between populations, tissue-specific radiation quality, and dose-rate dependencies. Attributable risks calculations for estimating probability of causation on disease discovery are evaluated with tissue-specific incidence models.[93] The astronaut informed-consent process is also improved if information on specific cancer types for both incidence and mortality risks is provided. More recently, an empirical Bayes method has been shown to provide an improved representation of statistical errors in tissue-specific risks.[95]

A multiplicative risk model for projecting cancer mortality (REID) from tissue-specific cancer incidence uses identical ERR functions determined for incidence to project tissue-specific mortality using population cancer incidence rate to mortality rate scaling.[16] Similarly, an additive risk model derived from incidence data can be used for mortality risk prediction by adjusting EAR functions derived from incidence data by the ratio of background mortality to incidence rates:[16]

$$\lambda_M(a, a_E, D) \quad = \quad EAR(a, a_E, D)\frac{\lambda_{M0}(a)}{\lambda_{I0}(a)} \tag{3.8}$$

Various advisory reports have used distinct approaches to arrive at assumptions on how to combine multiplicative and additive risk model estimates. A weighting of the multiplicative transfer model, denoted as ν_T, can be introduced. The additive transfer model weight is then given by $1-\nu_T$. NCRP Report No. 132 recommended to use an arithmetic mean of the additive and multiplicative risk models for all solid cancers and the additive risk model for leukemia risk. Although the recent UNSCEAR report[17] did not make a recommendation on risk transfer models, we note that its multiplicative risk model provides the best fit to the LSS. The BEIR VII report uses geometric means of the additive and multiplicative transfer models for most cancer types with a weight ν_T of 0.7 including leukemia, but deviates for lung, breast, and thyroid cancer risk estimates. For lung cancer, BEIR VII assigns a weight ν_T of 0.3, favoring additive transfer based on an older analysis of smoking interactions with radiation in the LSS .[96]

Projecting tissue-specific astronaut risks from space radiation requires functional forms for the ERR and EAR for cancer incidence for astronaut ages at first flight, typically age at exposure, a_E> 30 y. The recent report of Preston et al[92] uses Poisson regression models with appropriate adjustments to test several dose response models with a linear dose-response model providing the best fits of REIC for most solid cancers. Results are represented by ERR functions of the form

$$ERR(a, a_E, D) \quad = \quad \beta_s\, f(D)(\frac{a}{70})^p e^{-c(a_E-30)} \tag{3.9}$$

And of the same functional form, but with different parameters for EAR:

$$EAR(a, a_E, D) \quad = \quad \beta_s\, f(D)(\frac{a}{70})^p e^{-c(a_E-30)} \tag{3.10}$$

where $f(D)$ represents a dose-response function. Several dose-response functions were considered; however, a linear function was found to provide the best fit, ie, $f(D)=D$. These functions have no dependence on latency, L. Although the BEIR VII report used similar models as Eq(3.9) and Eq(3.10), fit LAR was used instead of REIC, and no age at exposure dependence of the rates for exposures was assumed over age 30 y (ie, c=0 in these equations for a_E>30 y with other parameters thus modified in fitting the data).

The UNSCEAR report used Poisson maximum-likelihood methods and Bayesian analysis to represent dosimetry errors to fit generalized ERR and EAR models for cancer incidence. The ERR functions were of a more general form than the BEIRVII or RERF models:

$$ERR(a, a_E, L, D) \quad = \quad (\alpha D + \beta D^2)e^{\gamma D} \exp[\kappa_1 1_S + \kappa_2 \ln(a - a_E) + \kappa_3 \ln(a) + \kappa_4 \ln(a_E)] \qquad (3.11)$$

with a similar form for the EAR function. Equation (3.11) includes a dependence on latency that was not tested in Eq(3.9) or Eq(3.10). In a manner similar to the results of Preston et al,[92] the linear dose response model provided optimal fits to the tissue-specific cancer incidence data. The addition of latency dependence was significant for several tissues including EAR models for colon, breast, and nonmelanoma skin cancer, and ERR and EAR functions for the category of all other solid cancer incidence. The UNSCEAR report, in its functional form given by Eq(3.11), considered an exponential term with argument, γD, in the exponent to represent cell sterilization effects. This approach would be useful in the pursuit of space radiation models, but would take a significant amount of study to determine the radiation quality dependence of the cell sterilization term across different tissues, and might be confounded by a correlation between RBE value estimates and cell sterilization effects.

The various approaches described above to fitting the most recent data set from the LSS are based on stratified dose groups with follow-up time from 1958 through 1998. The UNSCEAR and Preston et al[92] models used REIC or REID as the basic risk quantity while BEIR VII used LAR. Each report assumed a dose-independent neutron RBE of 10. Tissue-specific doses were approximated by colon dose estimates for solid cancers and bone marrow doses for leukemia. Not all of the minor tissues considered in each report were identical, which leads to differences in the definition of the remaining terms representing all cancer types excluded from tissue-specific analysis.

Tests of goodness of fit to the LSS cancer mortality and incidence data were made by the UNSCEAR committee[17] using both the BEIR VII and the UNSCEAR models, and suggested that the UNSCEAR more general model as described by Eq(3.11) provided the best fit to these data sets. (See the UNSCEAR report Appendix D for details.) Several dose response models were tested, and the result showed the linear dose response model provided the best fit for tissue-specific incidence and a linear-quadratic (LQ) model to total solid cancer mortality data.

3.2 Adjustment for Low Dose-rates

The models described above for projection of radiation cancer risks should be adjusted for dose-rate modifiers because epidemiology data are largely for acute doses of γ-rays, which are expected to be more effective than doses delivered at low doses or dose-rates (<0.2 Gy or 0.05 Gy/hr). This adjustment can be made by reducing the cancer incidence or mortality rates by a DDREF. DDREF values of about 2 have been used in the past. Uncertainties and recent data on DDREFs are described below. Here we note that recently smaller values of the DDREF have

been described by BEIR VII[16] and other reports compared to the recommendation of NCRP Report No. 132.[6] In contrast, the UNSCEAR-preferred model fit to total solid cancer mortality was an LQ dose response model.[10,17] An identical approach to leukemia risk estimation could therefore be followed where no DDREF is applied, while the quadratic dose term is ignored for low dose-rates. However, the optimal fit to cancer incidence by UNSCEAR was a linear dose response model, where a DDREF would normally still be applied.

3.3 Comparisons of Tissue-specific Risk Models

We compared the BEIR VII,[16] UNSCEAR,[17] and Preston et al[92] model fits for age- and gender-specific REIC and REID probabilities using the 2005 U.S. population data for cancer incidence, mortality, and life-table for all causes of death.[99] All calculations are made with a DDREF of 1.75 for solid cancer risks, and the linear component of the leukemia model. Preston et al[92] considered several tissues not considered by BEIR VII and UNSCEAR, including tumors of the oral cavity and esophagus. **Figures 3.1 and 3.2** compare these models for the %-REIC using identical U.S. population rates from 2005[99] and a DDREF value of 1.75. **Appendix A** contains tables of estimates of REIC and REID for several cancer types. In **Appendix B** we consider estimates for specific demographic factors within the U.S. population. Lung cancer makes the largest contribution to the risk, and the differences between the additive and the multiplicative models for lung cancer risks are found to be substantial, which is well documented.[6] Importantly, the models predict REIC values about 2 times higher than REID, or about a 20% increase compared to the analysis of NCRP Report No. 132.[6]

3.4 Age at Exposure Dependence of Cancer

NCRP Report No. 98[98] recommendations to NASA with regard to the age dependence of career dose limits was a substantial change from the contemporary dose limits for astronauts, and was also distinct from radiation protection methods at other government agencies or nations.[27] Tables of career limits were calculated for a 10-y career under the assumption that exposures were distributed evenly over the 10-y period,[98] and the report noted that more detailed calculations are needed if other career lengths are considered. NCRP Report No. 132 employed similar methodologies to NCRP Report No. 98, although it used the revised human epidemiology findings that occurred between the publications of the different reports. **Table 3.1** compares the age-dependent dose limits from the two reports. The more recent report recommended reducing Effective dose limits by more than 2-fold below age 50 y compared to the former NCRP report.

The largest difference between the NCRP estimates from 2000 and the BEIR VII model or recommended NASA 2010 approach is the reduction of the age at exposure dependence of cancer risk estimates and dose limits, with a more than a 3-fold change over the possible ages of astronauts in the NCRP model compared to a less than 50% change in the incidence-based risk transfer model approach. **Figure 3.3** compares REID values for solid cancer risk in the two approaches. The upper panels for males and females compares calculations using the rates from LSS report 13, the UNSCEAR mortality fits (linear term only), and the BEIR VII model. The NCRP and BEIR VII calculations use an identical DDREF of 2, and the UNSCEAR result uses the linear term from an LQ fit with DDREF=1. All calculations use the 2005 U.S. population data and ν_T=0.5 for all tissues. The NCRP and UNSCEAR mortality transport models show a similar dependence on a_E, and would be in even closer agreement if the UNSCEAR model were applied with a DDREF of about 1.3, or if the NCRP model DDREF was reduced from 2 to about 1.7. The

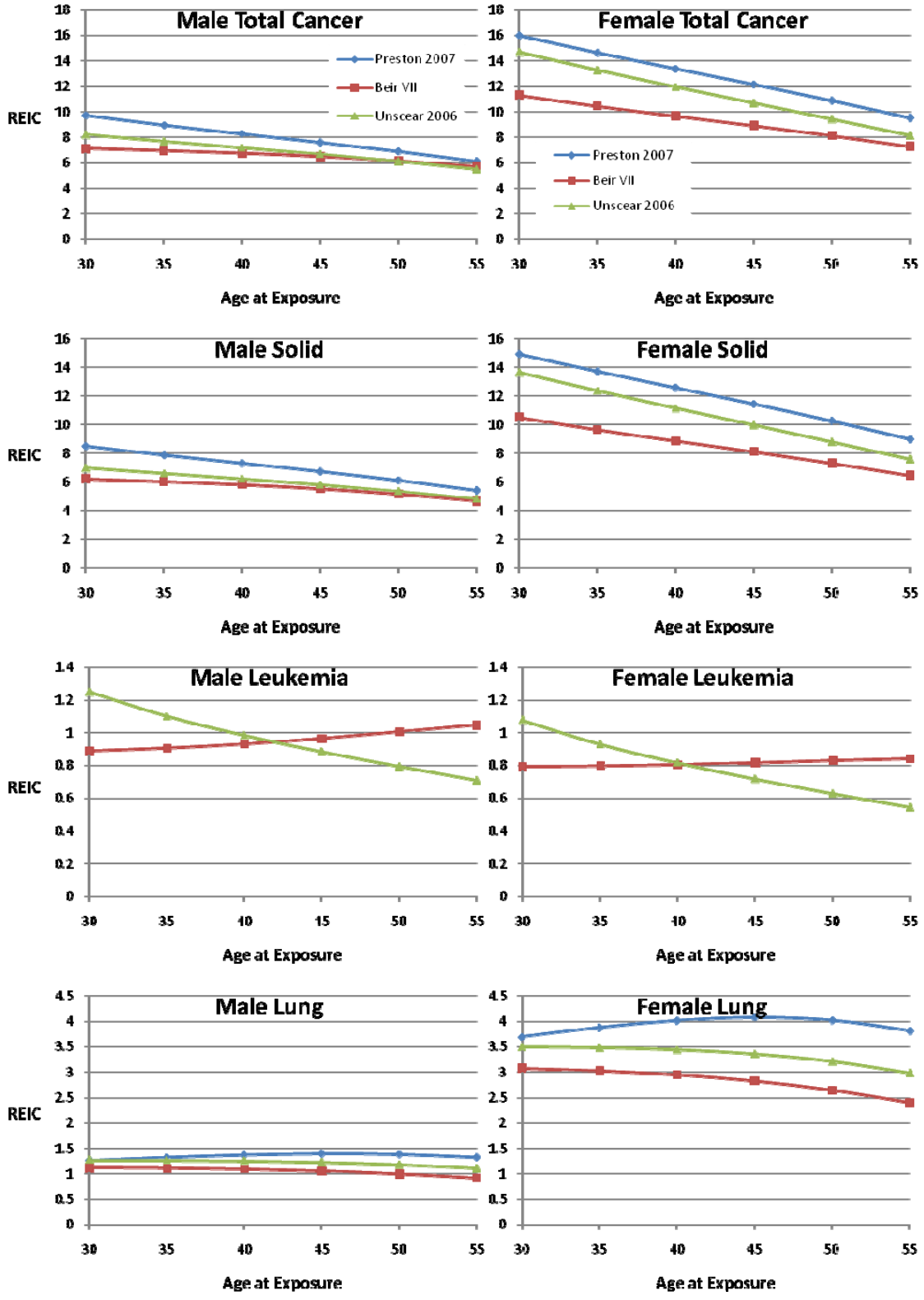

Figure 3.1. Comparison of %REIC per Sv for males and females as a function of age at exposure for mixture model U.S. for the BEIR VII, UNSCEAR, and Preston et al[92] tissue-specific cancer rates. Left panels for males; right panels for females.

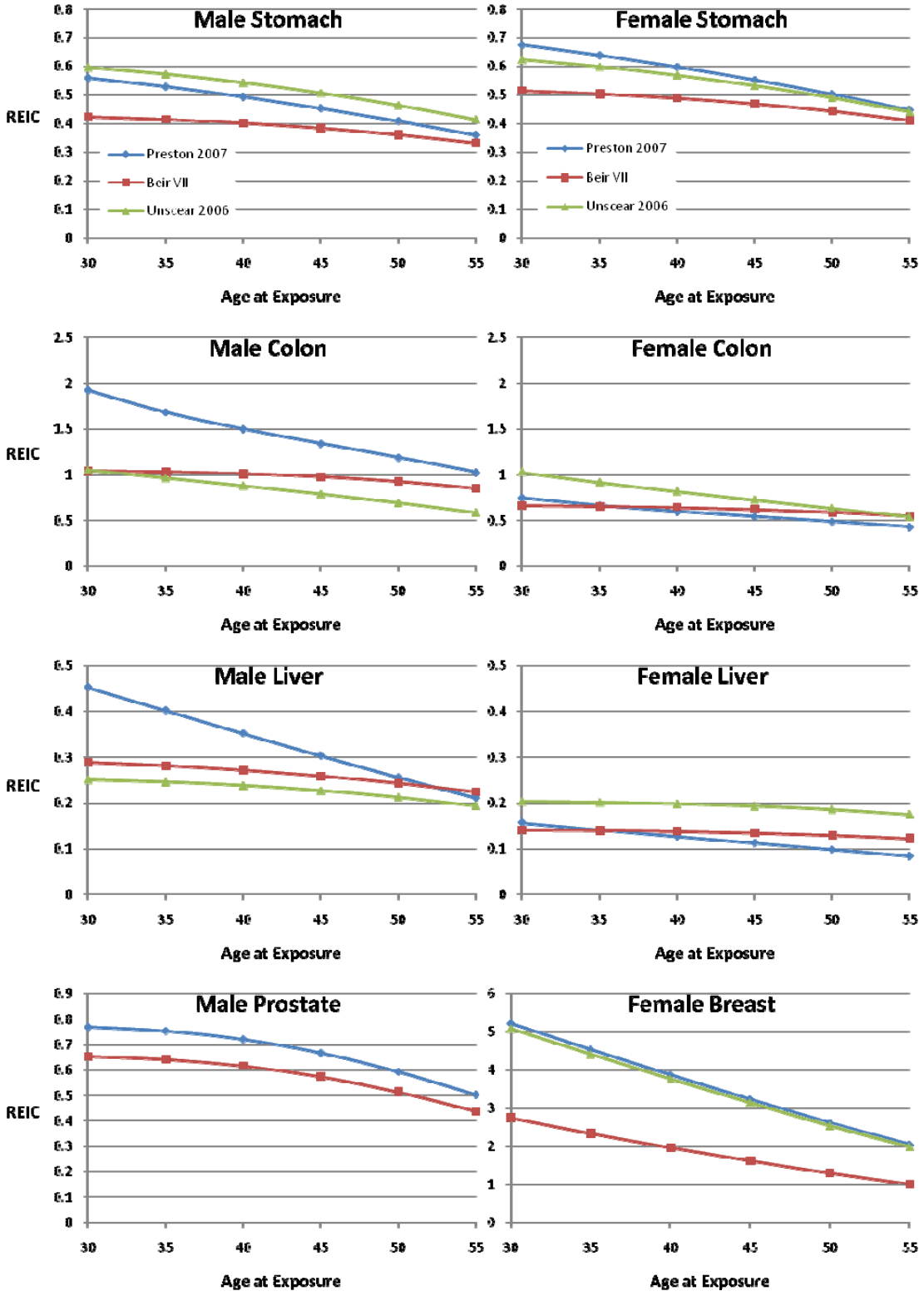

Figure 3.2. Comparison of %REIC per Sv for males and females as a function of age at exposure for mixture model and for the BEIR VII, UNSCEAR, and Preston et al[92] tissue-specific cancer rates. Left panels for males; right panels for females.

The BEIR VII model shows a very different a_E dependence. These assumptions have much larger impacts than those that would result from suggested changes to DDREF values recommended by the BEIR VII report[16] in which a DDREF of 1.5 increases the solid cancer risk estimate by 33% compared to a DDREF of 2 used in the past, and a smaller overall change when leukemia risk is included for the total cancer risk. The lower panels in **Figure 3.3** show calculations using transport of incidence rates converted to REID using the BEIR VII approach. A much weaker dependence on a_E is predicted compared to REID calculations based on the transport of mortality rates. The incidence-based transfer model makes good sense when one considers the changing rates for incidence and mortality over time since 1945, and differences between LSS and U.S. background rates. Cancer mortality rates in the U.S. are reported to be decreasing, while incidence rates remain more stable[100] except for lung cancer due to the reductions in tobacco usage.[101] The ratio of mortality to incidence is expected to continue to change in future if cancer treatments improve.

Table 3.1. Comparison of NCRP recommendation for career radiation limits for different ages at first exposure corresponding to a 3% risk of fatal cancer for 10-y careers from NCRP Report No. 98[98] to NCRP Report No. 132.[6] Values for other career lengths require a separate evaluation.

	E(Sv), NCRP Report No. 98		**E (Sv), NCRP Report No. 132**	
Age at Exposure, y	Female	Male	Female	Male
25	1.0	1.5	0.4	0.7
35	1.75	2.5	0.6	1.0
45	2.5	3.2	0.9	1.5
55	3.0	4.0	1.7	3.0

The biological basis for the age at exposure dependence of cancer risks should be considered with regard to the age dependences of radiation risks for astronauts with typical ages between 30 and 60 y. Radiation action as either a cancer initiator or promoter could be suggested to lead to differences in the age at exposure dependence of risk, and there are other competing biological factors to consider. Adults likely contain a much higher number of premalignant cells than do preadults.[16,17] However, differences in cell numbers for different ages of astronauts or between the average U.S. population and a population of healthy workers such as astronauts is unknown. The probability of a likely smaller population of preneoplastic cells being modified at low dose and dose-rates compared to normal cell populations should be considered in relationship to its relative probabilities of transformation. Aberrant changes to the tissue microenvironment[102] could increase with age, perhaps acting as a promotional effect for cells damaged from radiation exposure. The role of age in relationship to changing numbers of senescent cells, stem cells, or other susceptible cells and possible reduced DNA repair capacity could also be considered. Test of the LSS data for an increasing risk with a_E, as motivated by promotional effects considerations, were made by Little[94] and were not supportive of such a hypothesis.

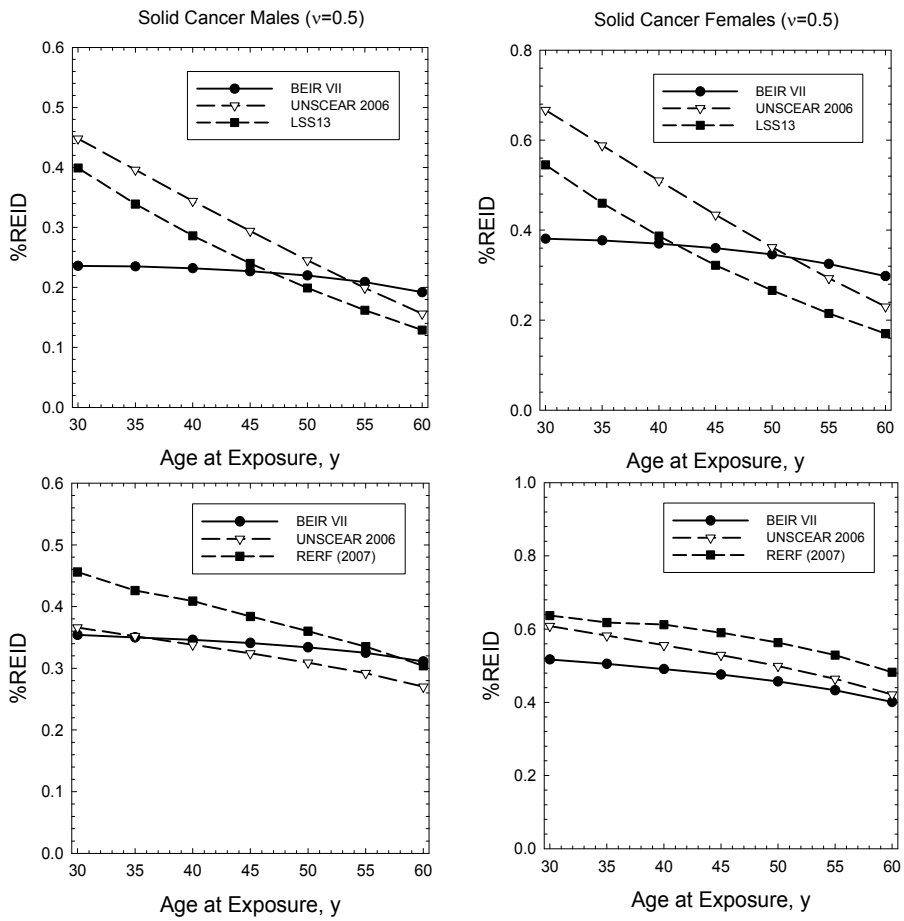

Figure 3.3. %REID per 0.1 Sv for solid cancer calculations in different models. Upper panels for males (left upper panel) and females (right upper panel) the %REID using mortality rate transport models. Lower panels show results using incidence rate transport models for males (left lower panel) and females (right lower panel).

3.5 Radiation Risks for Never-smokers

Astronauts and many other radiation workers or medical patients exposed to radiation for diagnostic reasons share common healthy attributes such as good nutritional and exercise habits and abstinence from smoking. More than 90% of astronauts are never-smokers (lifetime use less than 100 cigarettes) and the remainder are former smokers. The choice of a reference population to estimate risks was not considered in the past, at which time the average U.S. population was assumed in the NCRP projection models used at NASA. The reference population enters risk calculation in two ways: First, risk models consider competing causes of death from non-radiation risks, by which longer life span increases lifetime radiation risk. Second, multiplicative or additive risk transfer models for applying data from exposed populations to the reference populations are used in the risk models, with the multiplicative risk projection proportional to the cancer risks in the population under study. A military aviation population could be an appropriate choice for reference population data for the astronauts; however, data of sufficient accuracy have not been reported. Instead, we studied how cancer and all causes of death rates for the 50 U.S. states and the District of Columbia as well as other demographic factors affected risk calculations.

These data[99] show a wide variation in average life span and age-specific cancer rates, but we found that they result in only a small variation of REID probabilities.

The influence of the U.S. average rates for all causes of death and cancer incidence or mortality as an appropriate population on which to base risk assessments for healthy workers such as astronauts was investigated. Calendar year differences in rates occur, and comparison of U.S. rates from 1999 through 2005 showed a small trend toward increasing radiation risk as longevity increased. **Table 3.2** shows the average, SD, and minimum and maximum values based on the range of values for each of the 50 U.S. states and Washington DC using NCRP Report No. 132 and BEIR VII models using mixture models (**see also Supplementary Data in Appendix B**). A very small variation of REID estimates was observed in these comparisons. **Figure 3.4** shows the correlation between median life span and age-adjusted cancer rates with REID projections using %REID per Sv estimates in the BEIR VII model, with DDREF=1.5 for each state in the U.S. and Washington DC vs. the median life span and fatal cancer rates for females (upper panel) and males (lower panel) exposed at age 30 y. Trends are for small REID increases with longer life spans, and small REID decreases with decreasing cancer rates. These differences are closely tied to the assumptions of additive or multiplicative risk transfer, with larger changes found if multiplicative risk transfer is assumed.

Lung cancer incidence and mortality rates for never-smokers were recently compiled by Thun et al[103] from an analysis of never-smokers in 13 cohorts and 22 cancer registries. Furthermore, Furukawa et al[104] considered several interaction models between smoking and radiation in the A-bomb survivor cancer incidence data. A generalized multiplicative model for the combined effects of radiation and smoking was similar in form to Eq(3.9) for the radiation components, but with distinct coefficients. For never-smoker risk estimates, we adjusted the survival probability for the average U.S. population by adjusting the age-specific rate for all causes of death for lung cancer rates for never-smokers of Western European descent.[103] We considered other radiogenic cancers that are also linked to tobacco use, including cancers of the stomach, esophagus, oral cavity, and bladder. Age-specific rates for never-smokers for these cancers were not available. Instead, adjustments to rates for an average U.S. population were made using gender-specific relative risks for never-smokers,[101] which are given in **Table 3.3**. These rates are applied to the portion of rates corresponding to multiplicative risk transfer. Other radiogenic cancers are not counted as smoking attributable by the Centers for Disease Control (CDC),[105] although acute myeloid leukemia (AML) shows a small effect for smokers, and smoking contributions to breast cancer risk are also a possible concern.[106]

A significant decrease in REID and REIC probabilities compared to calculations for the average U.S. population was observed when lung cancer risk calculations were estimated for never-smokers. **Figure 3.5** shows comparisons between the data of Thun et al[103] with the SEER 2005 average U.S. population data for lung cancer incidence and mortality rates. We used these rates to estimate lung cancer risks in the BEIR VII, UNSCEAR, and RERF models as shown in **Tables 3.4 and 3.5** for estimates of REIC and REID, respectively. A more than 8-fold decrease is estimated in the multiplicative transfer model when never-smoker rates are compared to the U.S. population average. The model of Furukawa et al[104] leads to a minor reduction for females compared to the usage of never-smoker baseline rate estimates alone, and is about the same for males. We note that Furukawa et al[104] used lung dose estimates for the LSS cohort, while the reports noted above used colon doses to represent all solid cancer risks including the risk of lung cancer. Using a mixture model with v_T=0.5 reduced the lung cancer estimate for never-smokers by 2-fold compared to the average U.S. population. Because lung cancer is the largest contributor to overall radiation cancer risks, these lower estimates for never-smokers have large impacts on overall risk estimates.

Table 3.2a. Variation of %REID per Sv for females in individual states and Washington DC vs. age at exposure in models of BEIR VII (DDREF=1.5) and the NCRP 132 (DDREF=2).

			BEIR VII					
State	Median life span	Cancer rate	35	45	55	35	45	55
Average	82.4	133.8	5.4	5.2	4.7	4.7	3.5	2.3
Standard Deviation	1.1	17.1	0.2	0.2	0.2	0.2	0.1	0.1
Minimum	80.1	89.6	4.8	4.6	4.2	4.3	3.2	2.1
Maximum	85.6	165.6	5.7	5.5	5.1	5.0	3.8	2.5

Table 3.2b. Same as Table 3.2a for males.

			BEIR VII			NCRP 132		
State	Median life span	Cancer rate	35	45	55	35	45	55
Average	77.7	150.6	3.9	3.8	3.6	3.9	2.9	2.0
Standard Deviation	1.8	30.9	0.2	0.1	0.1	0.1	0.1	0.1
Minimum	73.2	96.0	3.5	3.4	3.3	3.6	2.7	1.8
Maximum	80.3	219.0	4.2	4.1	3.8	4.1	3.1	2.1

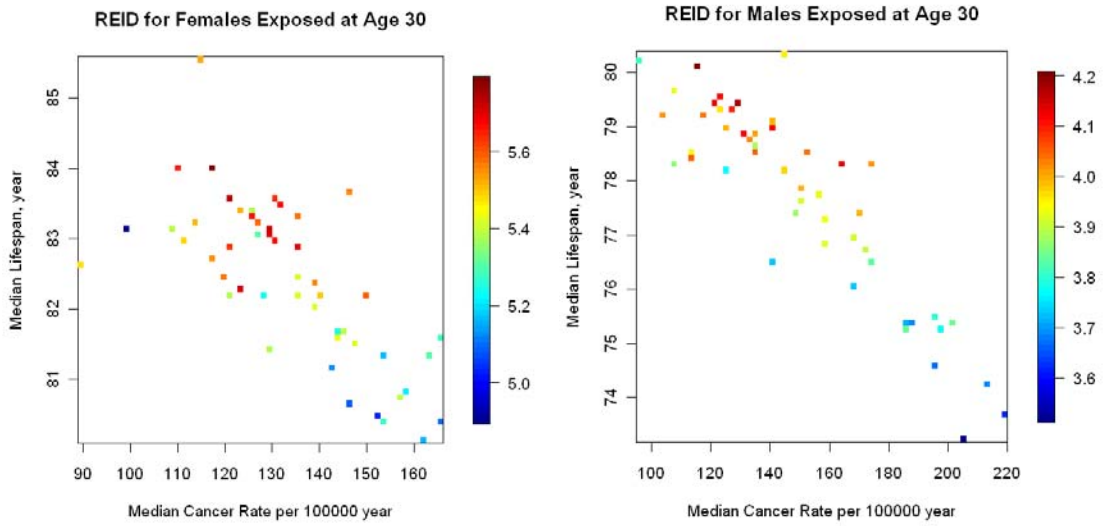

Figure 3.4. %REID per Sv estimates in the BEIR VII model, with DDREF=1.5 for each state and Washington DC vs. median life span and fatal cancer rates for females (left panel) and males (right panel) exposed at age 30 y.

Very little information has been reported for contributions for different lung cancer histologies to radiation risk, such as the fraction from small cell lung carcinoma (SCLC) vs. non-small cell lung carcinoma (NSCLC), in part due to statistical limitations. Much more is known for the histologies of lung cancers associated with tobacco use.[107] Land et al[108] reported that radiation lung cancer mortality risks were mostly associated with SCLC in the A-bomb survivors and uranium miners who received doses from α-particles. A study of Hodgkin's disease patients treated with high

doses of radiation in Europe and the U.S. indicated that NSCLC was associated with radiation exposure, and no significant risks for never-smokers.[109] For high-LET α-particles, the BEIR VI committee found sub-multiplicative models fit data for uranium miners the best, and ruled out additive risk models.[110] The choice of risk transfer model is a major uncertainty because never-smokers have a very small incidence of SCLC in the U.S., suggesting that additive risk transfer should be used to transfer the LSS data to the U.S. for SCLC risk, or else no risk of SCLC cancer would be predicted for never-smokers.

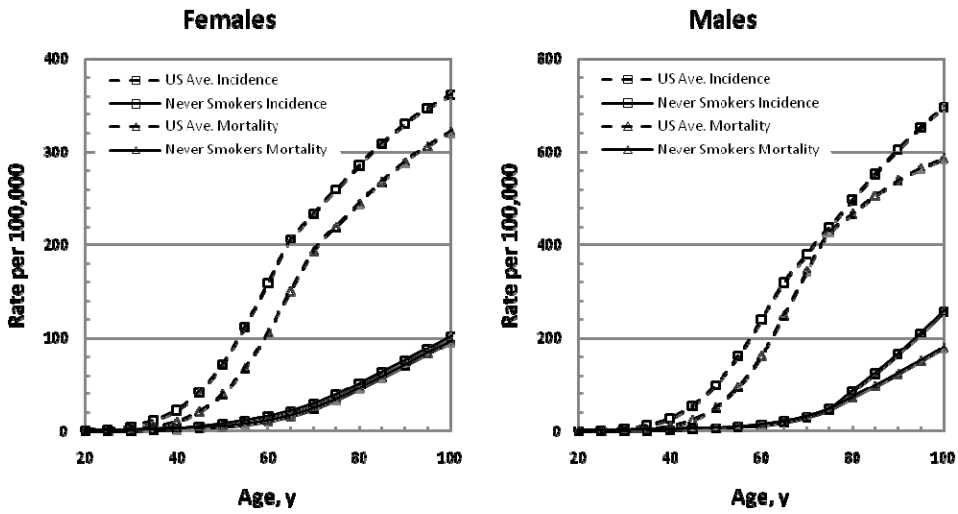

Figure 3.5. Comparison on age-specific cancer incidence and mortality rates for the 2005 U.S. average population and recent analysis for never-smokers by Thun et al.[103] Left panel for females, and right panel for males.

Table 3.3. Estimates of relative risks (RRs) for never-smokers (NS) compared to U.S. average population for several cancers attributable to both smoking and radiation exposure. For males, current smokers, former smokers, and NS are estimated at 24%, 40%, and 36% of the population above age 50 y. For females, we use 18%, 35%, and 47% of the population above age 50 y.

	RR to Never-smokers (NS)			RR for NS to U.S. Avg.
Males	**Current smokers**	**Former smokers**	**NS**	**RR (NS/U.S.)**
Esophagus	6.76	4.46	1	0.27
Stomach	1.96	1.47	1	0.71
Bladder	3.27	2.09	1	0.50
Oral Cavity	10.89	3.4	1	0.23
Lung*	23.26	8.7	1	0.11
Females	**Current smokers**	**Former smokers**	**NS**	**RR (NS/U.S.)**
Esophagus	7.75	2.79	1	0.35
Stomach	1.36	1.32	1	0.85
Bladder	2.22	1.89	1	0.65
Oral Cavity	5.08	2.29	1	0.46
Lung*	12.69	4.53	1	0.23

*Lung data shown only for comparison; with calculations in report using age-specific rates described in the text.

Table 3.4. Lung cancer incidence per Sv (REIC/Sv) in several models with DDREF = 2.

		%REIC, Females			%REIC, Males		
	Age at Exposure	**35 y**	**45 y**	**55 y**	**35 y**	**45 y**	**55 y**
Model Type	**Model rates**	**Average U.S. Population, 2005**					
Additive	BEIR VII	1.34	1.33	1.31	0.77	0.76	0.74
	UNSCEAR	1.60	1.57	1.42	0.86	0.83	0.78
	RERF	1.67	1.66	1.59	0.87	0.87	0.83
Multiplicative	BEIR VII	3.92	3.61	2.97	1.23	1.15	0.96
	UNSCEAR	4.65	4.49	3.98	1.45	1.41	1.27
	RERF	5.15	5.56	5.28	1.51	1.65	1.60
Mixture	BEIR VII	2.70	2.54	2.19	0.99	0.96	0.85
	UNSCEAR	3.14	3.03	2.73	1.15	1.12	1.02
	RERF	3.43	3.63	3.46	1.19	1.26	1.21
		Never-smokers					
Multiplicative	BEIR VII	0.54	0.50	0.44	0.16	0.17	0.16
	UNSCEAR	0.69	0.67	0.62	0.17	0.17	0.16
	RERF	0.70	0.76	0.77	0.15	0.17	0.18
Mixture	BEIR VII	1.01	0.99	0.93	0.45	0.44	0.42
	UNSCEAR	1.15	1.12	1.04	0.51	0.50	0.47
	RERF	1.18	1.21	1.18	0.51	0.52	0.50
Generalized Multiplicative	RERF, Generalized Multiplicative for never-smokers	0.50	0.58	0.62	0.16	0.19	0.22

Table 3.5. Fatal lung cancer risks per Sv (REID/Sv) in several models with DDREF=2.

		%REID, Females			%REID, Males		
	Age at Exposure	**35 y**	**45 y**	**55 y**	**35 y**	**45 y**	**55 y**
Model Type	**Model rates**	**Average U.S. Population, 2005**					
Additive	BEIR VII	1.20	1.20	1.18	0.65	0.66	0.66
	UNSCEAR	1.28	1.27	1.22	0.71	0.71	0.69
	RERF	1.33	1.34	1.32	0.72	0.73	0.73
Multiplicative	BEIR VII	2.88	2.74	2.38	0.95	0.92	0.83
	UNSCEAR	3.56	3.50	3.23	1.17	1.17	1.11
	RERF	3.71	4.16	4.21	1.13	1.30	1.37
Mixture	BEIR VII	2.04	1.97	1.78	0.80	0.79	0.74
	UNSCEAR	2.43	2.39	2.23	0.94	0.94	0.89
	RERF	2.53	2.77	2.78	0.92	1.02	1.05
		Never-smokers					
Multiplicative	BEIR VII	0.44	0.41	0.37	0.15	0.15	0.14
	UNSCEAR	0.57	0.57	0.54	0.15	0.15	0.14
	RERF	0.55	0.61	0.66	0.14	0.15	0.16
Mixture	BEIR VII	0.85	0.84	0.81	0.40	0.40	0.38
	UNSCEAR	0.96	0.95	0.91	0.46	0.45	0.42
	RERF	0.98	1.01	1.02	0.46	0.47	0.45
Generalized Multiplicative	RERF, Generalized Multiplicative for never-smokers	0.39	0.47	0.53	0.16	0.17	0.20

4. Uncertainties in Low-linear-energy-transfer Risk Model Factors

NCRP Report No. 126[15] reviewed uncertainties for low-LET radiation risk assessments, and the recommended PDFs were used by NASA for its previous space radiation risk assessments.[14,21] Several reports published since 1997, as noted above, provide new sources of information to update uncertainty assessments. We first summarize NCRP Report No. 126 and then describe other information to update the low-LET uncertainty PDFs. For Monte-Carlo sampling purposes, the low-LET mortality rate per Sievert, λ_L, is written as

$$\lambda_L(E, a_E, a) = \frac{\lambda_0(a_E, a)}{DDREF} \frac{x_D x_S x_T x_B x_U}{x_{Dr}} \tag{4.1}$$

where λ_0 is the baseline mortality rate per Sievert and the x_α are quantiles (random variables) whose values are sampled from an associated PDF, $P(x_\alpha)$. Note that the DDREF applies only to the solid cancer risk and not to the leukemia risk under the given assumptions. NCRP Report No. 126[15] defined the following subjective PDFs, $P(x_\alpha)$, for each factor that contributes to the low-LET-risk projection:

1) $P_{dosimetry}$ represents random and systematic errors in the estimation of doses received by atomic-bomb blast survivors. It was assumed by the NCRP as a normally distributed PDF for bias correction of random and systematic errors in the dosimetry (DS86) with a mean of 0.84 and an SD of 0.11.
2) $P_{statistical}$ represents the distribution in uncertainty in the risk coefficient r_0. It is assumed as a normally distributed PDF with a mean of 1 and an SD of 0.15.
3) P_{bias} represents any bias resulting for over-reporting or underreporting of cancer deaths. P_{bias} is assumed as a normal distribution with a most probable value of 1.1 and a 90% CI from 1.02 to 1.18 corresponding to an SD of 0.05.
4) $P_{transfer}$ represents the uncertainty in the transfer of cancer risk following radiation exposure from the Japanese population to the U.S. population. Both additive and relative risks models were considered by NCRP Report No. 126[15] in assessing the uncertainties in such transfer. $P_{transfer}$ is log-normal with a mean of 1 and an SD of 0.26 (GSD [geometric standard deviation]=1.3).
5) P_{Dr} represents the uncertainty in the knowledge of the extrapolation of risks to low dose and dose-rates embodied in the DDREF. The NCRP assumed P_{Dr} to be a truncated triangle distribution starting at 1 and ending at 5 with a peak at 2 and a relative value of ¼ or ½ at 1 or 5, respectively, compared to the peak values for the DDREF at 2. This PDF is used to scale the low-LET risk coefficient (mortality rates) in our estimates for space radiation.
6) P_U represents unknown uncertainties. The NCRP assumed this uncertainty followed a normal distribution with a central value of 1 and an SD of 0.3 with 90th-percentile subjective CIs of [0.5, 1.5].

The NCRP also considered a PDF for bias correction in projection of cancer risks over a lifetime, which is important for those exposed below age 30 y but not for astronauts. The lifetime projection and NCRP-unknown uncertainties were ignored in the previous NASA model.

The analysis and data for updating low-LET cancer risk assessments and uncertainties since NCRP Reports Nos. 126 and 132 are as follows:

1) Publication of the revised atomic-bomb dosimetry assessment[96] for the LSS of survivor called dosimetry system 2002 (DS02).
2) Longer follow-up and reanalysis of the LSS cancer incidence data by BEIR VII,[16] UNSCEAR[17] (see also Little et al[10]), and Preston et al.[92]
3) Meta-analysis of other human epidemiology models for breast and thyroid cancer risks (BEIR VII).
4) Development of empirical Bayes and Bayesian models for tissue-specific cancer incidence data that represent significantly reduced tissue-specific statistical errors,[95,111] respectively.
5) Assessment of dose response models fitted to human data sets and in the evaluation of DDREF values, including the BEIR VII analysis[16] and analysis of radiation worker studies that support a DDREF value near unity.[97]

4.1 Life-span Study Dosimetry Errors

Errors in dosimetry related to epidemiology data include random and systematic errors. The completion of the revised dosimetry of the atomic-bomb survivors, called dosimetry system 2002, DS02,[94] led to minor reductions in the neutron dose estimates as well as modest changes in estimates of the γ-ray organ doses compared to the earlier DS86. Recent analysis by BEIR VII, UNSCEAR, and Preston et al.[112] assume larger dosimetry errors than that of NCRP Report No. 126.[15] The DS86 evaluation was subjectively assessed in light of the anticipated dosimetry reevaluation that cumulated in the newer DS02 system. The UNSCEAR report made a Bayesian analysis of dosimetry errors.[10,17] Preston et al[92] assume an overall 35% error in DS02 estimates. UNSCEAR assumed a log-normal distribution with a GSD of 30%. Other reports[112-114] estimate the impact of using a fixed-neutron RBE of 10 in fitting the A-bomb data and other errors. Here, since a larger RBE value and a dose-dependent value are plausible, especially for solid cancers based on radiobiology experiments with cells and small animals, an overall reduction in the γ-ray-derived risk coefficients would be expected. A dose-dependent RBE tested by Suzuki et al[112] indicated that reductions as high as 30% in the γ-ray risks were plausible if the neutron RBE actually had a much higher value than the 10 that was assumed in recent reports. Another source of error is the use of stratified dose groups instead of individualized dose estimates.[10] Tissue sites in which meta-analysis over several exposed cohorts is considered introduces other dosimetry considerations. Cohorts exposed for medical conditions often involved x-ray exposures that have RBEs of two or more compared to γ-rays at low doses.[115-117] Underreporting of doses from other sources is also a potential bias**. After considering these various descriptions and the previous NCRP Report No. 126 assessment, we assume a log-normal PDF for the combined dosimetry uncertainties with a geometric mean of 0.9 and GSD of 1.3. This represents a significant increase in dosimetry error compared to the NCRP Report No. 126 recommendation.**

4.2 Statistical Errors

NCRP Report No. 126 represented statistical errors by a normal PDF with a mean of 1 and an SD of 0.15. It would be expected that the SD would improve with continued analysis and longer follow-up times. Pawel et al[95] found, using so-called Empirical Bayes (EB) models, that tissue-specific statistical errors are much better represented when all data are assumed to originate from a common parent distribution. A result of this analysis is reproduced in **Table 4.1**. For our subjective PDF representing statistical errors, we assume a normal distribution with a mean of 1 and an SD of 0.15 to represent the overall cancer risk estimate. Estimates of statistical uncertain-

ties for individual sites can be made with the larger values suggested by the EB model; however, these uncertainties would be small compared to DDREF or radiation quality uncertainties.

4.3 Errors from Reporting Bias

We estimated the REID probabilities based on the cancer incidence data in this report while NCRP Report Nos. 132 and 126 used cancer mortality data. As noted by NCRP Report No. 126, errors in incidence data are expected to be smaller than those of mortality data. We assumed a normal distribution with a mean of 1 and a standard error of 0.05 for the reporting bias error.

Table 4.1. Comparison of maximum likelihood estimates (MLEs) to EB method for gender-adjusted, site-specific ERR from the LSS.[95]

	ERR/Sv Estimate		Standard Error	
Tissue	**MLE**	**EB**	**MLE**	**EB**
Kidney	0.40	0.40	0.32	0.19
Esophagus	0.63	0.48	0.31	0.19
Prostate	0.18	0.32	0.30	0.19
Bladder	0.84	0.58	0.29	0.18
Pancreas	0.38	0.39	0.22	0.15
Remainder	1.15	0.85	0.19	0.15
Ovary	0.27	0.32	0.19	0.15
CNS	0.37	0.38	0.17	0.14
Oral Cavity	0.34	0.36	0.15	0.13
Lung	0.70	0.63	0.13	0.11
Gallbladder	-0.01	0.08	0.13	0.11
Colon	0.49	0.47	0.11	0.10
Rectum	0.14	0.19	0.10	0.10
Liver	0.31	0.32	0.10	0.09
Breast	0.67	0.63	0.10	0.09
Stomach	0.32	0.32	0.06	0.06
Uterus	0.04	0.05	0.05	0.05

4.4 Dose and Dose-rate Reduction Effectiveness Factor Uncertainties

The DDREF applies to solid cancer risk estimates over the appropriate range of equivalent organ doses and dose-rates to be expected in space. ISS missions lead to crew doses of 0.02 to 0.06 Gy and Effective doses of about 0.05 to 0.15 Sv. To date, the highest lifetime Effective dose for astronauts has been about 0.3 Sv.[73] For exploration missions, Effective doses as high as 1.5 Sv could occur. Dose-rates in space range from about 0.3 to 0.6 mGy/d for GCR. A large SPE would have maximum dose-rates at deep tissues for modest spacecraft shielding amounts of about 0.3 Gy/hr. These values suggest that experimental information for γ-rays for DDREFs that are applicable for doses from about 0.05 to 2 Gy are the most appropriate for the NASA risk estimates. This is distinct from exposure to the public or terrestrial workers, to whom exposures below 0.05 Gy are the major concern. NCRP Report No. 98[98] recommends a dose-rate effectiveness factor (DREF) of 2.5. NCRP Report No. 132[6] recommends a DDREF of 2.0. The BEIR VII report[16] recently recommended a DDREF of 1.5 based on a Bayesian analysis of the LSS data

and selective mouse tumor data. Reducing the DDREF from 2.0 to 1.5 would increase the solid cancer risk estimates by 33% with all other factors the same.

The UNSCEAR reports that best-fitting model to the LSS total solid cancer mortality data was an LQ dose response model, however, differences between fits using linear and LQ response models were consistent with the DDREF values reported by BEIR VII (**Table 4.2**). The NCI radio-epidemiological assessment model[93] considers a weighted discrete distribution of DDREF values with a mean value from the distribution of about 1.75. A recent meta-analysis of 12 radiation worker studies by Jacobs et al[97] suggests a DDREF of 0.83 [0.53, 1.96] when these data are compared to the LSS. However, other differences between populations, and adjustments for dose protraction and a photon RBE different than unity for different types of low-LET exposures are confounding factors in a comparison of radiation worker data to the LSS data.

The use of LSS data to make DDREF estimates raises some conceptual issues. It is well known that the curvature or quadratic component of any dose response in the LSS is small and, of course, there were no exposures at low dose-rate. The lack of curvature could be due to inherent uncertainties in the data or the impact of pooling data from a heterogeneous population. Data for individual tumors have larger statistical limitations than overall solid cancer mortality risk; however, these data appear to be even better represented by linear dose response than by the mortality data in which UNSCEAR finds a linear-quadratic model a better choice for the latter. If the response is truly linear, a dose-rate dependence related to linear induction mechanisms should be considered. Also, these more recent lower DDREF estimates raise important issues as to the appropriateness of experimental data in human cell culture models or strains of mice that often show a significant quadratic dose response component.

Several concerns arise in the BEIR VII analysis of animal data. First, BEIR VII did not consider all animal tumor data available but only a small set of such data. Second, mouse leukemia and lymphoma data were pooled with solid tumor data in the BEIR VII analysis of the DDREF; these data apply only to solid cancer risk estimates in humans. Certain mouse tumor types included are also believed to be poor models of human cancers. A notable example of this is ovarian tumors in mice, which seem to be inappropriate because the mechanisms for their induction is believed to be cell killing. Further, the report did not consider surrogate endpoint data in human cells, which would show a large range of DDREF values, and suggests that biological responses are through distinct mechanisms at low doses (< 0.1 Gy) compared to high doses of more than 1 Gy.

We evaluated data in the literature for other mouse tumor studies not considered by BEIR VII, as well as for surrogate cellular endpoints including mutation, neoplastic transformation, and chromosomal aberrations. A wide range of DDREF values from unity to approximately 10 can be found. Of note is the studies by Loucas and Cornforth[118,119] of chromosomal aberrations using MFISH [multicolor fluorescence in-situ hybridization], which found a linear response for acute effects and a dose-rate reduction factor for chronic irradiation of more than 5 albeit both dose response curves were adequately described as linear. **Table 4.3** shows a survey of different recommendations and data sets. An average value that is slightly less than 2 is estimated. **Based on available information, we chose to use the National Institutes of Health (NIH) report[93] mean value of DDREF=1.75, which is intermediate between the BEIR VII and the NCRP Report No. 132 recommendations. We assume a log-normal PDF for the DDREF uncertainty with a geometric mean (GM)=1 and GSD=1.4 as shown in Figure 4.1.**

Table 4.2. Summary of various estimates of the DDREF from human or experimental studies with cells and animals.

Estimate or Recommended Value	DDREF Estimate
***NCRP Report No. 98[98]**	2.5
NCRP Report No. 132[6]	2
BEIR VII: selected mouse tumor studies	1.5 [1.0, 4.4]
BEIR VII: LSS data analysis	1.3 [0.8, 2.6]
BEIR VII: Combined Bayesian Analysis	1.5 [1.1, 2.3]
ICRP[117]	2
***UNSCEAR[17]**	1.22
NCI[93]	1.75
Jacob et al[97] Radiation-Worker studies vs. LSS	0.83 [0.53, 1.96]
Oncogenic changes in cell culture models	~1 to > 10
***Solid tumors in mice from NCRP Report No. 64[120]**	3.48
NASA 2010 model	1.75

*NCRP used the related quantity DREF instead of DDREF.
**UNSCEAR did not make a DDREF recommendation; however, a comparison of its fitted LQ and linear dose response models to LSS data leads to value shown.

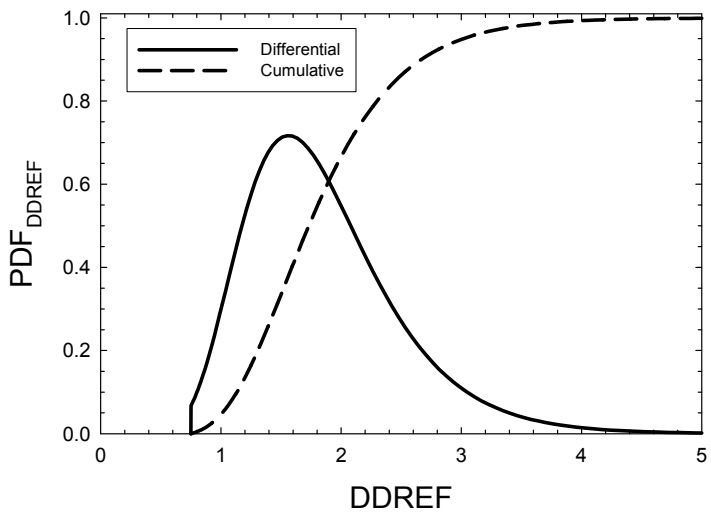

Figure 4.1. Monte-Carlo results for a sampling of log-normal distribution for the DDREF uncertainty with the values DDREF=1.75, GM=1, and GSD=1.4. The distribution is truncated at 0.75, which allows a 0.05 probability of an inverse dose-rate effect where DDREF<1.

4.5 Transfer Models Uncertainties

Two models are often considered for transferring radiation-associated incidence or mortality rates from other populations such as the Japanese to a U.S. population. The multiplicative transfer model uses the fitted ERR functions and assumes radiation risks are proportional to spontaneous or background cancer risks. The additive transfer model uses fitted EAR functions such that radiation acts independently of other cancer risks. The NCRP recommends[6] a mixture model for solid cancers with equal additive contributions from the multiplicative and the additive transfer models. For leukemia risk, the additive transfer model was recommended.

Table 4.3 Tissue-specific transfer weight ν_T for multiplicative risk transfer. Additive risk transfer weight is $1-\nu_T$.

Tissue	NCRP No. 132	BEIR VII	NASA 2010
Lung	0.5	0.3	0.5
Breast	0.5	0*	0
Thyroid	0.5	1.0*	1.0
Digestive system (stomach, colon, kidney, esophagus)	0.5	0.7	0.7
Leukemia	0.0	0.7	0.5
All Others	0.5	0.7	0.5

*Based on meta-analysis results described in BEIR VII.[16]

There are several considerations with regard to which transfer model is appropriate, least considered of which is the possibility of radiation quality dependence of the transfer model. Additive risk transfer models suggest that radiation acts independently of promotional effects in the population under study. Multiplicative risk transfer models suggest that radiation acts independently of other cancer initiators in the population under study.[16] Mouse tumor induction studies with γ-rays suggest the multiplicative transfer model is correct for solid cancers and additive transfer for leukemia.[121] The transfer model should depend on tissue type if distinct mechanisms leading to cancer act in different tissues. There could also be transfer model dependences on age at exposure since older persons compared to younger ones are presumed to have more initiated cells, altered DNA repair capacity, a higher fraction of senescent cells, etc. The transfer model may also depend on radiation quality if HZE nuclei and neutrons produce tumors through different mechanisms than γ-rays, or on dose if distinct mechanisms of carcinogenesis occur at high vs. low doses.

Lung cancer makes up the highest proportion of the overall cancer risks. BEIR VII assumed a higher weight for additive risk transfer for lung cancer based on the observation of additive interactions between smoking and radiation. BEIR VI,[110] in assessing the interaction between smoking and workers exposed to high-LET α-particles from radon, found a more than additive interaction. Because space radiation is comprised both of low- and high-LET particles, it is not clear which if any of these transfer weights is appropriate. **The results of Tables 3.4 and 3.5 imply that gaining the knowledge to decide which lung risk transfer model is correct potentially impacts to space radiation protection more highly than many other considerations, including improved forecasting of SPEs or adding large amounts of radiation shielding to spacecraft.** In our revised model, we assume equal weights for lung cancer transfer to the U.S. population as recommended in NCRP Report No. 132.[6] For cancers of the digestive system, a strong interaction with dietary factors is expected and BEIR VII assumes a higher fraction for the multiplicative transfer model with weight ν_T=0.7.

4.6 Baseline Cancer Rates and Life-table Data

Astronauts are surely classified as “healthy workers”; however, in the past, average U.S. population data have been used to estimate cancer risks.[6,98] Several types of uncertainties arise by assuming the average U.S. population to form the risk projection for astronauts. One uncertainty is the use of current calendar year data to project risks in the future. The Social Security Administration (SSA)[122] has assessed changes in median life-span. Recent data show a general trend for increase in life span and reduction in cancer mortality, while overall cancer

incidence remains roughly constant.[100] Errors due to future population evolution are not included in our uncertainty assessments, and are assumed as a model assumption. A second type of error is due to statistical limitations in population data at older ages, as reported by the NCI surveillance, epidemiology, and end results (SEER) program. Cancer incidence rates above age 85 y may have non-negligible SDs, and some reports suggest a downward curvature in these data that is perhaps caused by cell senescence. A sensitivity analysis was made by comparing radiation risks for the varying assumptions of monotonically increasing, downward curvature and constant rates above age 85 y. Because the fraction of a population alive above age 85 y is small, we found differences for overall cancer risks to be small (<5%) after comparing different models for extrapolation beyond age 85 y.

A third type of uncertainty is due to the choice of reference population, which is always assumed to be the average U.S. population. Alternative approaches would include the use of a military aviation population as the reference population for astronauts. However, incidence or mortality rates for pilots have large statistical errors and there are limitations in data collection.[123] To estimate the potential size of errors due to the choice of baseline rates, we collected life-table and age-specific all-cancers data from each of the 50 states and the District of Columbia in the U.S., all of which have a large range in life-span and age-adjusted cancer rates (**Appendix B**). We also compared, in **Appendix B**, these data to predictions by level of urbanization. From these comparisons SDs for REID estimates for the average U.S. population relative to the individual states or Washington DC were less than 5%, albeit there is substantial variation in median life span or background cancer rates over the range of values for each state. We therefore ignored assignment of any error related to the definition of a reference population. As noted above, the influence of smoking on background cancer rates and radiation risks in A-bomb survivor data is much larger. Statistical errors in population data for never-smokers are generally higher than those for the average U.S. population data from SEER,[99] and we introduced a normal distribution for these rates with M=1 and SD=0.15. However, when equal transfer weights are assigned for additive and multiplicative transfer models, the additive transfer model term dominates for never-smokers, thus reducing the importance of statistical errors in never-smoker cancer rates.

4.7 Summary of Past Uncertainty Analysis for Low-linear Energy Transfer Radiation

In **Table 4.4** we compare the NCRP Report No. 126 CIs to the more recent reports from BEIR VII and UNSCEAR. The results are for an average adult population. Although several differences in the assumptions of the different models occur, the comparison indicates about a 2-fold uncertainty at the 95% CL for low doses of low-LET radiation in each of the models.

Table 4.4. Comparison of model uncertainties from past reports on low-LET radiation cancer risks.

Analysis	%Risk for 0.1 Sv	Comment
NCRP Report No. 126	0.37 [0.115, 0.808]	Gender avg. with 90% CI
BEIR VII Males	0.48 [0.24, 0.98]	95% CI
BEIR VII Females	0.74 [0.37, 1.5]	95% CI
UNSCEAR Solid Cancer	0.502 [0.28, 0.735]	Gender avg. with 90% CI; DDREF uncert. not considered
UNSCEAR Leukemia	0.061 [0.014, 0.118]	Gender avg. with 90% CI

5. Cancer Risks and Radiation Quality

NASA currently uses the LET, *L*-dependent radiation QF function, *Q(L)* that was recommended by the ICRP[26] to estimate organ dose equivalents for space missions.[6,25,73] Organ doses are evaluated by a mass average of fluence spectra weighted by LET and QFs, *Q*(*L*) over each tissue contributing to solid cancer risks. For estimating leukemia risk, organ dose equivalents averaged over bone marrow sites as distributed in adults are used. As described by the NCRP,[25] NASA does not use the ICRP radiation weighting factors, which are defined for external fields at the surface of the human body, because of their imprecision and the complex nature of the radiation fields in space. The approach developed at NASA is supported by recommendations by the NCRP in its Report Nos. 132[6] and142.[25]

The ICRP[26] definition of the LET-dependent quality function is given by:

$$Q(L) \quad = \quad \begin{cases} 1 & L > 10 \quad keV/\mu m \\ 0.32L - 2.2 & 10 - 100 \\ 300/\sqrt{L} & L > 100 \end{cases}$$

The ICRP and NCRP have noted that the use of *Q*(*L*) or the alternative radiation weighting factors are simplifications because of lack of knowledge to assign a more precise relationship.

QFs are based on a subjective assessment of maximum RBE values, RBE_{max} for relevant endpoints from radiobiology experimentation. RBE_{max} is defined as the ratio of initial slopes for the radiation of interest to a reference radiation assuming that both radiation types have linear dose response curves at low dose and dose-rates. It is important to note that it is implicitly assumed that DDREFs are not used for ions because RBE_{max} values are the basis to assign QFs. Reference radiation should be taken as Cs or Co γ-rays to accurately represent LSS exposures. RBEs for ions can be underestimated if x rays with energies below about 300 kVp are used as the reference radiation because the RBE for x rays relative to γ-rays is greater than unity and observed to exceed 3 at low dose for some endpoints.[31] The ICRP and NCRP have noted limitations in radiobiology data to assess radiation QFs.[5,31] Other reports have discussed qualitative differences that might preclude the usage of QFs for estimating heavy ion effects.[1,5]

In this section, we review available radiobiology data for RBEs and discuss biophysical models of radiation quality effects. We will discuss a rationale for defining new radiation quality functions that will

1) Introduce distinct QFs for solid cancer and leukemia risk estimates.
2) Replace the QF LET dependence with a differential dependence on Z^{*2}/β^2 for light ($Z \leq 4$) and heavy ($Z > 4$) charged particles.
3) Discuss an alternative risk calculation using track-structure-based risk coefficients.
4) Revise the uncertainty assessment of QFs.
5) Provide an additional uncertainty assessment that considers a nonlinear dose response at low doses as suggested by NTE models of cancer risk.

Uncertainty analysis of radiation quality effects need to address several questions that arise with regard to the radiation quality function including:

1) Use of LET as a single parameter to describe the biological effectiveness of all particles in space, which includes charge numbers from Z=1 to 28, and energies corresponding to

low-energy recoil nuclei and stopping particles (<5 MeV/u) to relativistic ions with energies of 10 GeV/u or more.
2) The maximum value of Q to be used.
3) The shape of the Q function, including the slope in the rise to the maximum taken as linear by the ICRP, and the value of descending slope at high-LET or ionization density, which is taken as the power p= -1/2 by the ICRP.
4) Problems related to deviation from linearity and qualitative differences between HZE nuclei and low-LET radiation.

Experimental models of human cancer risks should be used to estimate the most meaningful RBE for risk assessment. The relevance of experimental models for human risks should be based on a small number of criteria,[124,125] including:

1) The model should represent tissues of interest for human risks.
2) The cell of origin for cancer risks in humans is considered.
3) Possible mechanisms of cancer risk are addressed.
4) Host factors that modify the expression of cancer in humans must be addressed.

Unfortunately, very few of the existing data sets on radiation quality fulfill one or more of these criteria, and very circumstantial endpoints have been used in the past to estimate RBEs for assessing cancer risks. NASA is supporting new studies at the NSRL with new approaches; however, few data have been reported at this time.

Because of the large number of radiation types and energies in space, a theoretical approach is needed to extrapolate limited data to other doses and particle types. There are also limitations as to how many particles can be studied in experiments due to both economical and time constraints. LET, which is a measure of energy loss, is known to provide a poor descriptor of track-structure and energy deposition in biomolecules, cells, or tissues. Biologically based methods are needed that are founded on fluence and track-structure rather than dose and LET, and that consider differences in biophysical events between HZE nuclei and γ-rays. Accurate QFs are not only important for improved risk calculations, but also to guide the design and evaluation of mitigation approaches such as radiation shielding and biological countermeasures. Shielding evaluations depend critically on the relative contributions of primary and secondary radiation[14,69] that depend on the definition of QFs. Other questions that have received little attention in the past are possible correlations between DDREF and Q-values, variations of RBEs for different types of cancer, and approaches to estimate the impact of qualitative differences between heavy ions and γ-rays. The role of differences in the types of initial biological damage, processing of damage, and subsequent signal transduction cascades in relation to aberrant tissue changes leading to tumorigenesis are also poorly understood.

5.1 Review of Radiobiology Data for Relative Biological Effectivenesses

5.1.1 Relative biological effectivenesses from human epidemiology studies

Human data for high-LET-induced carcinogenesis are extremely sparse. Limited insights are provided from analysis of the neutron contributions to the LSS data from Hiroshima and Nagasaki, or from radon daughter exposures to miners and medical patients exposed to α-emitters. Beyond statistical limitations in such data, there are important difference in the dose distribution among tissues and track-structure between the protons, helium and HZE nuclei in

space, and low-energy (<10-MeV) neutrons and α-particles in terrestrial high-LET exposures. The neutron contributions to the A-bomb survivors' data are usually treated with an RBE of 10; however, alternative approaches suggest higher dose-dependent values are plausible.[113,115] The BEIR VI report[110] made a thorough examination of α-particle risks of lung cancer. However, the local deposition of the dose in the lung from radon is quite different from the low-energy helium ions that are produced largely by high-energy GCR protons in all tissues, thus making any inferences from these data for space radiation risks quite difficult. ICRP Publication 92[31] noted that studies with α-emitters have estimated a low RBE compared to human studies for leukemia with γ-rays and x rays. Boice[126] estimates, from a study of 1003 patients exposed to thorostrast resulting in α-particle exposure to the bone marrow, an effectiveness of α-particles 1.33 times greater than that of γ-rays in the LSS of A-bomb survivors. In contrast, analysis of studies of liver cancer in thorostrast patients suggests RBEs of about 20 relative to the LSS results .[127] These estimates carry large uncertainties. For space radiation, the only epidemiology study reported was the increased risk of cataracts found at low doses (<100 mSv),[7,8] which suggests a large RBE (>10) for this endpoint.

5.1.2 Animal carcinogenesis studies with heavy ions

Animal studies generally demonstrate that HZE nuclei have higher carcinogenic effectiveness than low-LET radiation. However, the number of studies of animal carcinogenesis made with HZE nuclei is extremely limited, as summarized in **Table 5.1.** Dose response studies comparing tumor induction by γ-rays or electrons to HZE ions were measured for rat skin,[128,129] mouse Harderian gland,[130-132] rat mammary gland,[133] and mouse leukemia and liver.[134] These studies used one or only a few ion types, providing little information on the possible radiation quality dependence on RBE. The exception is the Harderian gland experiments, which consisted of seven ions of differing LET studied and exposures in a spread-out Bragg peak.[130] **Figure 5.1** shows that a similar dose response for solid tumor induction is observed for high-energy Fe nuclei in different murine models at low doses with an excess risk of approximately 25% at 0.2 Gy. Differences in cell sterilization effects or competing risks in the different models lead to different responses at higher doses. **No data have been reported for murine models of lung, colon, and several other tumor types important for human radiation risk assessments.**

Table 5.1. Tumor induction studies with HZE nuclei.

Tumor Model	*Tumor type*	*HZE type*	*Reference*
Mice (B6CF1)	Life-shortening	C, Ar, Fe	Ainsworth et al[135]
Mice (B6CF1)	Harderian Gland	He, C, Ar, Fe	Fry et al[130]
Mice (B6CF1)	Harderian Gland	p, He, Ne, Fe, Nb, La	Alpen et al[132,133]
Rat (Sprague-Dawley)	Skin tumors	Ne, Ar, Fe	Burns et al[136.137]
Rat (Sprague-Dawley)	Mammary tumors	Fe	Dicello et al[133]
Mice (CBA)	Leukemia, Liver	Fe	Weil et al[134]

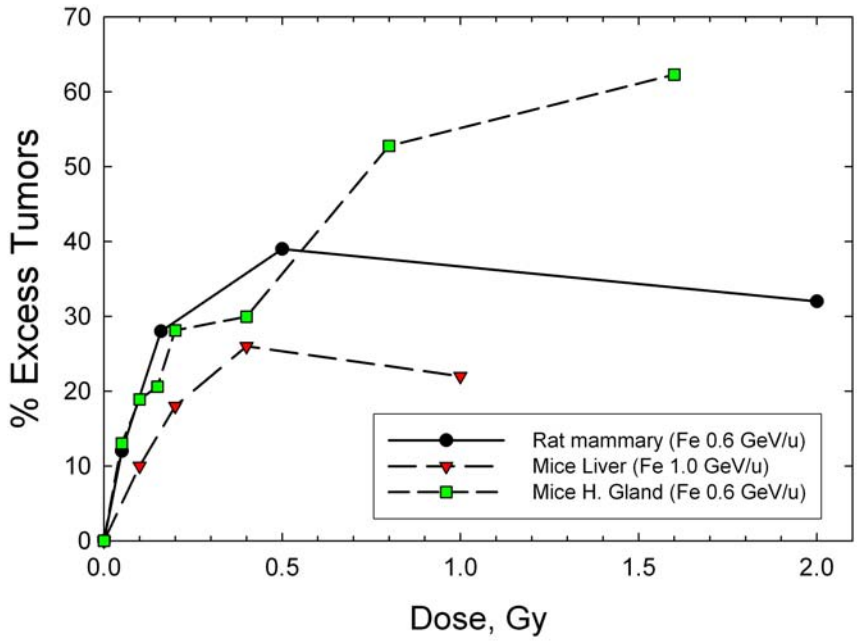

Figure 5.1. Excess tumors following iron irradiation for rat mammary[133] at 1.0 GeV/u, mouse HHarderian gland[131] at 0.6 GeV/u, and mouse liver at 1.0 GeV/u (LET=150 keV/μm).[134]

RBEs for Harderian gland tumors were estimated in the range from 20 to 40 for heavy ions at low doses.[130,131] An experiment was also performed to compare 6 weekly fractions of 0.07 Gy of Fe nuclei to an acute dose of 0.4 Gy; this experiment showed the fractionated exposure leads to about a 50% increase in tumor prevalence compared to acute exposure.[132] This suggests that even higher RBE values than estimated from acute dose response data are possible. RBEs for rat skin and mammary tumor induction by Fe nuclei are difficult to estimate because the low-LET radiation employed in these studies has zero initial slope. On one hand, an infinite RBE is estimated if the low-LET initial slope is taken as zero. On the other hand, a modest RBE value of about 10 is found if the higher dose points for the low-LET radiation are forced to intersect the zero dose point using a linear fit.

Weil et al[134] reported the RBE for Fe nuclei at 1 GeV/u for hepatocellular carcinoma (liver tumors) was 50.9 ± 9.9 in CBA [carcinoma-bearing animal] mice. In contrast, the RBE for AML for Fe nuclei was 0.48 ± 0.007. The small RBE found for Fe-induced leukemia is similar to the values for α-particles suggested by the thorostrast patient data and with neutron RBE studies of AML in mice that showed maximum RBEs of about 3.[138,139] In considering leukemia risks, the congruence of modest RBEs from human data, heavy ion, and neutron leukemogenesis studies along with studies of cell killing for progenitor cells for leukemias[140] or loss of deletions with time after exposure[141] lends support to a much lower QF assignment for leukemia compared to solid cancers.

RBE estimates for heavy-ion- and neutron-induced tumors are confounded by the bending of the response curves at modest doses. Alpen et al[131] arbitrarily ignored the higher-dose data to estimate an RBE using a non-weighted regression model. Edwards[142] used a weighted regression model to fit the same data sets while also ignoring the higher dose points in an attempt to avoid contributions from the downward curvature as the higher doses in the dose response.

Edwards[142] notes the problems with this approach in determining the initial slope for γ-rays as well as the heavy ions. Both Edwards[142] and Alpen et al[131] considered each ion individually in their fits to these data. Cucinotta and Chappell[24] applied functional forms motivated by TE or NTE models, which included a cell sterilization term, and made a global fit to all available data. In the NTE model, RBE estimates depend on dose below about 0.2 Gy. These RBE estimates are shown in **Figure 5.2**. Estimates for 600 MeV/u Fe nuclei range from about 25 in the TE model to as high as 80 in the NTE model at 0.05 Gy. The decline in RBE at high LET suggests a more negative power than p<-1/2, as embodied in the ICRP QF definition. Peak effectiveness was also near 200 keV/μm instead of 100 keV/μm as in the ICRP model. LETs in the range from between 30 and 180 keV/μm were not measured. The lack of data at these LET values likely influences estimates of which LET value would lead to the largest RBE. It is not known whether the 600 MeV/u Fe is the most effective GCR ion, but its carcinogenic power is similar to fission neutrons for this system. The La and Nb ions studied are high LET, but dissimilar Z from the GCR of interest. For other endpoints, fission neutrons are likely to have a higher effectiveness than neutrons of different HZE nuclei studied in the past. However for the Harderian gland study, tumor response for fission neutrons were dependent on pituitary implants in a manner similar to γ-rays,[143] while Fe nuclei showed a largely independent response to the pituitary implants.[131] A peak in the QF of 30 or higher for HZE nuclei is supported by the Harderian gland experiment, and an even higher value in the recent report on Fe-nuclei-induced liver tumors.[134] However, more information is needed, especially in the LET range from 50 to 250 keV/μm and at low doses, to prove or refute that a nonlinear dose response occurs.

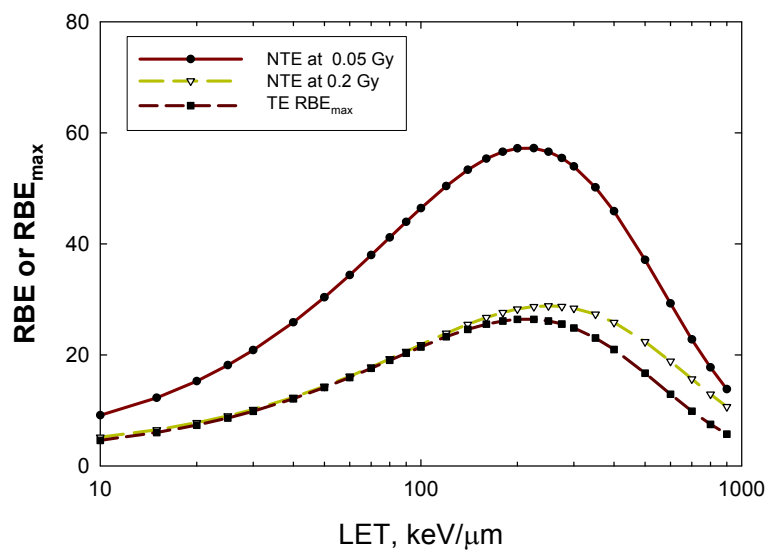

Figure 5.2. Calculations of RBE_{max} vs. LET in TE model, and the NTE model of RBE for doses of 0.05 or 0.2 Gy.

5.1.3 Cellular studies on chromosomal aberrations and mutation

For a large majority of biological endpoints, RBE peaks around 100 to 200 keV/μm, and then decreases at higher LET values. HZE nuclei are very effective at producing chromosomal exchanges with RBE values exceeding 30 in interphase (as visualized using premature chromosome condensation)[144] and 10 at the first post-irradiation mitosis for HZE nuclei.[145] **Table 5.2** shows RBE_{max} for chromosomal aberrations (CA) human lymphocytes estimates for several

energies of Si, Ti, and Fe nuclei. **Figure 5.3** compares Si and Fe data to data for neoplastic transformation of mouse C3H10T1/2 cells.[146] A sharp peak in the RBE curve appears at specific LET values similar to those of the ICRP model. However, through use of more energies in the CA study, the LET value in which the peak occurs is shown to increase with Z. Individual curves for each Z are not observed if LET is varied with limited E resolution. A lower RBE is found for the transformation experiments because the RBEs are based on 225-kVp x rays, not γ-rays, and are the RBEs at 50% cell survival levels, which are smaller than RBE_{max}.

Table 5.2. RBEs for chromosomal aberrations in human lymphocytes exposed to HZE nuclei at NSRL (George and Cucinotta, unpublished).[144]

Ion Type (E (MeV/u))	LET (keV/μm)	Z^{*2}/β^2	RBE_{max} for Total exchanges
Si (93)	158	1133	22.1±1.8
Si (170)	99	689	31.6 ±3.8
Si (250)	77	519	30.1± 2.4
Si (490)	55	344	18.5±1.6
Si (600)	48	311	11.8±1 .0
Ti (240)	195	1318	21.4±1.7
Ti (376)	152	984	23.0±1.8
Ti (988)	107	633	28.2±2.4
Fe (150)	440	2700	4.4±0.4
Fe (380)	220	1368	11.8±1.1
Fe (450)	197	1242	27.6±2.2
Fe (600)	178	1074	31.5±2.6
Fe (750)	170	976	29.9±2.4
Fe (1000)	151	881	28.0±2.1
Fe (5000)	145	693	23.3±1.9

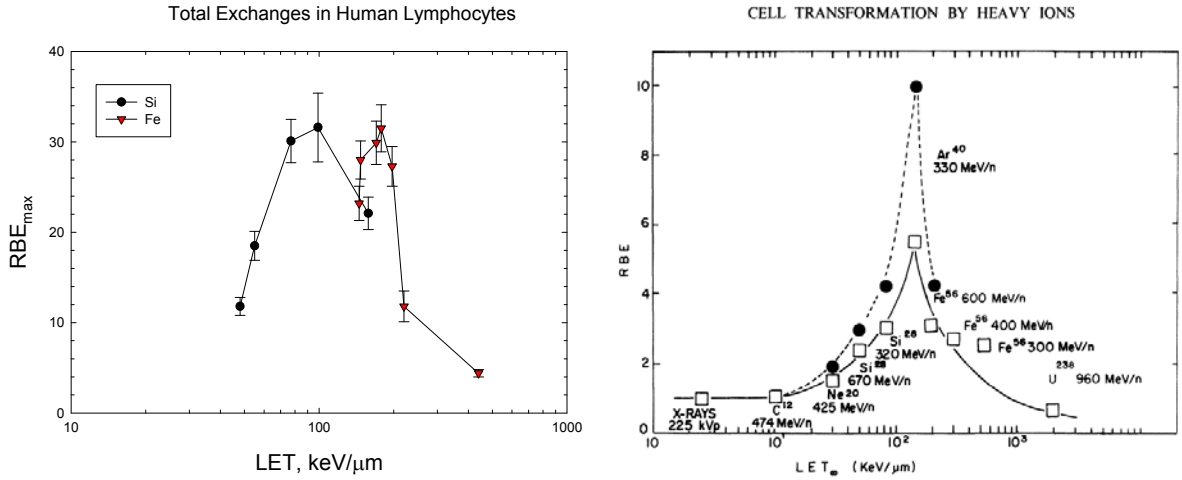

Figure 5.3. LET dependence of RBE. Left panel is RBE_{max} for chromosomal aberrations (total exchanges) in human lymphocyte cells for Si, Ti, and Fe nuclei relative to low-dose and dose-rate γ-rays.[144] Right panel is RBE at 50% survival relative to 225 kVp x rays for neoplastic transformation of C3H10T1/2 mouse fibroblast cells.[146] Solid circles are for delayed plating conditions, and open squares are for immediate plating.

The RBE vs. LET relationship found for total exchanges is similar to earlier studies of gene mutation.[147,148] For HPRT mutations, Kiefer found maximum RBEs of about 20 to 25 for He and

O nuclei compared to 300 MVp x rays where the lowest x-ray dose tested was 1 Gy.[148] Therefore, after considering possible differences in biological effectiveness between x rays and γ-rays for lower doses and dose-rates than those tested, RBE_{max} for HPRT mutations would likely exceed values of 30 for nuclei of the most effective Z and E. The CA and gene mutation data, as well as other data for cell inactivation, imply a higher-magnitude RBE peak at lower Z for fixed values of LET, which is consistent with the predictions of track-structure models. These data also suggest the slope, p, of the falloff with LET on the low-energy side of the RBE peak is more negative than in the ICRP Q. On the high-energy side of the peak, the RBE appears to decline in a manner underrepresented by LET. Here the LET is nearly constant at these energies as nuclei approach or exceed minimum ionization (~2 GeV/u). A single experimental campaign was made at the Brookhaven National Laboratory (BNL) alternating gradient synchtron (AGS) using ions of 5 GeV/u allowing for a comparison to results for Fe from NSRL or other facilities. George and Cucinotta[144] compared CAs for Fe at 0.6, 1, and 5 GeV/u with LE's of 178, 150, and 145 keV/μm. Results suggest the decline in RBE with increasing E was greater than a LET dependence would predict. In fact, the ICRP Q(LET) model estimates an increased effectiveness for Fe nuclei as the energy is increased above 600 MeV/u. Track structure models that take into account the broadening of a track as velocity is increased predict RBE declines as energy is increased above 600 MeV/u.[149]

The quality of chromosome damage or the mutation spectra has been noted to be different when heavy ions are compared to sparsely ionizing radiation.[147] Novel multicolor fluorescence painting techniques of human chromosomes have clearly demonstrated that α-particles and iron ions induce many more complex-type chromosomal exchanges in human cells than low-LET radiation.[150,151] Most of these complex chromosomal rearrangements will ultimately lead to cell death. In fact, only a small fraction of the initial damage is transmitted in mice 2 to 4 months after exposure to energetic Fe ions. A low RBE for induction of late chromosomal damage was observed in the progeny of human lymphocytes exposed in vitro to energetic Fe ions, with the interesting exception of terminal deletions; this occurred with much higher frequency with heavy ions compared to γ-rays, leading to a very large RBE value.[152]

5.1.4 Delayed effects from in-vivo and in-vitro studies

Genomic instability in the form of delayed chromosomal aberrations or micronuclei has been measured in mice or rats by several groups,[153-156] two-dimensional cell culture models,[157] and more recently three-dimensional cell culture models have also been studied for genomic instability.[158] These studies are typically undertaken to understand mechanisms and verify effects, and are often limited by the number of radiation qualities and doses studied. The relationship between delayed micronuclei appearance or chromosomal aberrations and cancer risk is also poorly understood. In general, high-LET radiation is more effective in producing chromosomal instability and delayed micronuclei than low-LET radiation, and in some cases no effect is observed for low-LET radiation. However, RBE or dose-response curves have not been studied in any detail for these endpoints.

5.1.5 Dose-rate and protraction effects for high-energy and charge nuclei

For proton and HZE nuclei exposures at a low dose-rate of more than a few months, new biological factors may influence risk assessments, including redistribution in the cell cycle, repopulation, or promotional effects, especially when particle fluences are large enough to lead to multiple hits of target cells or surrounding cells and tissue. Very few experimental data are at

low dose-rates for HZE nuclei. Burns et al[136] found split doses of Ar ions separated by from a few hours up to 1 day increased the risk of skin cancer in rats. Alpen et al[132] found using seven 2-week fractions of 0.07 Gy of iron increased risk to 50% compared to a single acute dose of 0.4 Gy for harderian gland tumors in mice. The Skyhook study of Ainsworth[135] considered life shortening in mice, comparing single acute with weekly fractions of several ions; however, the results were unclear with regard to any increase or decrease in risk as dose-rate is decreased. For γ-rays and neutrons, a number of studies for cancer induction or life shortening in mice were made, showing that the sparring effects for γ-rays and neutron effects may be increased due to protraction under certain conditions in some tissues.[159,160] Important questions related to the differences in life span, cell turnover rates, the role of cell killing, and mechanisms of initiation or promotion in humans and mice make difficult the estimates of the effects of protraction on risk. Elucidating possible differences in inflammation and immune responses at high vs. low or chronic doses is also needed to improve risk estimates. If protraction effects do increase the risk from high-LET radiation, such effects would be more important for a Mars mission than for the shorter lunar missions.

An additional radiation quality uncertainty is caused by the scaling assumption used when applying ERR and EAR functions from low-LET studies. Here time-dependent factors such as time to tumor appearance are assumed to be independent of radiation quality. Data on tumors or genomic instability in mice with neutrons[155,159,160] and the studies of rat or mammary carcinogenesis with HZE nuclei[133,136] suggest that the latency time is reduced for high-LET radiation compared to low-LET radiation. Few data are available to estimate the impact of these differences on risk estimates; however, those that do exist suggest RBEs are likely to depend on time after exposure. The so-called initiation-promotion models of cancer risk suggest that ERRs will decline with time after exposure[16] and RBEs that depend on time after exposure are predicted from these models.[161]

5.2 Biophysical Considerations

The term “track-structure” refers to the description of the position of excitations and ionization of target molecules from the passage of ions through DNA, cells, or tissues. It is these initial insults from particles interacting with biomolecules that lead to all biological damage from radiation. Two types of initial damage are considered: (1) DNA damage through direct ionization or oxidative radicals, and (2) oxidative damage to non-DNA structures (water molecules, proteins, etc.) leading to changes in signaling or tissue status and function. Track structure descriptions are used in theoretical models of biological responses to understand and extrapolate limited radiobiology data to other radiation qualities and doses.[162] Monte-Carlo track-structure simulation codes have been used to study the distribution and types of initial DNA damage, including models of single-strand breaks (SSBs) and DSBs, base damage and clusters of different types of DNA damage[163] and in the description of the oxidative damage.[164]

Ionization and excitation processes caused by the track of the ion and the electrons liberated by an ion lead to a stochastic cascade of biological events. Originating from the primary track are the energetic secondary electrons, denoted as δ-rays, which can traverse many cell layers from the track. **Figure 5.4** illustrates the stochastic nature of the energy deposition, showing a Monte-Carlo simulation of the radioloytic species produced by ions with an identical LET of 150 keV/μm but a differing charge number.[164] The ICRP and NCRP approach to describe radiation quality assumes that the ions shown in **Figure 5.4** produce the same cancer risk, although the initial physical-chemical stages are quite distinct.

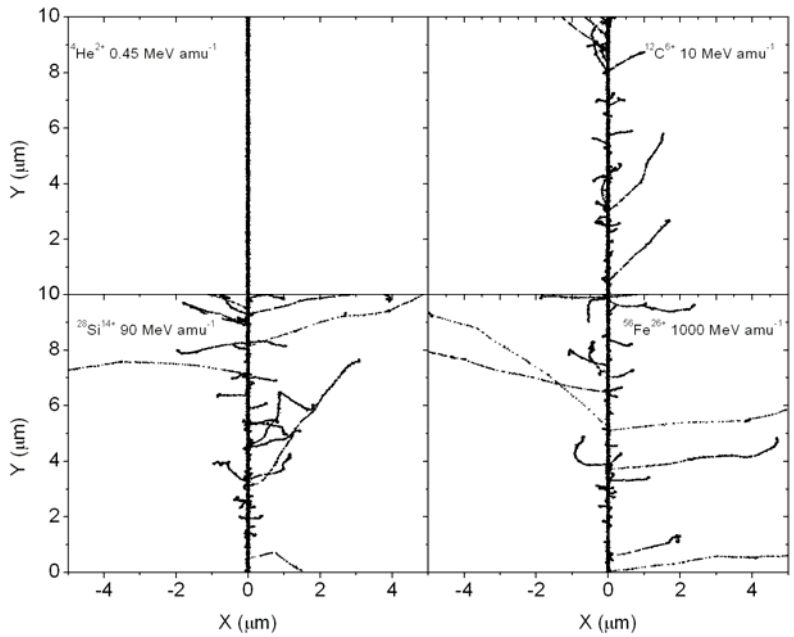

Figure 5.4. Projections over the XY plane of simulated tracks segments (calculated at ~10^{-12} s) for the following impact ions: ^{4}He (0.45 MeV/u), ^{12}C (10 MeV/u), ^{28}Si (90 MeV/u), and ^{56}Fe (1 GeV/u). Ions are generated at the origin along the Y axis in liquid water at 25°C under identical LET conditions (~150 keV μm^{-1}). Each dot represents a radioloytic species.[164]

Because of the complexity of particle tracks and biological systems and their response to radiation, a simplification scheme is always used to describe biological effects of radiation. The most commonly used approach is to introduce the concept of energy deposition as an empirical description of atomic collisions and ionization and excitation reactions by a given number of radiation tracks (or fluence). Several biophysical models describe how energy deposition changes with particle charge and energy at the molecular and cellular level. However, the simplest approach is to assume that energy loss by particles (or LET) is approximately the same as the empirical quantity, energy deposited in the volume of interest.

Values of LET are normally evaluated using the Bethe-Bloch formula or similar expression.[33] LET can also be calculated in terms of the radial distribution of dose as a function of impact parameter; denoted as the radial distance, t, about the track of the ion. The radial dose is the energy density distribution in a cylindrical shell of radius, t, about the path of the ion.[165] Integration of the radial dose distribution over all values of t up to the maximum allowable value, t_M, is a measure of the LET:

$$LET = 2\pi \int_0^{t_M} t\,dt\,[D_\delta(t) + D_{exc}(t)] \tag{5.1}$$

In Eq(5.1) contributions to the radial dose from ionization are denoted as D_δ, and excitations by D_{exc}. The value of t_M, which defines the track width, is a function of particle velocity that corresponds to the range of electrons with maximum energy ejected by the passing particle. At suffi-

ciently low energies (<0.1 MeV/u), nuclear stopping also contributes to the LET. At very high energy and charge number two-photon emission processes contribute to the LET.[166] The track width can extend well beyond 100 μm as the velocity of the ions approaches the speed of light. The primary electron spectrum from ion interactions with target atoms is folded with average transmission properties of electrons to obtain the spatial distribution of electron dose as a function of radial distance from the path of the ion (Kobetich and Katz, 1968):[167]

$$D_\delta(t) \quad = \quad -\frac{1}{2\pi t}\sum_i \int d\Omega \int d\omega \frac{\partial}{\partial t}[E(t,\omega)\eta(t,\omega)]\frac{dn_i}{d\omega d\Omega} \tag{5.2}$$

In Eq(5.2) ω is the initial electron energy, E is the residual energy of an electron with energy ω after traveling distance t, and $\eta(t,\omega)$ is the transmission probability that an electron with starting energy, ω, penetrates a depth, t. Equation (5.2) includes an angular distribution for the number of primary electrons produced from target atom i, n_i, with energy, ω, and solid angle, Ω. The cross sections for electron production from protons are typically scaled to heavy ions using the effective charge number, Z^*, which includes a velocity-dependent screening correction at low energies. The accuracy of the angular distribution is found to substantially modify the radial distribution both at large and small radial distances, and to play only a minor role at intermediate values where a $1/t^2$ behavior holds.

An *ansatz*[168] can be used for the radial dependence of the excitation term, $D_{exc}(t)$, which is important at small values of t (<10 nm),

$$D_{exc}(t) \quad = \quad C_{exc}(A,Z,\beta)\frac{\exp(-t/2d)}{t^2} \tag{5.3}$$

where $d=\beta/2\ hc/(2\pi\omega_r)$, c is the speed of light, β is the ion velocity scaled by c, h is Plank's constant, $\omega_r = 13$ eV for water, and C_{exc}, is a normalization parameter. In Eq(5.3), the radial extension of excitations is confined to very small distances (<10 nm) as characterized by the parameter d.[168] Characteristics of the two components of the radial dose are illustrated in **Figure 5.5** for nuclei of LET close to 30 keV/μm (1 MeV protons and 300 MeV/u Ne).[169] The radial dose for Ne extends for many microns, while low-energy protons deposit all of their energy within 0.1 micron of the track. The model of Chatterjee et al[170] incorrectly assumes that energy deposition in so-called track core and penumbra make equal contributions (50% each), while in truth less than 20% of energy deposition is in the so-called "core" (see reviews by Kraft et al;[171] Cucinotta et al[169]).

The frequency distribution of energy imparted to a volume of biomolecular dimensions[163] is more closely related to stochastic aspects of radiation tracks described by Monte-Carlo methods than it is to the radial dose. For high-energy ions, frequency distribution can be described using the impact parameter of the ion and distinguishing events in which the ion passes through a volume (primary-ion or δ-ray events) and outside a volume (δ-ray events).[172] The two components can be weighted by considering the number of events as a function of impact parameter. The frequency distributions demonstrate energy deposition events in biomolecular targets that occur for high-LET radiation that are not possible with low-LET radiation, even at high doses (up to 100 Gy of low-LET radiation).[163] These higher-energy deposition events are usually confined to close to the track of the ion, often called the "track core," and events similar to low-LET radiation at larger distances, often called the "track penumbra." The distinction is somewhat arbitrary

because deposition will vary with dimension considered, and because δ-rays dominate energy deposition in both regions.

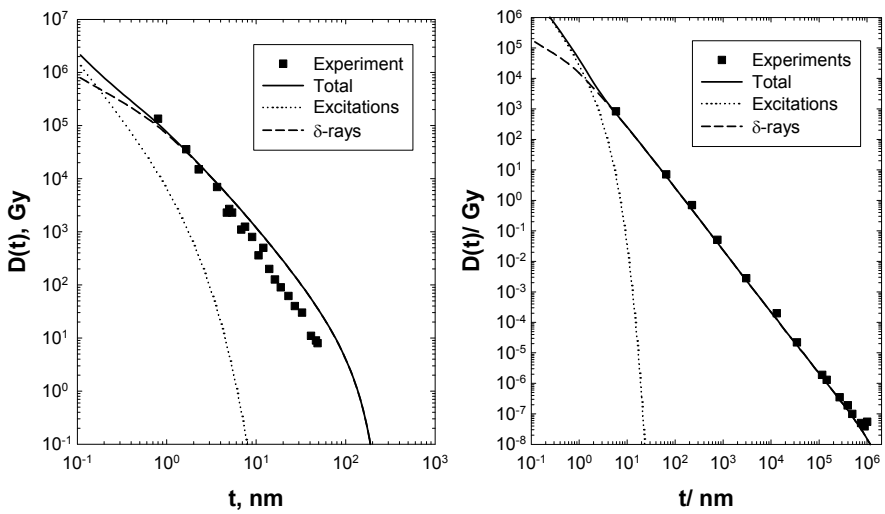

Figure 5.5. Calculations of radial dose distributions to experiments for ^{1}H at 1 MeV (LET=27 keV/μm) (left panel) and ^{20}Ne at 377 MeV/u (LET= 31 keV/μm) (right panel).[169]

Goodhead et al[173] reviewed energy deposition models and noted that using the probability of producing >9 ionizations in small volumes (<5 nm diameter), corresponding to a short segment of DNA, provided in the experiments of that time the best description of increased biological effectiveness at high LET. This number of ionizations is related to energy deposition >300 eV in this volume. Microdosimetry approaches, which use micron-size volumes, were shown to be inadequate for describing heavy ion effects or the effects of ultra-soft x rays. Ultra-soft x rays produce only low-energy electrons with short ranges (typically <20 nm), and are a useful probe of mechanisms or radiation action. Ultra-soft x rays were used in several defining experiments to demonstrate failed arguments in microdosimetry-based models. These arguments extend to the use of microdosimetry models of radiation quality, which are often motivated by detector considerations rather than radiobiology and are often difficult to interpret due to artifacts such as wall composition, anode wires, and electronic noise inherent in the measurement.

The spatial distribution of δ-rays plays an important role in describing RBE. Observations by Goodhead et al[173] and earlier arguments from Katz[174], predict that biological effects would be highly influenced by δ-ray effects rather than by LET alone. **Figure 5.6** shows such a description comparing the frequency of energy deposition above 300 eV in a volume the size of the nucleosome. The comparisons illustrate that the parameter Z^{*2}/β^2 provides an improved descriptor of energy deposition in small volumes compared to LET. Deviations from a unique Z^{*2}/β^2 dependence occur at low energy where the curves branch for distinct charge numbers. For identical LET values, the ion with the lowest charge is predicted to be more effective at energies above a few MeV/u.

Research at the NSRL is making new estimates of radiation quality effects for a variety of endpoints with the focus on approaches to mechanistic understanding of biological effectiveness. However, very few comprehensive studies have been completed at this time. Here we note that in the past very detailed studies of radiation quality were made for DNA breaks, as well as for cell

inactivation and mutation for a large number of ion types. Such extensive studies would be difficult to repeat today because of the higher costs of many current experimental approaches,

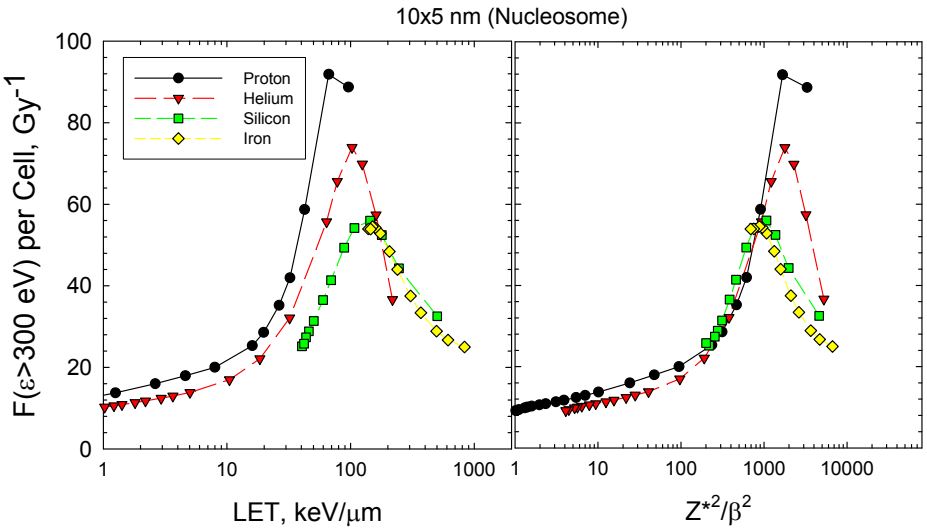

Figure 5.6. Number of nucleosomes per cell receiving 300 eV or more as a function of LET (left panel) or Z^{*2}/β^2 (right panel). Calculations are shown for H, He, Si, and Fe nuclei using methods of Cucinotta et al.[172]

and certainly would take many years to complete. These older studies are useful to consider in terms of track-structure models. **Figure 5.7**, from Thacker et al,[175] illustrates such track-structure effects for cell inactivation with several ions at a variety of LET values. The upper panel shows the RBE diverging for ions with similar LET values but differing charge numbers, while the lower panel shows much improved convergence when radiation quality is described by the parameter Z^{*2}/β^2. Similar observations by Belli et al[176,177] suggested that protons were significantly more damaging than helium at the same LET for V79 cell inactivation and HPRT mutation. More expansive studies of diverging biological effectiveness for particles of identical LET, but differential *Z* and *E*, were made with heavy ions with energies from about 1 to 20 MeV/u. **Figure 5.8** shows results expressed as an action cross section for inactivation of *E. coli* Bs-1,[178] *Bacillus subtilus* (rec),[179] and V79 mammalian cells.[148,175,180] These experiments were compared to the Katz track-structure model by Cucinotta et al,[149,181] which is also shown in **Figure 5.8**. Good agreement is found in comparing the model to experiments. LET is a poor predictor of biological effectiveness in these comparisons, which was established by the use of many ion types and energies. Track structure models of DNA damage endpoints show similar deviation of LET response for nuclei with different *Z*. **Figure 5.9** shows predictions from Holley and Chatterjee[182] for the production of small DNA fragments (0.02 to 20 kbp [kilobase pairs]) by several HZE nuclei. The model shows that for two nuclei with the same LET, the one with the lower *Z* has a larger biological effectiveness. It is also known that the production of the initial oxidative species varies by *Z* and *E*, and not by LET alone as shown in **Figure 5.9** (right panel).

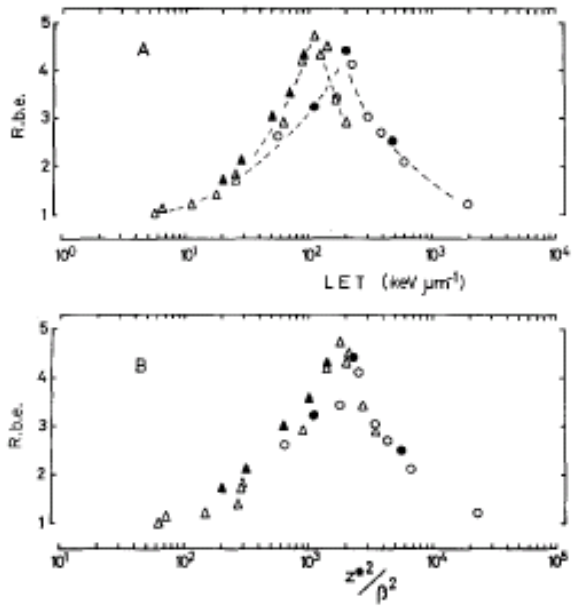

Figure 5.7. Reproduced from Thacker et al,[175] the relationship between RBE and ionization density for V79 hamster cells (closed symbols) and T1 human cells (open symbols). Panel A: RBE vs. LET. Panel B: RBE vs. Z^{*2}/β^2.

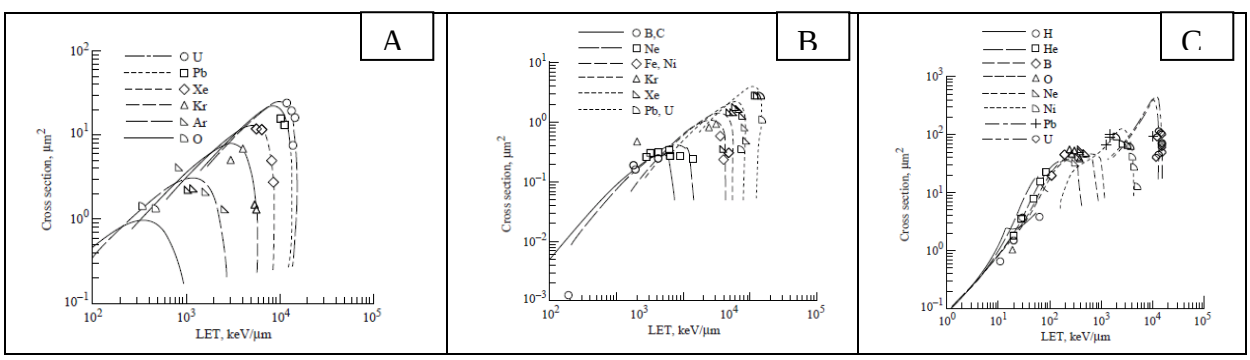

Figure 5.8. Cross sections for inactivation of *E. coli* (panel A), Bacterial spores (panel B), and V79 mammalian cells (panel C) showing charge number branching in the LET dependence of biological responses (see Cucinotta et al[181] for details).

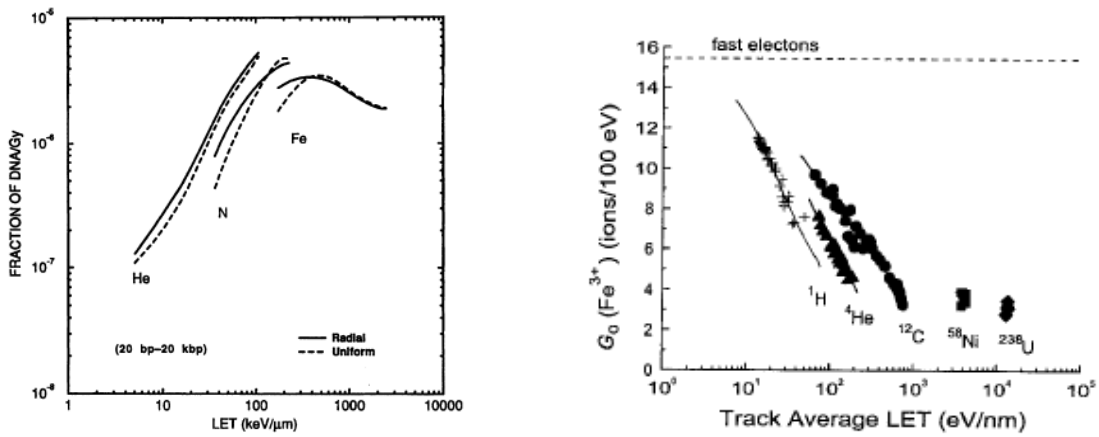

Figure 5.9. Panel A shows calculations of total yields of fragments of double-stranded DNA with sizes from 0.02 to 20 kbp for He, N, and Fe nuclei (for details see Holley and Chatterjee[182]) showing that lower Z nuclei have greater biological effectiveness at identical LET values than higher Z nuclei. Panel B shows results for Laverne[183] of ferric ion yields in the Fricke dosimetry illustrating charge branching with LET for oxidative damage effects.

The existing evidence therefore suggests that the radiation quality dependence of both the initial DNA damage and the non-DNA damage, such as the production of various oxidative species, is dependent on Z and LET or alternatively Z and E, and is not well described by LET alone.

Although commonly used endpoints (eg, DNA breaks, cell death, mutation, and chromosomal aberrations used to investigate track-structure effects) are limited as surrogate markers to cancer risks, they are used under the assumption that cancer risks would follow similar relative changes as a function of radiation quality. HPRT mutations are clearly related to the deletion of segments of DNA in surviving cells; but the role of mutations and genomic instability that might evolve from deletions in cancer risk is still debated. While chromosomal aberrations are found in almost all human tumors, they can be both an initiating event or the result of genomic instability from an independent event. The NRC[1] recommends that endpoints, such as chromosomal aberrations or cell inactivation, could be studied to evaluate track-structure and shielding effectiveness. However, it would be more useful for track-structure studies to be made with endpoints clearly related to cancer risk.

5.3 Biophysical Models of Relative Biological Effectiveness

Heavy ion and neutron dose response curves for tumor induction often appear to increase linearly at low doses and then bend over at moderate doses of 0.5 Gy or lower due to cell sterilization effects or competing risks.[160] This bending in the dose response makes determination of RBE_{max} values difficult unless large sample sizes for multiple low doses are used. For describing tumor dose-response data in which cell killing or competing risks modifies the dose response at higher doses, a commonly used functional form, which we denote as the TE model, is given by:

$$P_{TE} = P_0 + [\alpha(L)D + \beta(L)D^2]e^{-\lambda(L)D} \tag{5.4}$$

where the dose is denoted, D, and P_0 is the background tumor probability. The α, β, and λ coefficients are parameters that will depend on radiation quality. The dose-squared term (with

coefficient β) in Eq(5.4) is normally only considered for γ-rays or other forms of low-LET radiation such as high-energy protons or helium ions. Equation (5.4) can be thought of as a Taylor series expansion with higher-order terms typically ignored.

It is a common assumption to represent radiation quality dependence in terms of LET with the α or linear induction term rising with increasing LET to a peak and then decreasing at higher LET:

$$\alpha(L) = \alpha_0 + \alpha_1 L \exp(-\alpha_2 L) \tag{5.5}$$

And, similarly for the cell sterilization factor:

$$\lambda(L) = \lambda_0 + \lambda_1 L \exp(-\lambda_2 L) \tag{5.6}$$

The D_o value for cell killing, which varies by LET, is given by $1/\lambda(L)$.

In the TE model, the RBE becomes independent of dose at a sufficiently low dose in which the cell sterilization term and the β-term can be ignored. RBE_{max} is defined as a low dose-limit given by the ratio of linear-induction coefficients for γ-rays and ions:

$$RBE_{TE} = \frac{\alpha_L}{\alpha_\gamma} \tag{5.7}$$

At low fluence, where less than one particle intersects the biological target under study, the biological action cross section, which is defined as the probability per unit fluence for the end-point considered (eg, cell inactivation, mutation, or tumor induction), is a very useful quantity for discussing particle effects. This concept holds rigorously when exponential or linear dose response curves occur such that the simple relationship applies:

$$\alpha D = \sigma F \tag{5.8}$$

Using a conversion factor to have units of μm^2 for σ, keV/μm for LET, and Gy for dose leads to:

$$\sigma = \alpha L / 6.24 \tag{5.9}$$

The RBE is expressed in terms of the linear slope for γ-rays and the action cross section as:

$$RBE = \frac{6.24\sigma}{\alpha_\gamma L} \tag{5.10}$$

A complication occurs if the dose response curve for particles contains nonlinear terms. The initial slope in a dose response curve will then be distinct from the final slope or a slope estimated at higher doses. In this case, models of nonlinear terms must be constructed to infer the action cross section from dose response data.[162] The use of fluence is problematic for γ-rays, because of the complication of the distribution of electrons of varying LET that mediate γ-ray effects, and because a “low electron fluence” regime is difficult to observe experimentally for biological endpoints of interest (eg, doses of ~0.01 Gy or less).

Because of the large number of particle types and energies in space, parametric representations will be quite limited if no underlying biophysical model is used to describe track-structure and dose response curves. Instead, a parametric approach built on an underlying track-structure model would be very useful for extrapolation of experimental data. Biophysical models can describe how RBEs vary with radiation quality, and can be compared to the assumption of the QF function dependence on LET alone. One consideration is the assumed decline in effectiveness at high LET by the power, p=-1/2, in the ICRP definition of Q(L). Katz and Cucinotta[184] studied the case in which a multi-target model represents the γ-ray biological response data. In the Katz model,[162] the action cross section is calculated in terms of the radial dose distribution averaged over the target volume $\overline{D}(t)$, and γ-ray dose response function, P(D), integrating over all distances from the ions track to the target as:

$$\sigma = 2\pi \int t dt P(\overline{D}(t)) \tag{5.11a}$$

For ions above about 5 MeV/u with Z<30, the cross section model of Katz et al[162] is accurately described by the function:

$$\sigma = \sigma_0 (1 - e^{-Z^{*2}/\kappa\beta^2})^m \tag{5.11b}$$

where *m* can be interpreted to represent a target number or hit number, σ_0 is the saturation area of the sensitive part of biological system under consideration, and κ is a measure of the value of Z^{*2}/β^2 where σ approaches σ_0. These constants are fitted to radiobiological data sets. Equation (5.11) predicts the action cross section above energies of about 5 MeV/u for Z<30, which then increases with Z^{*2}/β^2 until reaching a maximum dependent on the value of κ. If an ion has a charge and speed such that $Z^{*2}/\beta^2 > \kappa$, saturation occurs. Values of κ ranging from 500 to 2000 were found in fits to a large number of radiobiology experiments with heavy ions.[185] The action cross section deviates from this form at lower E where thin-down occurs (narrowing of the track relative to the biological target size) or for very high Z where $\sigma > \sigma_0$. At low fluence, the RBE is found to follow the following relationship (Katz and Cucinotta, 1991):[184]

$$RBE = \frac{\sigma^{1/m} D_{0\gamma}}{F^{1-1/m} L} \tag{5.12}$$

where $D_{0\gamma}$ is a radiosensitivity parameter for the γ-ray data being considered. Equation (5.12) predicts that the RBE declines once the cross section saturates to its asymptotic value, σ_0, as higher LET values are reached with a power, p=-1. Katz has also described a “final slope” cross section for high doses that shows a distinct dependence on Z^{*2}/β^2 and LET rather than Eq(5.12). At high dose, LET is shown to be a reasonable predictor of radiation quality effects, as should be expected because here δ-rays from many overlapping particle tracks occur.

Of the biophysical models developed to describe heavy ion effects, the Katz model provides the most robust description of heavy ion dose responses and radiation quality. Mechanistically, the model contains several deficiencies,[169,186] including neglect of stochastic aspects of radiation tracks and ignoring differences in biological effectiveness of electrons of different energies. In many applications, the multi-target model is also used, which ignores a linear response term for γ-rays and a time-dependent description of damage repair. The idea of an effective target size continues to be debated in radiobiology.[187] There appear to be several important dimensions.

These are target sizes on the order of: (1) small segments of DNA (<10 nm) leading to DNA breaks including complex DSB, gene mutation, and also leading to chromosomal aberrations through a one-hit mechanism involving DNA mis-repair; (2) a micron related to the interaction between DSBs as a second mechanism for chromosomal aberrations; and (3) one to a few cells related to distributed oxidative damage leading to signal transduction processes and perhaps to NTE. The Katz model, which did not assume any specific ideas on target size, allowed fits to radiobiology data to determine characteristic size – perhaps one of the reasons for its parametric efficiency.

A linear kinetics repair/mis-repair model[188,189] that uses the Katz model track-structure model, but allows for a linear term in the γ-ray dose response that leads to an RBE model at low fluence given by:

$$RBE_{\max} \quad = \quad (1-\sigma/\sigma_0) + k_{mis}\frac{\sigma D_{0\gamma}}{L} \tag{5.13}$$

where k_{mis} is a constant representing the fraction of initial damage that is mis-repaired. The inclusion of the linear term for γ-rays does not reduce the accuracy of fits of the cross section as long as a multi-hit or multi-targeted term is dominant. This result predicts the same characteristic of declining RBE at high LET or Z^{*2}/β^2 as Eq(5.12), which is due to saturation; however, it differs by reaching a maximum RBE at sufficiently low fluence, which is not true for Eq(5.12) when m>1. The RBE is predicted to decline like p=-1 at high ionization density. We note biophysical models and radiobiology experiments suggest that for identical LET values, the ion with the lowest charge will have the highest RBE as predicted by Eq(5.12) or Eq(5.13), at least for velocities above where the track is wider than the characteristic size of the biological target. Whether stochastic track-structure models would alter these observations has not been studied in sufficient detail. In contrast, the ICRP model assumes p=-1/2, and the ICRP report states that ions with larger Z would have the higher RBE for a fixed value of LET.[31]

5.3.1 Relative biological effectiveness in the non-targeted effects model

We next consider an alternative to the linear dose response assumed by the TE model. A model that considers deviations from linearity at low doses is motivated by studies of NTE. Non-targeted effects, including bystander effects and genomic instability in the progeny of irradiated cells, have been shown to lead to nonlinear dose responses at a low dose (<0.1 Gy). Evidence for NTE effects are more extensive for high-LET than for low-LET radiation; however, this has largely been observed in cell culture models. More recently, the harderian gland tumor study with heavy ions was found to be better described by an NTE model as compared to a TE model.[24] The BEIR VII[16] and UNSCEAR[17] reports reviewed recent scientific literature on NTE for low-LET radiation. Other research suggests that for high-LET radiation at low doses, NTE are clearly important and lead to nonlinear responses. **Figure 5.10** illustrates[2] the potential importance of NTE to NASA. NTEs would lead to different expectations for mission length, radiation shielding, and mechanisms of risk compared to TEs; therefore, understanding their role in risk assessment is of major importance to NASA.

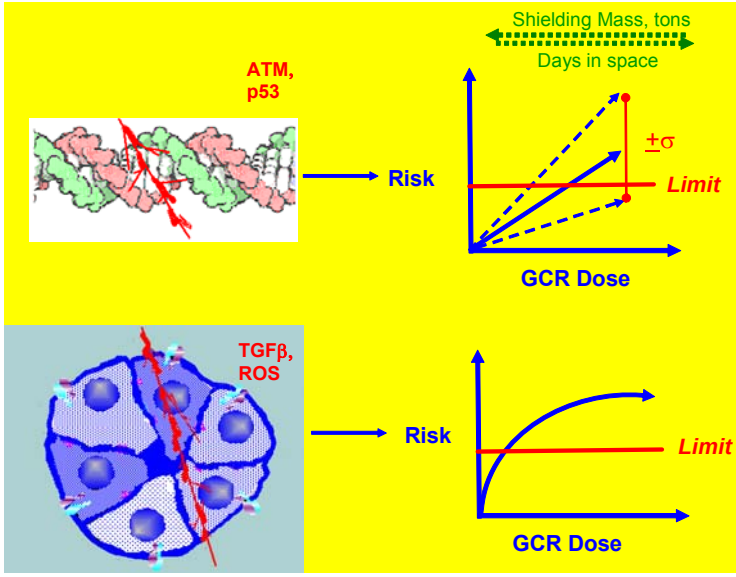

Figure 5.10. Schematic of importance of uncovering basic mechanisms of cancer induction by space radiation.[2] Determining the role of DNA damage vs. non-targeted effects has large implications for radiation shielding and mission duration, and in approaches to the design of biological countermeasures. In a DNA model, a linear response is expected with research focus on slope of response as function of radiation quality and radiation sensitivity. In the non-targeted model, shielding is ineffective and distinct targets for biological countermeasures are pursued.

Many bystander experiments have focused on establishing effects and possible mechanisms using cell culture models such as medium transfer from irradiated cells to un-irradiated cells.[190,191] A second approach is the use of low-energy H and He microbeams of relatively high LET that target a fixed number of cell traversals of hit cells with concurrent identification of non-hit cells that receive bystander signals.[192] These experiments are not able to provide data on the shape of the dose response curve at low doses. Other experiments have used low doses of α-particles of high LET (90 to 120 keV/μm) in which the average fraction of cell hits can be estimated based on the cell area. Data for sister chromatid exchanges,[193,194] chromosomal aberrations,[195] and neoplastic transformation[196,197] suggest that dose responses for high-LET radiation deviate from linearity at low doses, which is defined as less than one track per cell nuclei in which a flat or shallow dose response is observed. These experiments, under broad-beam irradiation conditions, mimic conditions for exposures of interest for radiation protection on Earth or in space travel.

The functional form of an NTE model includes a constant (dose-independent) term above a certain dose threshold. It can be assumed that the NTE term saturates as LET is increased for the radiation quality dependence of the NTE term. The NTE dose response model is written:

$$P_{NTE} \quad = \quad P_0 + [\alpha(L)D + \beta(L)D^2]e^{-\lambda(L)D} + \kappa(L)e^{-\lambda(L)D}\Theta(D_{th}) \qquad (5.14)$$

In the model, NTE are reduced as the dose is increased and all cells are hit. Because high-energy ions deposit energy through δ-rays in many cells adjacent to cells directly traversed by a particle, Cucinotta and Chappell[24] reasoned that it was more useful to reduce the NTE term by the cell survival probability as dose is increased rather than by the probability of cell traversal by

ions. The different choices should have only a minor effect since the TE term in Eq(5.14) is expected to dominate at higher doses.

The dependence of NTE on LET can be described by a term that increases linearly with LET with an exponentially decreasing modifying factor at high LET as given by:

$$\kappa(L) \quad = \quad \kappa_1 L \exp(-\kappa_2 L) \tag{5.15}$$

where the parameter κ_1 represents the strength of the non-targeted effect, κ_2 is a saturation of NTE at high LET, and the step function Θ represents a likely threshold dose for the NTE, which is ignored in the data analysis and arbitrarily set at 0.01 Gy as it is assumed to occur at a dose lower than the experiments considered. The addition of the nonlinear induction term motivated by the NTE model was found by Cucinotta and Chappell[24] to provide an improved fit compared to the TE model to the Harderian gland tumor data of Alpen et al.[131] These results are modified here to consider the additional data for lanthanum nuclei from Alpen et al.[132] Results in **Table 5.3** include statistical tests of quality of fit with the NTE fits providing an improved fit compare to the TE model for each test considered.

Table 5.3. Parameters that result from global fits to all ions for Harderian gland tumor dose-response data in the TE and NTE models as described. Also shown are test statistics for the goodness of fits of the models, including the Bayesian information criteria (BIC), Akaiki information criteria (AIC), and adjusted R^2 test. Each test resulted in the NTE model providing an improved fit compared to the TE model.

Parameter	*TE Model*	*NTE Model*
P_0	2.93±0.47	2.54±0.4
α_0 , Gy^{-1}	7.53±3.96	10.02±2.07
α_1, Gy^{-1} $(keV/\mu m)^{-1}$	1.261±0.213	0.679±0.187
α_2 , Gy^{-1} $(keV/\mu m)^{-1}$	0.0037±0.00058	0.0033±.0006
β, Gy^{-2}	6.3±3.41	5.08±3.0
λ_0, Gy^{-1}	0.25±0.065	0.231±0.016
λ_1, Gy^{-1} $(keV/\mu m)^{-1}$	0.0051±0.0029	0.0033±0.0042
λ_2, Gy^{-1} $(keV/\mu m)^{-1}$	0.0034±0.0027	0.005±0.0064
κ_1, $(keV/\mu m)^{-1}$	-	0.12±0.06
κ_2, $(keV/\mu m)^{-1}$	-	0.0053±0.002
Adjusted R^2	0.933	0.954
AIC	208.52	193.6
BIC	222.42	209.24

The diameter of the epithelial cell nucleus transformed in mouse Harderian gland tumors is about 5.5 μm with a cell nucleus area, *A*, of about 24 μm^2. Using the relationship between dose, *D* (in units of Gy), and fluence, *F* (in units of μm^2), as *D = F x L / 6.24,* the number of ion hits per Gy per cell nucleus, *H*, is given by:

$$H \quad = \quad \frac{6.24DA}{L} \tag{5.16}$$

Figure 5.11 shows the model fit to the Harderian gland experiment. The comparison shows that less than 1 Fe ion per 100 cells, which is more than double the tumor prevalence. The response curves for the heavy ions display a characteristic change in slope from a low-fluence region, in which NTE effects dominate, to intermediate regions, in which TE dominate and then bend and decrease as cell sterilization contributes at even higher fluence.

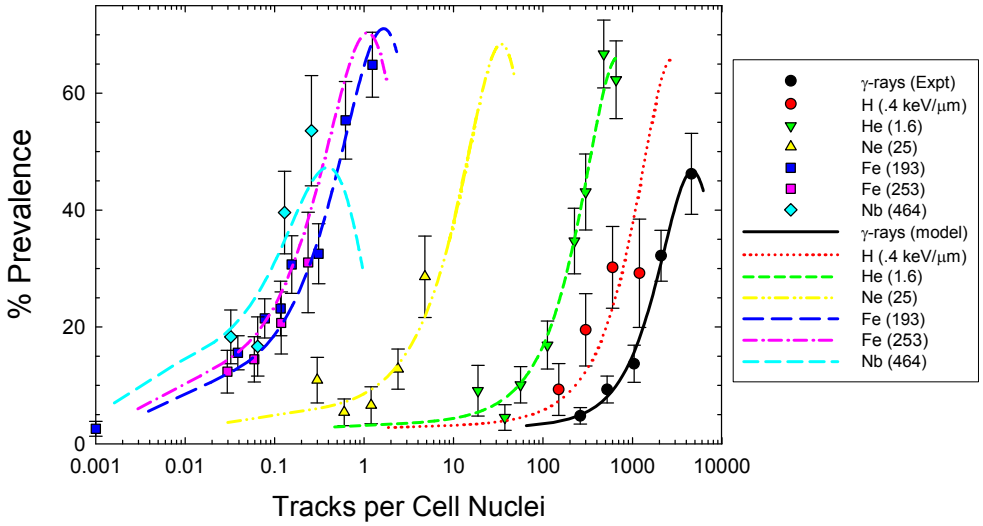

Figure 5.11. Comparison of NTE2 model[24] to experiments[131] for prevalence of harderian gland tumors vs. the number of radiation tracks per cell nuclei (diameter of 5.5 μm). Error bars represent standard errors. A mean LET of 0.23 keV/μm is used to convert dose to number of radiation tracks for γ-rays.

The RBE can be estimated near the crossover dose in which the linear induction term is equal to the nontarget term. The crossover dose can be found, for example, from Eq(5.14) as:

$$D_{cr} = \frac{\kappa(L)}{\alpha(L)} \tag{5.17}$$

A dose-dependent RBE in then found for the NTE model given for ions of LET, L, at dose, D_L by:

$$RBE_{NTE} = \frac{\alpha(L)}{\alpha_\gamma} + \frac{\kappa(L)}{\alpha_\gamma D_L} = RBE_{TE}\,(1+\frac{D_{cr}}{D_L}), \tag{5.18}$$

which is assumed to hold down to a possible threshold dose for the non-targeted effect. The RBE is thus seen to be dose dependent even at doses below where cell sterilization and the β-term no longer contribute. For chronic irradiation at low fluence as occurs in space, the lower limit or a threshold dose for NTEs becomes an important consideration, and little is known in this regard. Many other considerations need to be addressed including the role of protective NTEs such as the induction of apoptosis, the tissue specificity of NTEs, and temporal aspects.

5.3.2 Saturation mechanisms in biological responses

The declining biological effectiveness at the high ionization density observed in radiobiology experiments can be due to several mechanisms, as described in **Table 5.4**. The first mechanism is what is termed "overkill effects," which occur due to energy deposition exceeding a value that is needed to cause an effect. In terms of an action cross section, saturation occurs when the cross section reaches a nearly constant value for increasing ionization densities. A second mechanism is denoted as "thindown," which results when the spatial distribution of the δ-ray brush from an ion becomes limited by kinematics to a size smaller than the biological target size, although the ionization density is still large, often occurring at a velocity at which the Bragg ionization peak occurs. Since thindown depends only on the velocity of the ion and not on Z, it is determined by kinematics. A third mechanism may occur for endpoints such as mutation, neoplastic transformation, or perhaps cancer induction when a significant cell killing probability reduces the viability of mutant or carcinogenic cells. Each of these mechanisms needs to be considered when describing the dependence of RBE or QFs with energy and charge as well as dose. A further consideration for cancer data is the role of competing risks from other causes of death, which also may vary with dose and radiation quality.

Table 5.4. Summary of mechanisms for decline in biological effectiveness at high-energy densities.

Mechanism	Impact on RBE	Impact on Cross Section, σ
Overkill	RBE declines like 1/LET	σ constant
Thindown	RBE declines >1/LET	σ decreases rapidly
Competing risks from cell death or other tumors	Dose dependent decrease at higher doses	σ does not apply at H>1

H = number of cell hits per particle.

5.4 Risk Cross Sections and Coefficients

Descriptions of radiobiology data in terms of action cross sections lead naturally to the idea of a risk cross section, which originates in the ideas of Katz[162,165,198] and is considered by Hoffman et al.[199] and Curtis et al.[200] Such an approach was also discussed in NCRP Report No. 137.[201] In this approach, the form for a risk calculation as $R = R_0 \times D \times Q/DDREF$ is replaced by $R = R_0 \times \Sigma \times F$ were Σ denotes a risk cross section. Parametric forms for Σ, as dependent on LET or Z^{*2}/β^2 fit to available experimental data or to the ICRP quality function, were considered in NCRP Report No. 137.[201] At first glance, it appears that the risk cross section is merely an alternative algebraic representation of the existing calculation replacing dose and Q by fluence and Σ, respectively. What was lacking in NCRP Report No. 137[201] was a description of particle track-structure and biophysical considerations on the extrapolation to low dose. We hypothesize that risk cross sections would be useful to NASA if placed in the context of using track-structure and biophysical models to extrapolate experimental observations to other particle types and from acute responses at relatively high doses or fluences to chronic exposures of interest.

Another approach was developed by which to consider the neutron components of the Atomic-bomb exposures in Japan. Here, Kellerer and Walsh[114] made a direct estimate of a neutron risk coefficient for a typical fission neutron spectrum. Using LSS data to estimate the neutron risk directly avoids the need for the use of the DDREF and its associated uncertainties. The method would not be applicable to space radiation or even other neutron energies, however, because no

human data fit a risk coefficient for these radiation types. One idea is that a neutron risk coefficient would represent the maximum value to be expected for any cosmic ray. However, the uncertainties associated with the neutron risk coefficient – especially with its smaller contribution in the dose estimates from DS02 compared to the earlier DS86 estimates as well as the complex mixture of particles in space – make knowledge of such a maximum estimate of limited value. Furthermore, the space radiation environment is variable, including solar cycle modulation of the GCR energies, random SPE occurrences with variable energies and total fluence, and shielding modifications to the proportion of secondary radiation. Therefore, as in the NCRP Report No. 137 description of a risk cross section, the lack of an underlying track-structure description and dose response model of proton and heavy ion radiobiology limits the applicability of such an approach for describing space radiation risks.

The ideas discussed above on track-structure models can be used to allow a risk cross section to be written as[188,189]:

$$\Sigma(Z,E) \quad = \quad \Sigma_0 P(Z,E) + \frac{\alpha_\gamma LET}{6.24}(1 - P(Z,E)) \tag{5.19}$$

with

$$P(Z,E) \quad = \quad (1 - \exp(-Z^{*2} / \kappa\beta^2))^m \tag{5.20}$$

where the parameters, Σ_0, m, and κ should be based on subjective estimates from radiobiology experiments, and the low-LET slope, α_γ, estimated from human epidemiology data for γ-rays. Using Eqs(5.19) and (5.10), a QF function is then written:

$$Q_{NASA} \quad = \quad (1 - P(Z,E)) + \frac{6.24(\Sigma_0 / \alpha_\gamma)}{LET} P(Z,E) \tag{5.21}$$

The interpretation of the parameters is quite general, and is not tied to a particular track-structure models per se, but rather is an efficient parameterization of radiobiology data for particles. The parameters can be described as follows: Σ_0 is the maximum value of the cross section, which is related to RBE_{max} for the most biologically effective particle types. m is the slope of the cross section for increasing ionization density, with values m>1 necessary to have RBE>1. κ determines the saturation value of the cross section, where the RBE begins to decline. To estimate these parameters, high-energy protons of about 150 MeV have an LET similar to γ-rays as well as a kinetic energy below where nuclear reactions become important and many experiments have shown a biological effectiveness very similar to γ-rays. For this energy proton, we have P(Z,E)<<1, and Q ~1. For solid cancer risks, radiobiology data are sparse. However, the largest RBE for HZE nuclei is in the range from 20 to 50 for solid tumors in rodents, and for chromosomal aberrations and mutations in human cells (see **Figure 5.12**). A lower value is found for leukemia. This assumes a linear dose response at low particle dose, ignoring NTEs or other possible mechanisms, leading to deviation from linearity. Thus, for example, if a peak RBE value of approximately 40 is assumed for Si at 100 keV/μm where P(Z,E)~1, Σ_0 / α_γ can be estimated as 40$\times$100/6.24, with the inclusion of the DDREF discussed below. Only the ratio, Σ_0 / α_γ is considered here to simplify parameter estimates. Alternative choices for the monoenergetic particle in which the peak occurs would not change numerical estimates appreciably, and

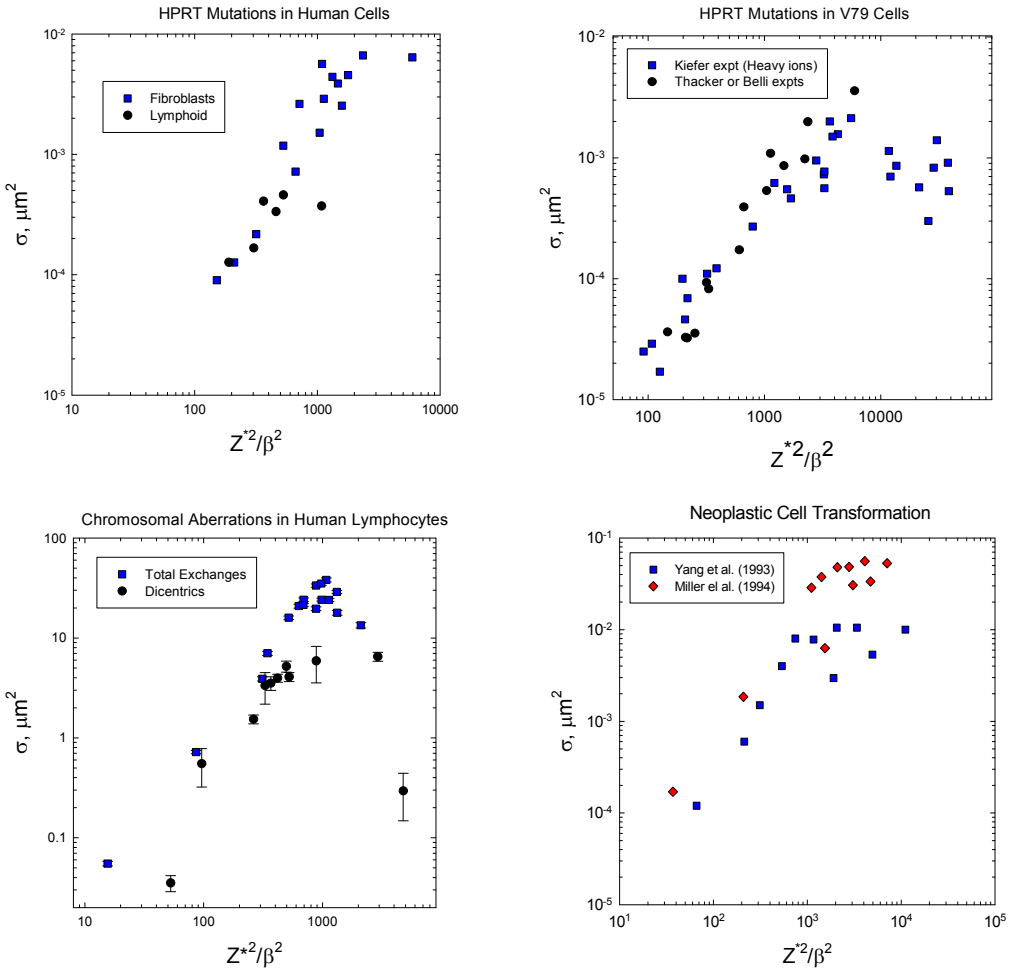

Figure 5.12. Action cross sections vs. Z^{*2}/β^2 for several biological endpoints in mammalian cells. Experimental data for total exchanges (George and Cucinotta, unpublished),[144] dicentrics,[202,203] HPRT mutations in human fibroblasts,[204,205] human lymphoid cells,[206] HPRT mutations in V79 Chinese hamster cells,[148,175,177] and C3H10T1/2 neoplastic transformation.[146,196,207,208]

calculations should include uncertainty analysis through the use of PDFs to represent subjective assessments of ranges for each parameter. A similar estimate of Σ_0 could be made from the Kellerer and Walsh[114] estimate of the neutron risk coefficient if one chooses the particle with the maximum effectiveness.

Defining uncertainty ranges for the three parameters of Eq(5.21) can be made in the following manner: Based on studies of past radiobiology experiments, values of *m* are narrowly defined over the interval from >1 to ≤ 4 with m=2 and 3 occurring most frequently,[161,185,209] including fits to Harderian gland tumor data, and neoplastic transformation as well as gene mutation or chromosomal aberrations in mammalian cells with heavy ion beams. The uncertainty range of Σ_0 corresponds to the range for the maximum Q value for the most effective particle. Lastly, the value of κ requires studies of ions with different energy and *Z* to identify the most effective energy or value for Z^{*2}/β^2. Values can be estimated from past radiobiology experiments. **Table 5.5** illustrates how E changes for different *Z* for fixed values of Z^{*2}/β^2; eg, the maximum effectiveness for protons and He is expected near 0.5 MeV and 1 MeV/u, respectively. Experiments with Fe nuclei

suggest the peak effectiveness is approximately 600 MeV/u, with experiments performed at lower or higher E showing a lower effectiveness (**Figures 5.3 and 5.12**). A reasonable range for the RBE peak for Fe is energies of 500 to 1000 MeV/u, which correspond to Z^{*2}/β^2 between 900 and 1300 (**Table 5.5**). (Note: The value of κ corresponds to roughly one half the value of Z^{*2}/β^2 in which the peak for the RBE occurs.) Less is known for other Z values. Basing QFs or risk cross sections related to an underlying track-structure model provides improved confidence in these descriptions, including that the energy at which the Q is maximum, would be similar to the value of Z^{*2}/β^2 for the maximum found for Fe nuclei. PDFs describing possible ranges of values are described below.

Table 5.5. Kinetic energy values for different charge number, Z, corresponding to fixed Z^{*2}/β^2. Calculations use the Barkas model[210] of the effective charge number.

	Kinetic Energy (MeV/u) for Charge Number (Z) at fixed Z^{*2}/β^2						
Z^{*2}/β^2	1	2	6	10	14	20	26
100	4.7	19.3	234	>10 000	NA	NA	NA
250	1.85	7.5	75.5	272	1070	NA	NA
500	0.93	3.75	35.5	110	264	1155	NA
750	0.61	2.5	23.3	69.4	153	424	2042
1000	0.45	1.85	17.2	50.5	108	272	707
1250	0.35	1.46	13.7	39.8	83.2	199	445
1500	0.28	1.2	11.3	31.6	65.4	157	326
1750	0.24	1.01	9.7	27.8	57.1	130	258
2000	0.2	0.88	8.4	24.2	49.4	110	214

Describing radiation quality effects in terms of Z^{*2}/β^2 is consistent with radial dose models of track-structure, and describes some aspects of stochastic track-structure models. Both LET and the ionization cross section for δ-ray production are proportional to Z^{*2}/β^2; however, LET has other important Z- and β–dependent terms at low energy due to atomic shell structure and nuclear stopping corrections, and at high energies due to the Fermi density effect. The use of Z^{*2}/β^2 does not take into account differences in track-width between two particles with identical Z^{*2}/β^2. This effect will be most important at low energy (<10 MeV/u). Only light ions make important contributions at these energies for GCR because of their longer ranges and the large nuclear production cross sections for hydrogen and helium in tissue. Possible deficiencies of radial dose in describing track-structure would include the absence of a description of differences in biological effectiveness of different δ-rays energies, especially for energies below 10 keV. Tracks of low-energy hydrogen and helium nuclei will contain a higher fraction of δ-rays of these energies, thus possibly increasing their biological effectiveness compared to higher Z nuclei of the same Z^{*2}/β^2. Stochastic track-structure models have not been applied to any great extent in describing heavy ion effects, except for modeling DNA damage. It will be important to extend these models to endpoints that are more closely related to cancer risk in future to understand any shortcomings in using Z^{*2}/β^2 in the description of risk cross sections.

6. Revised NASA Model for Cancer Risks and Uncertainties

In this section, we integrate the new findings and observations described in this report to introduce a revised NASA assessment model of space radiation cancer risk. **Figure 6.1** shows a flow chart of the major components of the calculation. In using the BEIR VII approach, we recommend a departure from NCRP Report No. 132[6] whereby we transfer incidence rates from exposed cohorts to the U.S. rather than use mortality rate transport. The ratio of U.S. background rates for mortality to incidence are then used to convert REIC to REID estimates. Arithmetic weighting of multiplicative and additive risk transfer models are used to transfer to the U.S. population in the same manner as NCRP Report No. 132.[6] The preferred multiplicative transfer weights, ν_T, are listed in the last column of **Table 4.3**. An alternative calculation for lifetime never-smokers (NS) is also described by the revised NASA model using the adjusted rates for never-smokers for lung, stomach, bladder, oral cavity, and esophagus cancers described in Section 3 of this report. For the ERR and EAR functions, we prefer the UNSCEAR model fitted to the LSS data. The BEIR VII report assumes no age at exposure dependence of cancer rates above age 30 y, and uses LAR instead of REID in fitting the LSS data. Furthermore, Appendix D of the UNSCEAR report[17] showed an improved fit to the LSS data for Eq(3.11) used by UNSCEAR as compared to Eq(3.9) with c=0 used by BEIR VII. Therefore, the UNSCEAR[17] models are recommended for most tissue sites. For several tissues that UNSCEAR did not consider, we use the results from Preston et al,[92] however, and the remainder term adjusted accordingly. For breast and thyroid cancers, we follow the BEIR VII recommended models based on meta-analysis of several exposed cohorts. **Table 6.1** summarizes the sources of ERR and EAR functions used in the recommended NASA model. We assume an average DDREF value of 1.75 for solid cancer risks similar to the value by the NIH,[93] which is the GM value of the PDF for the DDREF used in our

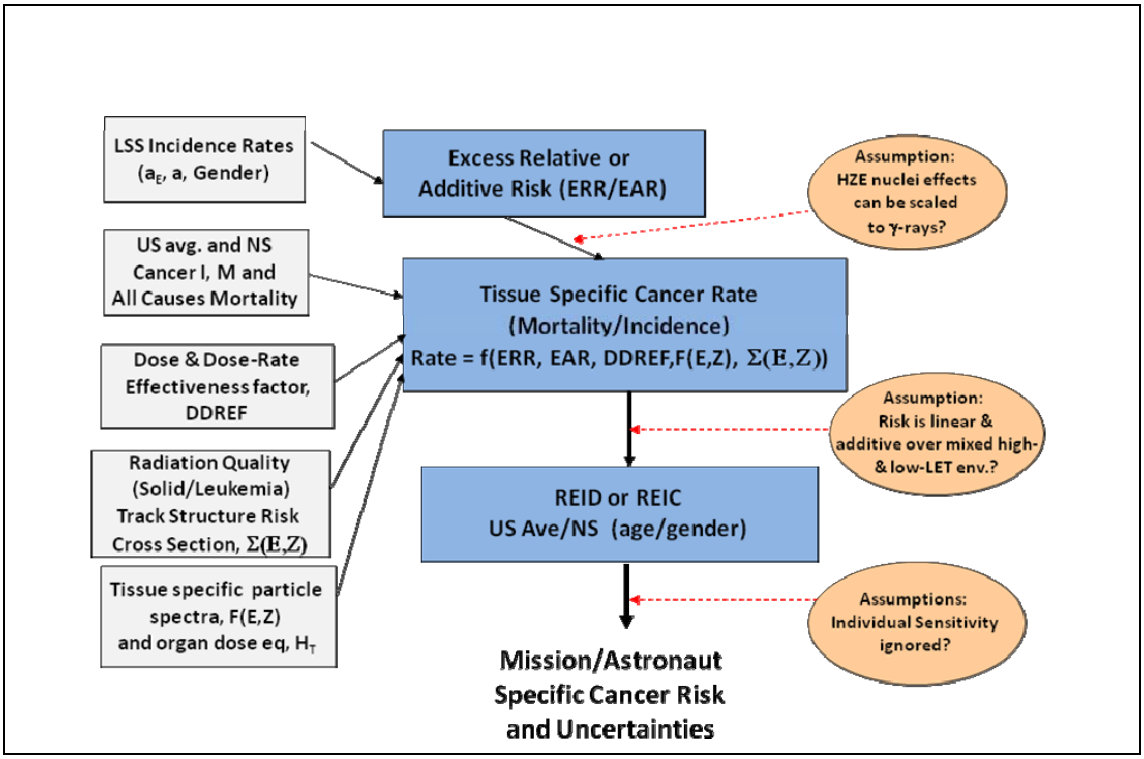

Figure 6.1. Flow chart for REID and REIC calculations.

uncertainty analysis. In calculating leukemia risk, no DDREF value is used. The quadratic dose response term in fits to the LSS data are to be ignored; however, they should be considered as SPEs with dose-rates >0.1 Gy/hr.

The tissue-specific cancer incidence rate for an organ dose equivalent, H_T, is written:

$$\lambda_I(H_T, a_E, a) \quad = \quad [v_T ERR(a_E, a)\lambda_{0I}(a) + (1 - v_T)EAR(a_E, a)]\frac{H_T}{DDREF} \tag{6.1}$$

where *ERR* and *EAR* are the excess relative risk and excess additive risk per Sievert, respectively. The tissue-specific cancer mortality rate for each tissue site is written:

$$\lambda_M(H_T, a_E, a) \quad = \quad [v_T ERR(a_E, a)\lambda_{0M}(a) + (1 - v_T)\frac{\lambda_{0M}(a)}{\lambda_{0I}(a)} EAR(a_E, a)]\frac{H_T}{DDREF} \tag{6.2}$$

The rates for each tissue using Eq(6.2) are summed to estimate the REID using Eq(3.4). A comparison of Effective doses that lead to REID=3%, under the assumption of equal organ dose equivalents for each tissue, can be made to the current dose limits at NASA. These comparisons are shown in **Table 6.2** where we also show a similar calculation using the BEIR VII model. All calculations used recent cancer incidence and life-table data for the U.S. population, which is for 2005 (SEER, 2008).[211] In the recommended NASA model, dose limits are slightly less restrictive at younger crew ages (<40 y), but become more restrictive above age 40 y and older. We also show in **Table 6.2a and 6.2b** the dose limits that are recommended for lifetime never-smokers based on the analysis described in Section 3. The recommended never-smoker limits are more than 20%, or 30% less restrictive for males and females at age 30 y, respectively, than the model based on the average U.S. population with larger differences at older ages of exposure. However, estimates for never-smokers are more restrictive than those for the NCRP model; ie, above about age 50 y.

Table 6.1. Tissue-specific cancer risks considered in recent studies that are used in the NASA revised model.

Tissue	BEIR VII	UNSCEAR	Preston et al	NASA 2010
Stomach	X	X	X	UNSCEAR
Colon	X	X	X	UNSCEAR
Liver	X	X	X	UNSCEAR
Lung	X	X	X	UNSCEAR
Breast	X	X	X	BEIR VII
Prostate	-	-	X	Preston et al
Uterus	X	-	X	Preston et al
Ovary	X	-	X	Preston et al
Bladder	X	X	X	UNSCEAR
Esophagus	-	X	X	UNSCEAR
Brain-CNS	-	X	X	UNSCEAR
Thyroid	X	X	X	BEIR VII
Oral Cavity	-	-	X	Preston et al
Remainder	X	X	X	Preston et al
Leukemia	X	X	-	UNSCEAR (Little et al[10])
Nonmelanoma Skin	X	X	X	Future work
Bone Cancer	-	X	X	Future work

Table 6.2a. Effective dose limits for females on 1-y missions for a 3%REID assuming equivalent organ dose equivalents.

Age, y	NASA 2005	BEIR VII	NASA 2010 Avg. U.S.	NASA 2010 Never-smokers
30	0.5 Sv	0.55 Sv	0.49 Sv	0.68 Sv
40	0.6	0.59	0.52	0.76
50	0.9	0.64	0.57	0.84
60	1.6	0.73	0.66	0.97

Table 6.2b. Same at Table 6.2.b but for males.

Age, y	NASA 2005	BEIR VII	NASA 2010 Avg. U.S.	NASA 2010 Never-smokers
30	0.6 Sv	0.79 Sv	0.73 Sv	0.93
40	0.8	0.80	0.79	1.04
50	1.15	0.83	0.87	1.17
60	2.0	0.94	1.0	1.38

6.1 Track-structure-based Risk Model

As shown by Eq(5.19), calculations with radiation QFs and a risk cross section are related to each other through a simple algebraic formula. However, the approach of Eq(5.19) more naturally aligns with track-structure descriptions of radiation quality, including models for the extrapolation of experimental data from acute to low dose and dose-rates and other radiation qualities. In the track-structure-based model, Eq(6.1), or similarly Eq(6.2), is replaced by:

$$\lambda_{ZI}(F_T, a_E, a) \quad = \quad \frac{\lambda_{\gamma I}(a_E, a)}{DDREF}\left\{D_T(Z,E)(1-P(Z,E)) + \frac{\Sigma_0}{\alpha_\gamma}P(Z,E)F_T(Z,E)\right\} \qquad (6.3)$$

where $\lambda_{\gamma I}$ is the inner-bracketed term in Eq(6.1) that contains the ERR and EAR functions.

Recommended parameters for the risk cross section are shown in **Table 6.3**. The model contains the three parameters (*m*, κ, and Σ_0) that describe variations with particle type as well as the γ-ray slope (α_γ). However, we also assume a description of "thindown" at low energies. Here Eq(5.19) accounts for the saturation, but not for the thindown, mechanism where the track width becomes smaller than the biological target. For low energies, we modify the cross section by the factor P_E=1-exp(-E/E_{TD}) to account for thindown. The value of E_{TD}=0.2 is based on experimental data for H and He. This factor has a very small impact for heavy ions since at low E they make a very small contribution for GCR or SPEs. The values for Σ_0/α_γ correspond to maximum Q values of 40 and 10 for solid cancer and leukemia, respectively. We assume the parameter κ has distinct values for light and heavy ions (**Table 6.3)**. Equation (5.19) was suggested by radial dose models of track structure. Radial dose models do not account for some aspects of track

Table 6.3. Cancer risk cross section or QF parameters for solid cancer and leukemia risks.*.

Parameter	Solid Cancer	Leukemia
m	3	3
κ	550 (1000)	550 (1000)
Σ_0/α_γ, μm^2 Gy	7000/(6.24)	1750/6.24
E_{TD}	0.2 MeV/u	0.2 MeV/u

*Values in parenthesis for when distinct values for light ions ($Z \leq 4$) are to be used.

structure, as discussed in Section 5, which suggests that the models do not allow us to describe light and heavy particles with a single parameter set.

Radiobiological experiments have shown the peak effectiveness at about 600 MeV/u for Fe, 0.5 MeV for protons, and 1 MeV/u for helium, which led to our distinct choices for heavy and light nuclei. As another example, several studies show the peak for Si to be in the range of 90 to 300 MeV/u for CA (George and Cucinotta, unpublished),[144] gene mutation,[206] and neoplastic transformation.[146,212] However, more detailed studies are needed to improve estimates. The absence of animal tumor data for Si an important issue. The PDF describing κ discussed below covers the range of existing data. Although there is likely some further dependence of κ on Z, there is little information to make more informed choices. This approach simplifies the calculation of uncertainties to two distributions of particles at each tissue site – F_{LI} for Z<5, and F_{HI} for Z≥5 – and provides flexibility in uncertainty analysis. Future studies can aim to improve these descriptions of particle track structure. An alternative approach would assume Q(L) is similar to the form used by the ICRP, but with the peak value (currently 100 keV/μm) shifting with Z to higher values. Such an approach would require LET spectra for each Z to be determined, while the approach used here allows a simplification into just two spectra for light and heavy particles, and includes considerations of the uncertainty in the rising and falling slope of Q with changing ionization density.

The use of a DDREF in Eq(6.3) needs to be addressed. Since we are assuming a model extrapolation from high to low dose, the DDREF is included in the scaling approach. The alternative would be to ignore the DDREF; however, the possibility of dose and dose-rate dependencies for low and medium ionizing particles would need to be considered in more detail than is allowed by the current approach.

The model represents several changes from the ICRP QF: First, we assume a smaller maximum Q for leukemia than for solid cancer based on existing animal and human data. The RBE value for leukemia for fission neutrons is reported in the range of 3 to 5 for AML.[138,160] However, there is little data for other types of leukemia. Data for heavy ions are sparse but also suggest a value below 10 and perhaps as low as 1. We assume the maximum Q is 10 for low-energy protons (~0.5 MeV). For projecting solid cancer risk, a maximum Q value of 40 is used. This value is about the average of the different values of RBE_{max} for the most effective particle found in animal tumor induction studies or cellular endpoints, such as chromosomal aberrations or gene mutation, and is consistent with values for neutrons for similar endpoints. Second, the NASA QF accounts for experimental and theoretical observations that radiation quality is a function of Z and E. The cancer risk cross section or related QF is expressed in terms of the track structure parameter, $X_{tr} = Z^{*2}/\beta^2$, and we assume the Barkas form for the effective charge function[210]. The QF has an additional dependence on LET in the denominator of Eq(5.21), which relates the particle track structure to the absorbed dose. **Figure 6.2** compares the NASA QF to the ICRP model used at NASA in the past for p, C, Si, and Fe nuclei vs. LET, thus illustrating the differ-

ences as described. The preferred slope on the rising side with increasing ionization density of m=3 is different than the ICRP Q(LET), which rises approximately as m=2. Our expectation is

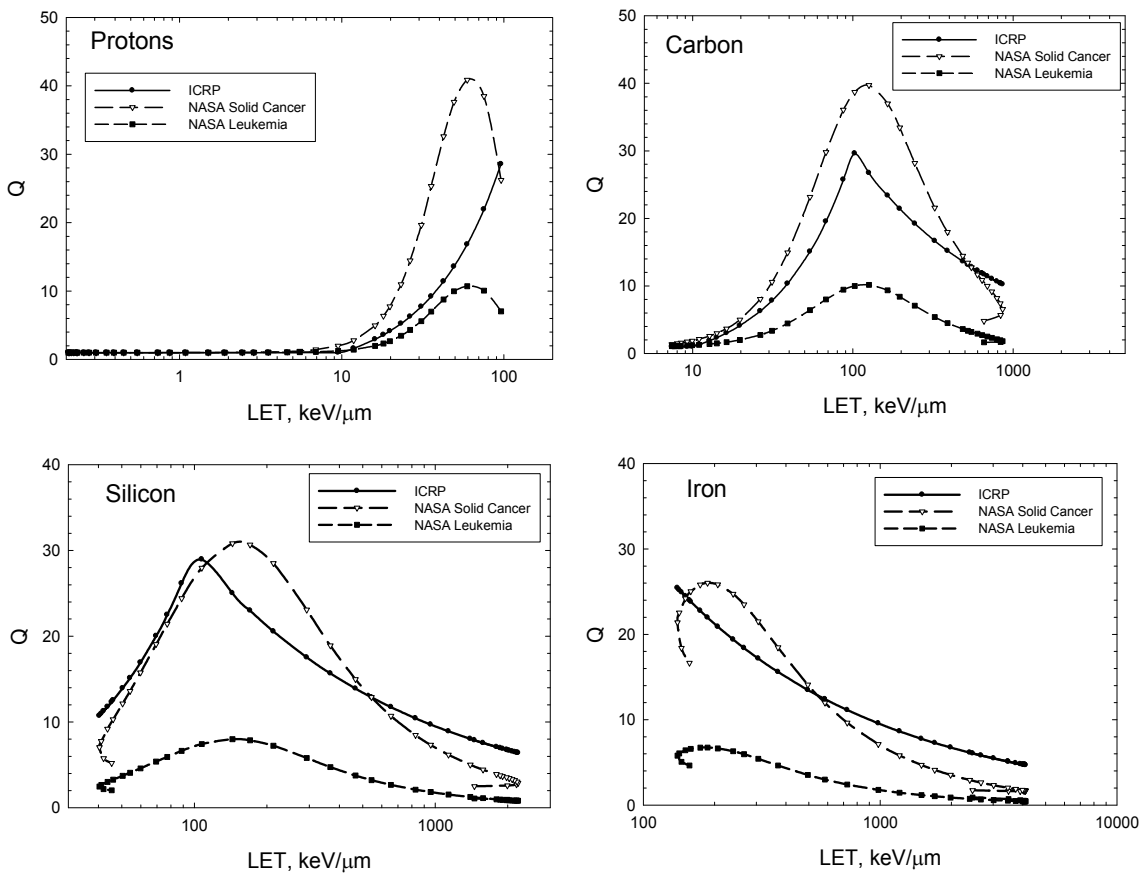

Figure 6.2. Comparison of LET dependence for H, C, Si, and Fe nuclei in the proposed NASA QFs for solid cancer and leukemia risk estimation to QFs from ICRP.[26]

that the proposed NASA QFs will not modify point estimates of risk substantially, except for smaller GCR-induced leukemia estimates. This will lead to different assessments of radiation shielding effectiveness, and an improved model of the uncertainty distribution because of the better representation of existing radiobiology knowledge than is provided by LET-dependent QFs.

6.2 Updates to Radiation Transport Codes

Using the HZETRN code or similar radiation transport codes, the fluence spectra, $F(X_{tr})$, can be found by transforming the energy spectra, $\phi_j(E)$, for each particle, j of mass number, and charge number A_j and Z_j, respectively, as:

$$F(X_{tr}) \quad = \quad \sum_j \left(\frac{\partial X_{tr}}{\partial E} \right)^{-1} \phi_j(E) \tag{6.4}$$

where we evaluate the Jacobian in Eq(6.4) using the Barkas[210] form for the effective charge number given by

$$Z^* \quad = \quad Z(1-e^{-125\beta/Z^{2/3}}) \tag{6.5}$$

The tissue-specific cancer incidence rate for GCR or SPEs can be written as:

$$\lambda_I \quad \approx \quad \frac{\lambda_{I\gamma}}{DDREF}\left\{\sum_j \int dE\phi_{jT}(E)S_j(E)(1-P(X_{tr})) + \frac{\Sigma_0}{\alpha_\gamma}\int dX_{tr}F(X_{tr})P(X_{tr})\right\} \tag{6.6}$$

The first term on the right side of Eq(6.6) can be well approximated by the tissue-averaged absorbed dose times the low-LET risk coefficient. This approximation can be shown to lead to <10% overestimation of its true value. However, in the REID calculation, the error is even smaller because the second term of the right side of Eq(6.6) is dominant. We modified the HZETRN and BRYNTRN codes to perform the exact calculation; but for the Monte-Carlo uncertainty analysis we can use the following form for the radiation cancer rate for the mixed particle and energy fields in space:

$$\lambda_I \quad \approx \quad \frac{\lambda_{I\gamma}}{DDREF}\left\{Dose + \frac{\Sigma_0}{\alpha_\gamma}\left[\int dX_{tr}F_{LI}(X_{tr})P_{LI}(X_{tr}) + \int dX_{tr}F_{HI}(X_{tr})P_{HI}(X_{tr})\right]\right\} \tag{6.6'}$$

where we separate out spectra for light ions with Z≤4, F_{LI} from heavy ions, and F_{HI} with higher charges as described above. A summation of all cancer types is made for the radiation contribution to the survivor function that enters into the REID or REIC formula in evaluating specific tissue risks, and to evaluate the overall cancer risk. Fluence spectra are averaged over each tissue using body-shielding models. Previous versions of HZETRN and BRYNTRN had included Z=1 and Z=2 target fragments as part of the transported particle energy spectra. However, the Z=3 to Z=8 target fragments in tissues that are of low energy (<10 MeV/u) and have very small ranges were modeled using parametric dose functions. To more readily include their contributions to the revised risk model and associated error analysis, we modified these codes by adding the target fragment spectra into the Z=3 to Z=8 energy spectra for primaries and projectile fragments on entry to the existing DMETRIC and the new cancer risk cross-section subroutines in these codes.

We show the resulting differential REID spectra vs. X_{tr} at solar minimum behind increasing amounts of aluminum shielding in **Figure 6.3**. Calculations are made with the HZETRN code using the Badhwar and O'Neill GCR model[51] and QMSFRG nuclear cross-section database.[39,72] Results are shown on a linear-log plot such that the area under the curve for each decade of X_{tr} is equally weighted. Leukemia risk shows a reduced maximum Q-value compared to solid cancer risks, resulting in particles at lower values of X_{tr} that make larger contributions compared to solid cancer risks. **Figure 6.3** shows sharp spikes at the integer value of Z^2 corresponding to different GCR charge groups. For example, at small values of X_{tr} we see peaks at 1 and 4 corresponding to protons and He nuclei. At large values of X_{tr} we observe a prominent peak near 626, which corresponds to Fe nuclei. These sharp peaks correspond to the contributions from relativistic particles.

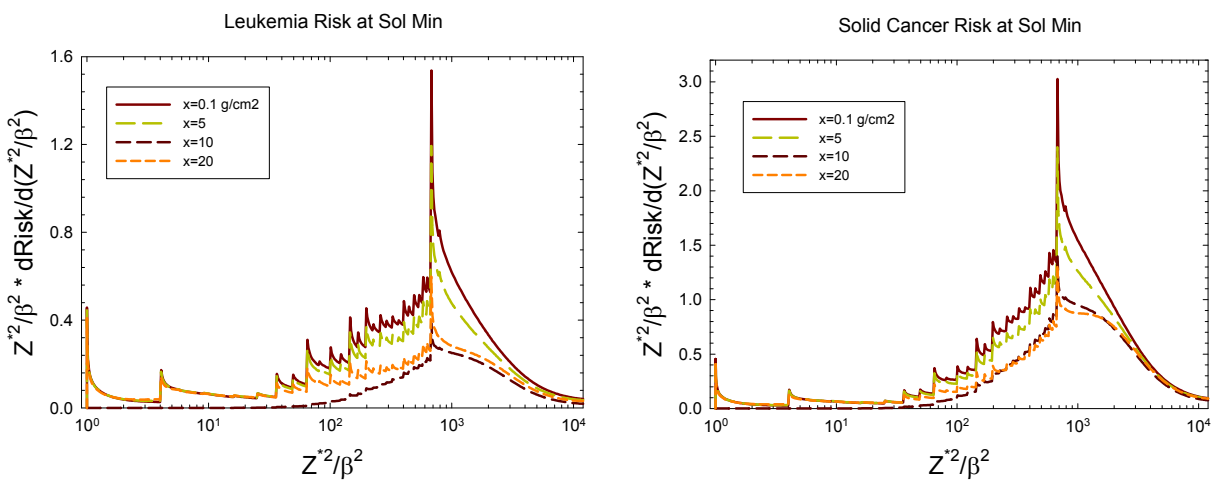

Figure 6.3. Leukemia and solid cancer risk distribution vs. Z^{*2}/β^2 for increasing amounts of aluminum shielding for 1 y in deep space at solar maximum with the August 1972 SPE.

6.3 Effective Dose and Tissue Weights

In the approach described above, tissue weights, w_T, do not appear in the calculation of REID or REIC; however because Effective dose is still a useful summary variable for mission operations, we estimated gender-specific w_T values (**Table 6.4**) averaged over typical astronaut ages (30 to 60 y). The use of the terminology, "Effective dose" of course refers specifically to the ICRP definition. However NASA continues to make adjustments to methods from the ICRP and NCRP based on the unique circumstances of space radiation protection. The use of this terminology with modified values is intended strictly for internal NASA usage. Several differences in values for the tissue weights estimated here compared to the ICRP values. First, the ICRP includes hereditary risk and nonlethal cancer in its considerations of radiation detriment in recommending w_T values. In comparison, NASA uses cancer-mortality-based risk limits (REID) based on NCRP recommendations[6]. The ICRP averages tissue weights over age and gender, including values for preadults because its simplified methods are intended for use in both occupational and public exposures. Comparison of the ICRP values to gender-specific estimates in the NASA model for adults (30 to 60 y) are shown in **Table 6.4**. Distinct values would occur for different radiation fields because of the different QF used for the leukemia risk estimate. Never-smokers also have different tissue weights than the average U.S. population due to lower contributions from smoking-attributable cancers. The ICRP w_T values for skin, gonad, and thyroid, which make negligible contributions to the REID, can lead to very high estimates of Effective doses for SPEs in which steep dose gradients occur, especially for extravehicular activity risk assessments. The values in **Table 6.4** are good approximations for SPEs or trapped protons; however, for GCR, the leukemia weights are reduced and solid cancer weights are increased as indicated by values in parentheses.

We compare calculations of annual Effective dose in the ICRP model to the NASA-recommended model for ISS missions at solar minimum and maximum in **Figure 6.4**. Comparisons for aluminum and polyethylene shielding are shown. The AP8 model of trapped protons is used, as is the Badhwar and O'Neill model of the GCR environment with quiet-time geomagnetic cutoffs. The CAM [computerized anatomical man] and CAF [computerized anatomical female] models of tissue self-shielding[213] are used to evaluate of organ dose equivalents. **Figure 6.5** shows similar comparisons for 1 y in deep space. The ICRP model, due largely to its higher estimation of con-

tributions for relativistic particles than described here, provides higher estimates at shallow shielding depth. At deep shielding depths, the NASA model is larger due to its assignment of higher biological effectiveness to low-energy proton and helium nuclei produced by neutrons and other particles and from atomic slowing down of primaries. For the various mission scenarios, differences in Effective doses are on the order of 10% to 30%; but the NASA model allows for a more precise uncertainty assessment to be made than the ICRP Q function, whose parameters are difficult to relate to biophysical interpretation. **Figure 6.6** shows predictions of the Effective dose map on the surface of Mars using the MOLA [Mars orbiter laser altimeter] data to determine the vertical height of the carbon dioxide atmosphere and assuming a 10 g/cm^2 aluminum habitat. Shown are results for the 1972 SPE using the King spectra (and the annual GCR at solar minimum. GCR Effective doses will be much larger than SPEs on the martian surface due to the attenuation of the SPEs by the martian atmosphere. Comparisons of **Figure 6.6** will be useful for the selection of future crew landing sites on the Mars surface to minimize crew risks.

Table 6.4. Tissue weights from past ICRP reports, which are gender-average and gender-specific values estimated from the NASA 2010 model for the average U.S. population and a population of never-smokers.

Tissue	ICRP 1991	ICRP 2007	NASA Avg. U.S. Males	NASA Avg. U.S. Females	NASA NS Males	NASA NS Females
Colon	0.12	0.12	0.098	0.057	0.107	0.093
Stomach	0.12	0.12	0.085	0.061	0.125	0.086
Liver	0.05	0.04	0.067	0.047	0.076	0.053
Lung	0.12	0.12	0.289	0.495	0.192	0.322
Bladder	0.05	0.04	0.075	0.033	0.062	0.045
Breast or Prostate	0.05	0.12	0.021	0.053	0.035	0.083
Ovary/Uterus or Testis	0.2	0.08	0	0.044	0	0.067
Brain	-	0.01	0.016	0.01	0.022	0.016
Esophagus	0.05	0.04	0.048	0.01	0.019	0.007
Salivary Gland or Oral Cavity	-	0.01	0.015	0.006	0.003	0.003
Skin	0.01	0.01	0	0	0	0
Thyroid	0.05	0.04	0.002	0.003	0.002	0.004
Bone Marrow	0.12	0.12	0.194(0.15)#	0.10 (0.07)#	0.284 (0.21)	0.138(0.1)
Bone Surface	0.01	0.01	0	0	0	0
Remainder	0.05**	0.12**	0.089	0.079	0.073	0.083
Total Solid cancers	0.88	0.88	0.806 (0.85)#	0.90 (0.93)#	0.716(0.79)	0.862(0.9)

*Remainder organ/tissue defined in ICRP 60: adrenals, brain, trachea, small intestine, kidneys, muscle, pancreas, spleen, thymus, and uterus.
**Remainder organ/tissue defined in ICRP 103: adrenals, extra-thoracic (ET) region, gallbladder, heart, kidneys, lymphatic nodes, muscle, oral mucosa, pancreas, prostate, small intestine, spleen, thymus, and uterus/cervix.
Bone marrow weights in parenthesis are appropriate for GCR where impact of lower Q for leukemia becomes important. The resulting adjustment for over solid cancer weight is shown, and individual tissue weights should then be adjusted accordingly.

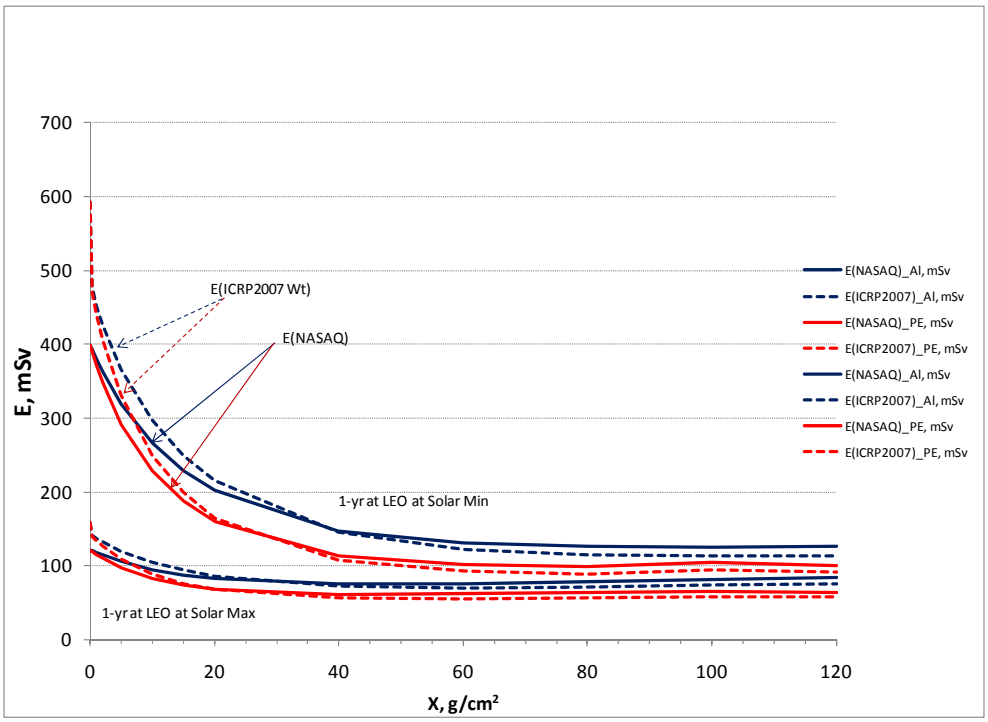

Figure 6.4. Comparison of annual Effective dose for males in ISS orbit (51.6 deg × 400 km) vs. depth of shielding. Values for solar minimum and maximum are shown, comparing ICRP model to recommended NASA model.

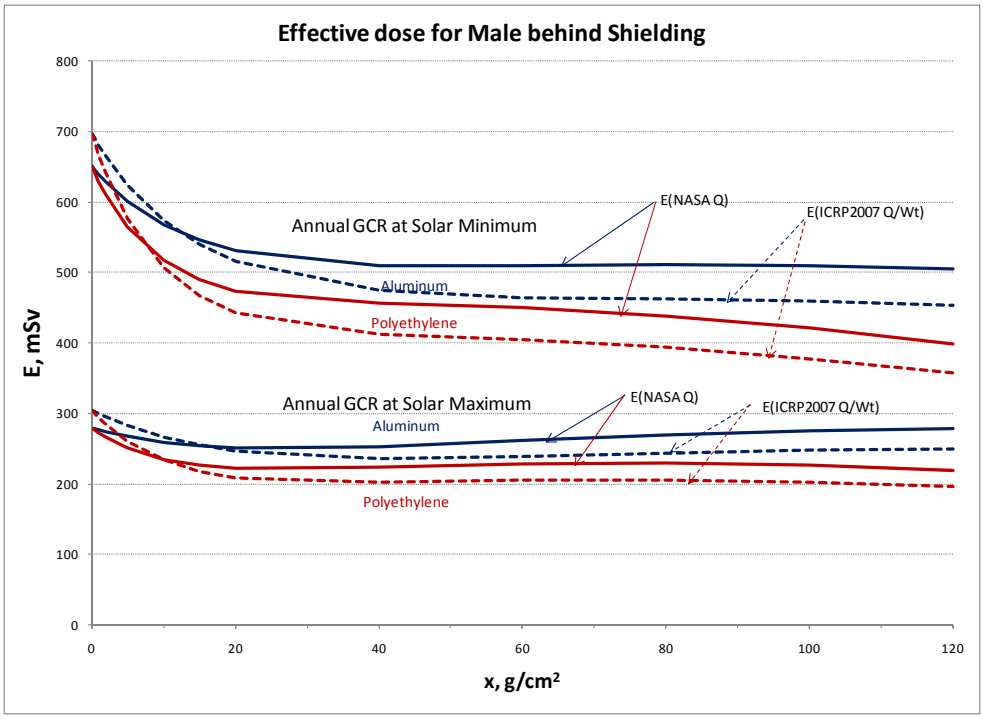

Figure 6.5. Annual GCR Effective doses in deep space vs. depth of shielding for males. Values for solar minimum and maximum are shown, comparing ICRP model to recommended NASA model.

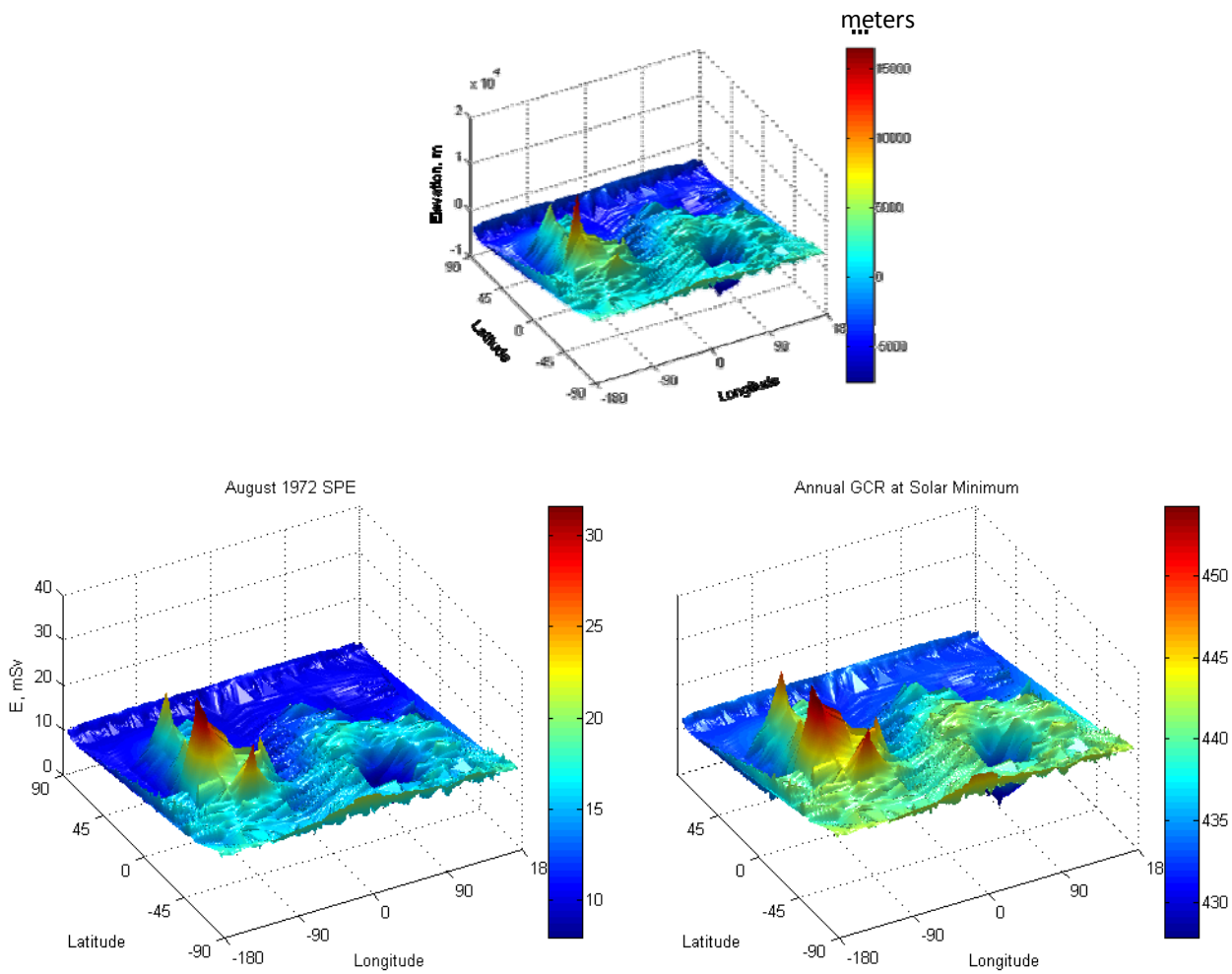

Figure 6.6. (Upper panel) MOLA topography data from the Mars Global Surveyor (http://tharsis.gsfc.nasa.gov) for atmospheric density on Mars surface vs. longitude and latitude. (Lower panel) Effective doses (mSv) from August 1972 SPE (left panel) and annual GCR (right panel) at solar minimum on surface of Mars behind 10 g/cm^2 Al shield.

6.4 Revised Uncertainty Assessment

PDFs describing the uncertainties to the quantiles, x_ξ, for the various parameters in the model are described in **Table 6.5**. Space physics uncertainties were described in Section 2, low-LET uncertainties were described in Section 4, and radiation quality uncertainties were described in Section 5. The subjective PDFs are then employed in Monte-Carlo calculations to describe a given space radiation scenario, as described previously.[12.14,15,20] **Figure 6.7** illustrates the uncertainties in the Q value for solid cancer for monoenergetic particles (Si and Fe) vs. kinetic energy. The median values and 95% CIs are shown. The largest contributor to the Q-uncertainty is the maximum value, Q_{max}, or the value of Σ_0. Our point estimates for Q_{max} of 40 or 10 for solid cancers or leukemia, respectively occur for the most effective proton energy (~0.5 MeV). Values assigned give more weight to the animal model solid tumor data and are influenced by fractionation studies that suggest that higher RBEs are possible. These values are also

consistent with RBEs for gene mutation and chromosomal aberrations in human cells. The resulting PDF has a 95% CI for the maximum value of Q_{max} for solid cancer as [14, 70], which covers most of the range of values from Fe nuclei tumor induction and earlier neutron studies reflective of low-energy protons. The possibility of NTEs suggests that higher values are possible. NTE contributions to uncertainties estimates are discussed below. we use in **Table 6.5** a GM=0.9 for the PDF associated with Σ_0 with the expectation that some tissues would have lower values as found for leukemia; however, there is a lack of information to make a more informed choice. We did not consider uncertainty quantiles for the characteristic energy for thindown, E_{th}, and the γ_m parameter in Eq(5.19). Estimates of values for these parameters are likely correlated with the values of m, κ, and Σ_0, and the addition of quantiles with small influence would not add to the analysis.[214] The addition of a quantile for E_{th} would also create the complication of performing uncertainty analysis for each charge group, rather than the light and heavy charge groups considered here. The possible correlations between DDREF and Q_{max} (or Σ_0/α_γ) are difficult to estimate with existing data, however should be considered in future work.

Table 6.5. Summary of PDF for uncertainty components in NASA model.

Uncertainty Contribution	PDF form for Quantile, x_i	Comment
Low-LET Model:		
Statistical Errors	Normal (M=1.0; SD=0.15)	Revised since NCRP Report No. 126
Bias in Incidence Data	Normal (M=1.0; SD=0.05)	Based on NCRP Report No. 126
Dosimetry Errors	Log-normal (GM=0.9, GSD=1.3)	Based on Preston et al;[92] UNSCEAR[27]
Transfer Model Weights	Uniform distribution about preferred weight	Ignored for breast and thyroid cancers
DDREF	Log-normal (GM=1.0; GSD=1.4)	DDREF=1.75; truncated at 0.75 for inverse dose-rate probability <0.05
Risk Cross Section or Q:		
Σ_0/α_γ	Log-normal(GM=0.9; GSD=1.4)	GM<1 assumes existing data are biased to higher values
κ	Normal (M=1, SD=0.2)	Position of peak estimates suggests variation on sensitivity, target size/distributed targets
m	Discrete M=[1.5,2,2.5,3,3.5,4] with weights [0.05,0.1,0.2, 0.4,0.2.,0.05]	Values restricted over (1.5,4)
Physics Uncertainties:		
$F(Z^{*2}/\beta^2)$ for Z<5	Normal (M=1.05; SD=1/3)	HZETRN does not account for mesons, e-rays, and γ-rays that are low charge and high velocity; may underestimate neutron recoils of low charge
$F(Z^{*2}/\beta^2)$ for Z≥5	Normal (M=1.0; SD=1/4)	HZETRN accurate at high Z
Non-targeted Effects:		
x_{NTE}	Uniform over [0,0.5]	Maximum probability of occurrence of 0.5

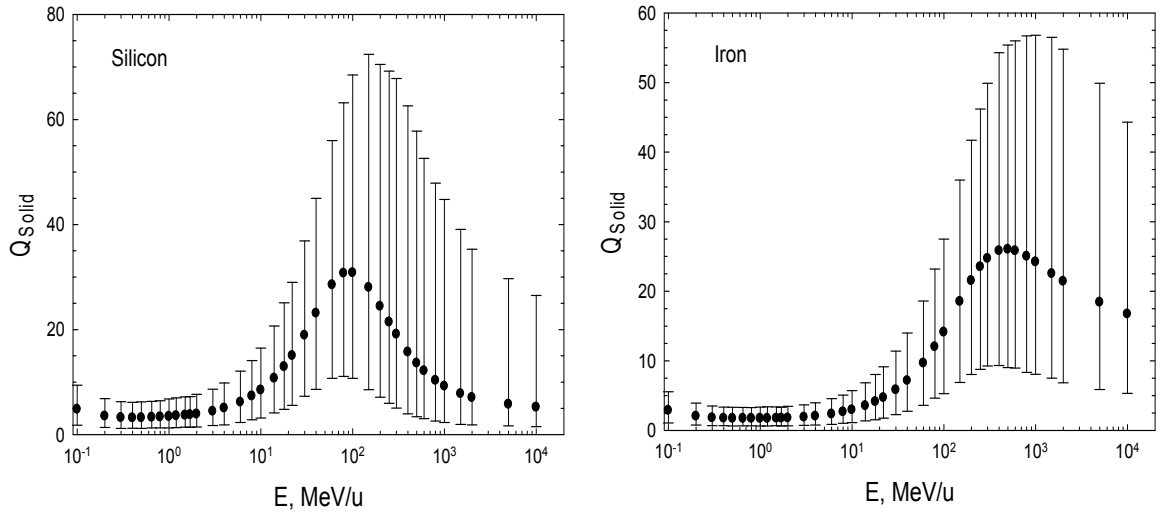

Figure 6.7. Most likely QF values for solid cancer and 95% CIs vs. kinetic energy that results from Monte-Carlo evaluation using 20 000 trials.

In an alternative model of the radiation quality uncertainties, we assume that the slope, *m*, is correlated with the position of the maximum value of Q as determined by the value of κ. After studying the functional dependence of the parameters of Eq(5.21), we find that the position of the maximum Q is held fixed for different values of *m* if we use the constraint:

$$\kappa(m) \quad = \quad \frac{4\kappa_0}{(m+1)} \tag{6.7}$$

where κ_0 is the estimated value from **Table 6.3**, the results of which are shown in **Figure 6.8**. This alternative uncertainty assessment assumes that risk cross section for cancer induction in humans is fairly well described by the existing data, as reviewed in Section 5. In contrast, ignoring the condition of Eq(6.7) places more emphasis on the lack of data for specific models of human cancer such as lung, colon, stomach, etc., such that a wider range of parameter variation is estimated. Equation (6.7) allows uncertainties in the maximum Q value, slope of Q with changing X_{tr}, and kinetic energy at the Q maximum to occur; however values are more constrained compared to the uncertainty analysis described above. A large part of the uncertainty is for particles with small to intermediate Z values, especially at high energy as illustrated by the differences between m=2 and m=3 shown in **Figure 6.8**. The alternative uncertainty model was applied using conditional Monte-Carlo sampling, where a random value of *m* is selected from its PDF prior to sampling for the κ value with central estimate defined by Eq(6.7).

The cancer risk projection for space missions is found by folding predictions of the tissue-weighted X_{tr} spectra behind spacecraft shielding, $F(X_{tr})$, with the radiation cancer rate to form a rate for a Monte-Carlo trial ξ. Results from each trial are binned to form an overall PDF function after a sufficient number of trials (on the order of 50 000) are made. **Table 6.6a** breaks down the contributors to the uncertainty at solar minimum. **Table 6.6b** shows comparisons near solar maximum, assuming the 1972 SPE occurred during a 1-y deep-space mission. The low-LET uncertainties lead to an upper 95% CI approaching 2 times the point estimate, and can be compared to the estimates made in the past listed in **Table 4.4**. The Q uncertainties make up the largest

fraction of the uncertainty. The overall uncertainty is about 3.6, and this factor will increase modestly as mission length is shortened because competition with other risks is smaller at lower risk levels. **Table 6.7** shows a similar calculation using the alternative Q uncertainty model that includes the constraint of Eq(6.7). Uncertainties are significantly reduced in this model with a 2.8-fold overall uncertainty.

Table. 6.6a. Contributions of various uncertainties for 40-y females on a 1-y mission at solar minimum in deep space with a 20-g/cm^2 aluminum shield.

Uncertainties considered	Expected	Mean	Median	STD	Lower 95%	Upper 95%	Fold Uncert.
Epidemiology	3.23	2.95	2.84	0.78	1.61	4.64	1.44
DDREF	3.23	3.40	3.23	1.02	1.78	5.78	1.79
Epidemiology DDREF, Transfer	3.23	3.10	2.79	1.36	1.17	6.44	1.99
Q	3.23	3.92	3.19	2.30	1.87	10.8	3.34
Q and Physics	3.23	3.99	3.28	2.35	1.91	11.1	3.44
All uncertainties	3.23	3.78	2.97	2.70	1.03	11.5	3.56

Table. 6.6b. Contributions of various uncertainties for 40-y females on a 1-y mission at solar maximum with August 1972 SPE in deep space with a 20-g/cm^2 aluminum shield.

Uncertainties considered	Expected	Mean	Median	STD	Lower 95%	Upper 95%	Fold Uncert.
Epidemiology	1.89	1.73	1.63	0.54	0.87	2.94	1.56
DDREF	1.89	2.00	1.89	0.59	1.04	3.38	1.79
Epidemiology DDREF, Transfer	1.89	1.82	1.63	0.81	0.68	3.79	2.01
Q	1.89	2.16	1.71	1.52	0.60	6.49	3.43
Q and Physics	1.89	2.42	1.99	1.53	0.86	6.87	3.63
All uncertainties	1.89	2.24	1.75	1.66	0.60	6.91	3.66

Table. 6.7a. Alternative estimate of radiation quality uncertainties using constraint of Eq(6.7) for 40-y females on a 1-y mission at solar minimum in deep space for a 20-g/cm^2 aluminum shield.

Uncertainties considered	Expected	Mean	Median	STD	Lower 95%	Upper 95%	Fold Uncert.
Q	3.23	3.58	3.15	1.48	1.94	7.44	2.05
Q and Physics	3.23	3.64	3.20	1.53	1.99	7.59	2.35
All uncertainties	3.23	3.47	2.90	2.09	1.03	8.9	2.77

Table. 6.7b. Alternative estimate of radiation quality uncertainties using constraint of Eq(6.7) for 40-y females on a 1-y mission at solar maximum with August 1972 SPE in deep space for a 20-g/cm^2 aluminum shield.

Uncertainties considered	Expected	Mean	Median	STD	Lower 95%	Upper 95%	Fold Uncert.
Q	1.89	2.10	1.84	0.89	1.16	4.41	2.33
Q and Physics	1.89	2.15	1.87	0.92	1.46	4.52	2.39
All uncertainties	1.89	2.04	1.72	1.25	0.60	5.29	2.80

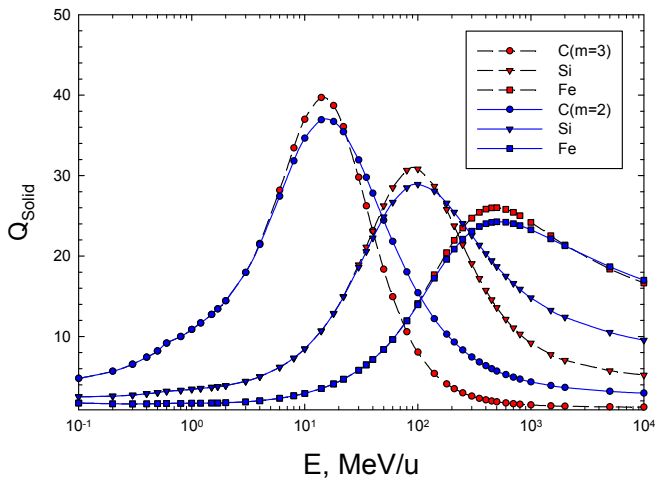

Figure 6.8. Most likely solid cancer QF vs. kinetic energy for C, Si, and Fe nuclei comparing m=2 and m=3 with κ constrained by Eq(6.7).

6.4.1 Uncertainties for never-smoker risk estimates

The uncertainty assessment for never-smokers considers larger errors in background cancer rates for never-smokers compared to average U.S. rates. A distinct transfer weight uncertainty also occurs because of the larger difference between predictions of the additive and multiplicative transfer models. We introduced a normally distributed quantile with M=1 and SD=0.15 to represent statistical errors in background cancer rates for never-smokers. Transfer model uncertainties were treated in the same manner as the average U.S. population with a uniform distribution about the most likely transfer weight value, ν_T. **Table 6.8** shows the results for males and females on 1-y deep-space missions at solar minimum. Decreases for never-smokers compared to the average U.S. population are more than 20% and 30% for males and females, respectively, with larger decreases at older ages of exposure. Several implications are apparent from this comparison. First, risks for astronauts may be significantly overestimated when based on the average U.S. population due to smoking effects inherent in epidemiology data. Second, estimates made here for a mixture model would be reduced even further if a higher multiplicative transfer weight were used. Third, the value of crew selection is substantial when compared to the costs for extra radiation shielding or constraints to launch windows or mission timelines that would lead to a similar risk reduction as this comparison has shown. This is

Table 6.8. %REID predictions and 95% CI for never-smokers and average U.S. population for 1 y in deep space at solar minimum with 20 g/cm^2 aluminum shielding.

	%REID for Males and 95% CI			%REID for Females and 95% CI		
a_E, y	Avg. U.S.	Never-smokers	Decrease (%)	Avg. U.S.	Never-smokers	Decrease (%)
30	2.26 [0.76, 8.11]	1.79 [0.60, 6.42]	21	3.58 [1.15, 12.9]	2.52 [0.81, 9.06]	30
40	2.10 [0.71, 7.33]	1.63 [0.55, 5.69]	22	3.23 [1.03, 11.5]	2.18 [0.70, 7.66]	33
50	1.93 [0.65, 6.75]	1.46 [0.49, 5.11]	24	2.89 [0.88, 10.2]	1.89 [0.60, 6.70]	34

Table 6.9. Estimates of safe days in deep space defined as maximum number of days with 95% CL to be below 3%REID limit. Calculations are for solar minimum with 20-g/cm^2 aluminum shielding. Values in parenthesis are for the alternative assessment that assumes extra constraint on QF uncertainties as given by Eq(6.7).

a_E, y	NASA 2005	NASA 2010 Avg. U.S.	NASA 2010 Never-Smokers
		Males	
35	158	140 (186)	180 (239)
45	207	150 (200)	198 (263)
55	302	169 (218)	229 (297)
		Females	
35	129	88 (120)	130 (172)
45	173	97 (129)	150 (196)
55	259	113 (149)	177 (231)

further illustrated in **Table 6.9**, in which we report calculations for the number of safe days in space at solar minimum for 20 g/cm^2 of aluminum shielding. The gain in the number of safe days for never-smokers compared to the average U.S. population can be contrasted with the results of **Figure 6.5** for large amounts of aluminum or polyethylene shielding. Clearly, gaining knowledge to improve risk assessments has the potential to lead to more substantial reductions in risk projections than the addition of costly radiation shielding or the use of alternative radiation shielding materials. In addition, there are other radiogenic cancers that are also increased by tobacco use that should be considered in future analysis, including colon cancer and leukemia.

6.4.2 Uncertainties Due to Non-targeted Effects

To estimate the uncertainty contribution from NTEs, we introduced a dose-dependent QF trial function and an additional quantile representing the probability that NTEs contribute to cancer risks. Using the harderian gland data as a basis for parameters for the uncertainty assessment, we assume, for a Monte-Carlo trial, the modified QF function:

$$Q_S^{NTE} \quad = \quad Q_S^{TE}(1 + x_{NTE}\frac{D_{cross}}{D_T}) \tag{6.8}$$

where the quantile, x_{NTE} represents the uncertain contribution of NTEs to space radiation cancer risk. We assumed a uniform PDF for this quantile, but with a limited maximum probability of 0.5. We chose not to vary the parametric dependence of D_{cross} and used the harderian gland estimates with no modifications. **Figure 6.9** shows results for risks and uncertainties for absorbed doses of 0.01 and 0.1 Gy of 600 MeV/u Fe. Further comparisons are shw in **Table 6.10**. These results show that about a 2-fold increase in uncertainties compared to TEs alone occurs at low dose (<0.1 Gy) representative of GCR exposures. Extension of the calculations for mixed-particle space environment will depend not only on the NTE probability, but also on information on temporal aspects and likely lower dose or fluence (threshold) for NTE occurrence. Results could be higher or lower depending on these assumptions. The current recommendation is that research using chronic exposures to simulate GCR studying cancer-related processes should be prioritized because of the large impact of the results for NASA. Efforts to validate or refute the importance of NTEs should consider *in-vivo* experiments with representative tissues of human cancer risks, as well as differences between chronic and acute irradiation for small total absorbed doses (<0.3 Gy).

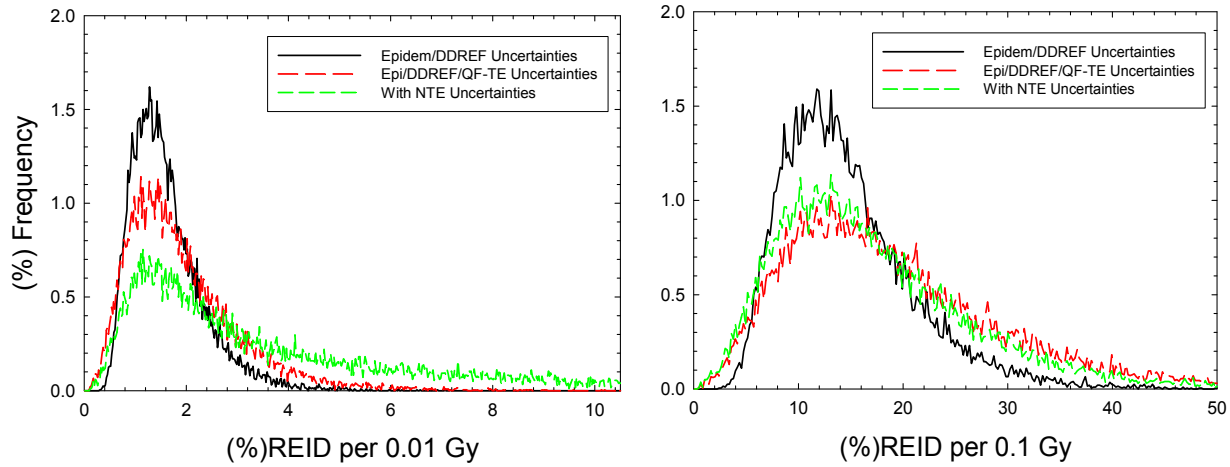

Figure 6.9. Uncertainty assessment for REID distribution for 600 MeV/u Fe nuclei at 0.01 or 0.1 Gy for 40-y males with a limit of 0.5 for maximum probability that NTE occur and average probability of 0.25.

Table 6.10. Influence of NTE on average and upper 95% CL REID for 40-y males exposed to 0.01 Gy (1 rad) of HZE nuclei for different average probability of NTE occurrence, P_{NTE}.

P_{NTE}	%REID for 0.01 Gy of Fe (600 MeV/u)		%REID for 0.01 Gy of Si (1000 MeV/u)	
	Avg.	Upper 95% CL	Avg.	Upper 95% CL
0	1.02	4.41	0.50	2.29
0.1	1.19	5.39	0.56	2.48
0.2	1.58	7.27	0.67	2.74
0.25	1.81	7.84	0.73	2.86
0.35	2.34	8.44	0.89	3.02
0.5	3.31	8.83	1.19	3.18

6.5 Considerations for Implementation of New Methods

Implementation of the recommendations made in this report should consider several areas, including dosimetry requirements, application for the ISS Program, historical records or future epidemiology studies, and new or ongoing NASA trade studies for exploration mission planning. The NCRP recommends updating radiation worker records when revised assessments exceed potential changes of more than 30%.[25] Our recommendations for Effective doses and REID projections would include instances in which assessments would be above or below a 30% difference. Exposure records at NASA include mission dosimetry values, Effective dose and organ dose equivalents using the HZETRN/QMSFRG and CAM/CAF models,[73] and projections of REID and REIC. It will be a small undertaking to reassess past ISS exposures and risk levels using the revised approach, but a much larger effort for past shuttle missions. Effective doses on shuttle missions were small; typically below 10 mSv. We recommend that exposures for the past and future ISS missions be updated using the new methods. For space shuttle and other past missions, there is no strong rationale to update organ dose equivalent records; however, REID and REID values could easily be updated using existing databases. For NASA trade

studies, the approaches here are recommended for future mission analysis. Models of radiation risks and uncertainty analysis are subjective when applied to human risk estimates from space radiation. Nevertheless, it continues to be a reasonable approach to carry acceptable levels of risk as specific REID values, and to make uncertainty assessments of the upper 95% CL as an additional safety consideration. Trade studies can explore the value of potential mitigation measures to reduce uncertainty factors and REID projections, but radiobiological research remains the primary method to reduce uncertainties for all space missions.

Dosimetry in space flight is complex because of the many types of particles and energies comprising space radiation. Mission dosimetry includes area and crew personnel dosimetry. Area dosimetry used in the past includes TEPCs, charged-particle hodoscopes to measure Z and E spectra over a limited range, and passive dosimeters made up of TLDs and CR-39 nuclear track detectors. Typically, passive dosimeters used as area detectors are also carried by crew members as their dosimeter of record. Each of these dosimeters can measure various aspects of the radiation environment in space, but none can measure all radiation components. Furthermore, cancer risks are evaluated at sensitive tissue sites, which, of course, are not directly measured and must be estimated with computer models. NASA thus uses area and crew dosimetry in conjunction with the HZETRN/QMSFRG code to make estimates of organ dose equivalents in which mission-specific predictions are normalized to the dosimetry of record.[25] The recommendations of this report would not change this approach; however the new NASA QFs and REID/REIC calculations would be employed. Biodosimetry results from the ISS crew would be unchanged, and these results already include track structure effects described in this report.

Implementation of the recommendation made in this report to estimate cancer risks and Effective dose limits for never-smokers should consider several factors. Ensuring continued never-smoker status for the remainder of a lifetime should be a minor concern because most individuals make a decision on tobacco usage at a young age. The influence of secondhand smoke and risks for former smokers also needs to be considered. The CDC has estimated the number of secondhand smoke-attributable cancers,[101] which indicates that the number is a much smaller fraction of cancer risks than the corrections considered in this report. The potential impact of secondhand smoke should be emphasized in occupational health programs at NASA, however. The genetic basis for individual radiation sensitivity is an active research area, although there is no consensus on whether or how to use such information at this time. Other nongenetic factors besides tobacco usage that could modify cancer risks from space radiation are: the age of first pregnancy for breast cancer risks, and skin pigment and history of ultraviolet exposures for skin cancer risks. Possible interactions between these factors and space radiation exposures should be considered in future research.

7. Conclusions

Important changes to the calculation of cancer risks from space radiation were proposed in this report. Several of these changes are based on recent reports from international committees on low-LET radiation effects, or reanalysis of older heavy ion data sets with the notable exception of new data on leukemia and liver tumors induced by Fe nuclei.[134] Several reviews[2,3,5] summarize more recent radiobiology findings on the qualitative and quantitative differences between space radiation and terrestrial low-LET radiation. However, very few comprehensive data sets related to radiation quality or dose-rate modifiers from space radiation have been reported in recent years, although many new studies are in progress. Uncertainties, described as the ratio of the upper 95% CL to the point projection, were slightly improved from our earlier estimates, with improvements partially negated by higher assessments of LSS dosimetry errors in recent reports compared to the earlier NCRP assessment.[15] GCR uncertainties estimates at solar minimum were about 3.6 fold in our revised assessment. In an alternative model that relies on more stringent track structure constraints on QFs, uncertainties are estimated as 2.8 fold. The goal of the NASA Space Radiation Program (SRP) is to achieve less than a 50% error for risk projections for a Mars mission, which is estimated to be the necessary tolerance level because of the higher radiation risks associated with Mars exploration. The underlying scaling approach to the LSS and other human radio-epidemiology data used to estimate space radiation risks has an inherent uncertainty of about 2-fold, which is a severe limitation to the current approach to space radiation risk estimates. Thus, the current approach will need to be replaced in future to achieve the SRP goal for a Mars mission.

Changes recommended, based on the available new information, include:

- Revisions to low-LET risk coefficients to scale space radiation cancer risks, based largely on the UNSCEAR[17] fits to the most recent LSS incidence data.
- Use of incidence-based risk transfer from the LSS to an average U.S. population as recommended by the BEIR VII report.
- Development of an alternative risk calculation for never-smokers that reduces radiation risks for lung, esophagus, stomach, oral cavity, and bladder cancers compared to calculations for the average U.S. population.
- Revisions to PDFs for uncertainties from low-LET radiation, including a revised PDF for the solid-cancer-risk DDREF with a point estimate of DDREF=1.75 compared to the NCRP value of 2 and BEIR VII recommendation of 1.5.
- Development of a track-structure-based model of radiation QFs and an alternative risk cross-section approach, which rely on both E and Z and not LET alone.
- Recommendation of a lower QF for leukemia risk compared to solid cancer risks.
- Revisions to uncertainty assessment for space physics and radiation QFs.
- Use of probabilistic models of SPE size, frequency, and spectral parameters for mission design for a given set of mission parameters (solar cycle, mission length, and shielding).

The RERF in Hiroshima, Japan has made important updates to the LSS data within the last decade, including longer follow-up time and implementation of the DS02 dosimetry system.[96] The BEIR VII, UNSCEAR, and RERF[92] reported on models of incidence or mortality rates for these data sets. The BEIR VII report[16] ignored the age at exposure dependence in EAR and ERR functions above age 30 y, while arguing that the effects were small or the data lacked

significant power to detect this effect. The UNSCEAR report[27] used more general functions of age as well as age at exposure dependences of ERR and EAR functions to describe temporal effects, and also used a Bayesian model of dosimetry errors. UNSCEAR showed that its approach provided improved fits to the LSS incidence data in comparison to the mathematical functions used in the BEIR VII report. Because the UNSCEAR report did not consider several tissues with smaller rates that may be of interest for future attributable risk calculations for ISS crew and exploration planning, we used the RERF model[92] for these tissues (esophagus, oral cavity, ovary, and uterus) and adjusted the remainder calculation accordingly. we used the BEIR VII recommended rates from meta-analysis of several populations, including the LSS data, for radiation risks of breast and thyroid cancer.

The most significant change compared to the NCRP model[6] that was recommended in this report is the use of incidence rates from the LSS to project mortality risks for astronauts. When using incidence-based transfer, cancer rates from the LSS are transferred to the current U.S. population and then converted to mortality risks using ratios of mortality-to-incidence in the U.S. for each tissue site. Mortality-based risk transfer was shown to lead to a much larger decrease in risk with increasing age at exposure compared to incidence-based risk transfer, while yielding similar results around ages 40 to 45 y. We prefer incidence-based risk transfer because these rates are more stable with time compared to mortality rates. Mortality rates have changed appreciably over time since 1945, and are likely to continue to change in future. We recommend that Bayesian or other uncertainty analysis methods be used to fit the LSS incidence and mortality data simultaneously to improve the ERR and EAR functions used in assessments. Tissue-specific estimates also are needed for attributable risk calculations, which will be described in a future report.

Tissue-specific incidence calculations offer improved representation of cancer risks from SPE exposures. In the past, Effective dose calculations were made by averaging organ dose equivalents using tissue weights, w_T, recommended by the ICRP that are age and gender averaged. In the recommended approach, Effective doses do not enter into risk calculations and instead tissue-specific organ dose equivalents are used. For operational radiation protection purposes, Effective doses are useful summary variables, and we recommended the use of gender-specific tissue weights for an average population of ages 30 to 60 y representative of NASA crew ages, and alternative weights for never-smokers. The recommended w_T values are important for SPE risk estimates, in which large dose gradients occur, often leading to high skin, thyroid, an gonad dose equivalents. Therefore, an overestimate of SPE fatal cancer risks occurs when calculated using the ICRP-defined Effective dose. In the recommended w_T values, skin dose equivalent is absent and the values for the thyroid and gonad are reduced.

Because astronauts and many other individuals should be considered as healthy workers, including never-smokers (lifetime use of tobacco below 100 cigarettes), we considered a possible variation in risks and dose limits that would occur due to the reference population used for estimates. After adjusting U.S. average cancer rates to remove smoking effects, radiation risks for lung, and other smoking-attributable cancers including esophagus, oral cavity, stomach, and bladder cancer, estimates were made using a mixture model. Overall cancer risks were found to be more than 20% and 30% lower for males and females, respectively, for never-smokers compared to the average U.S. population. We recommended age- and gender-specific dose limits, based on incidence-based risk transfer for never-smokers, that could be used by NASA. This analysis illustrates that gaining knowledge to improve risk transfer models, which entails knowledge of cancer initiation and promotion effects, could significantly reduce uncertainties in risk projections. Larger reductions than were estimated in this report could occur if higher weight is given to multiplicative risk transfer compared to the transfer weights used herein. The effects

of secondhand smoke and post-mission use of tobacco need to be taken into account when considering distinct radiation limits based on never-smoker risk estimates.

A large number of radiobiology experiments show that biological effects depend on both particle charge number and velocity (or kinetic energy) and not on LET alone. Theoretically based track structure models have for many years predicted this effect. In this report, we developed a simple approach to take into account track structure effects using the improved physical descriptor of Z^{*2}/β^2 and breaking risk calculations into distinct response models for light ($Z \leq 4$) and heavy ($Z>4$) charged nuclei. Finer groupings into individual charge spectra can be made in future as more data become available. The revised approach to QFs described here corrects an important shortcoming in the ICRP definition of QF. Deficiencies in the ICRP model included that: the LET value of the maximum Q was independent of Z, and the slope of the Q function with varying *E* is incorrect both on the ascending and the descending side of a peak value. The resulting NASA model evaluates risks using particle spectra dependent on Z^{*2}/β^2 for light and heavy nuclei groups, and the total absorbed dose at sensitive tissue sites. We recommended QFs for leukemia risks with much smaller values than for solid cancer risks, based on limited but important data from human, animal, and cellular studies. Although the revised calculations of Effective doses differ by about 10% to 30% from the ICRP-recommended QFs for varying shielding thicknesses, these calculations lead to distinct conclusions on the effectiveness of radiation shielding and improved method to assess uncertainties and target critical experiments to further reduced uncertainties.

The ICRP QF is not informed by existing radiobiology data for HZE nuclei. Uncertainty analysis is improved in the revised approach as the underlying QF parameters are more readily related to results from radiobiology experiments than to an LET-based approach such as the ICRP model. An alternative uncertainty assessment was described that assumes that the energy where the maximum QF occurs for each Z is highly constrained. Existing experimental data for Fe nuclei were used to estimate the most likely value and its standard deviation, while the underlying track structure model was used to predict the position for other nuclei with lower Z. The alternative uncertainty assessment led to a 2.8-fold uncertainty for GCR behind 20-g/cm^2 aluminum shielding compared to a 3.6-fold uncertainty for the analysis without this constraint. These results suggest research strategies to improve parameter uncertainties with well-defined particle choices can be made. Tissue-specific estimates of the parameters Σ_0 and κ, using validated experimental models such as transgenic tumor models of human cancers, and a human cell culture model of cancer processes would be optimal in estimating these parameters. Such data would narrow uncertainty factors substantially from current estimates. Alternative uncertainty assessment approaches such as Bayesian methods should be used in the design and analysis of such experiments.

Our revised approach allows for REIC and REID estimates in terms of track-structure-dependent risk cross sections. Risk cross sections, which have been suggested by several biophysical models of heavy ion effects, are useful for considering the extrapolation of radiobiology data to low doses. The changes recommended replace LET with Z^{*2}/β^2 for different charge groups, but do not lead to any inconsistencies with current space dosimetry approaches, which scale transport code prediction or organ exposure to crew dosimeters and area monitors. However, the recommended approach places more emphasis on measurements of Z and E spectra, which can be estimated using CR-39 plastic track detectors worn by crew, and area detectors such as particle hodoscopes that resolve charge and energy. These methods can also be used to validate the accuracy of radiation transport code predictions as has been described in the past.[73]

The uncertainties to cancer risk projections can be broken down into the low-LET risk coefficients, space physics, and radiation QF uncertainties. This breakdown assumes that other uncertainties are smaller and thus ignored. There was an increased estimate of the LSS dosimetry errors in recent reports compared to the NCRP description in 1997.[15] Space physics uncertainties continue to be a minor component of the overall uncertainty. For very thick shielding there is a need for continued analysis of particle production processes that produce largely low-LET radiation (eg, mesons, electrons, and photons) that are less well studied by space transport codes than are protons, neutrons, and heavy nuclei. QFs with values below unity may be appropriate at sufficiently high energy for electrons and photons, and should be considered in uncertainty assessments. There are uncertainties related to estimating the fraction of the U.S. population that are current or former smokers, and the types of cancers attributable to tobacco usage and related relative risk factors. Models of these uncertainties should be the focus of future work.

DDREF values are based on subjective assessment of dose and dose-rate responses across available data sets (human epidemiology, animal studies, and cell culture studies). The ICRP[117] and NCRP[6] recommend DDREF values of 2. However, the recent BEIR VII report recommended a DDREF of 1.5. The impact of a wide range of DDREF values can be evaluated through error assessment methods for uncertainty assessments. We used a PDF for the DDREF that was similar to the NIH Working Group analysis[93] with a median value of DDREF=1.75. This DDREF is at the high end of estimates based on human data for solid cancer risks, and near the lower values found for mouse tumor induction studies for solid cancers.

Uncertainties not addressed are the “unknown” uncertainties discussed by the NCRP, and uncertainty factors related to the distinct time after exposure dependence of cancer risks with radiation quality. There is very little information available to understand how an earlier time of appearance of tumors would impact risk assessments. Uncertainties due to deviation from linearity at low doses of heavy ions were explored with calculations motivated by nontargeted effects.NTEs could increase uncertainties by more than 2-fold for HZE nuclei, and may also depend on mission length. NTEs are a potential “game-changer” for NASA because they may impact radiation protection paradigms with regard to mission length and shielding. Research with chronic exposures at low doses in appropriate models is needed to better understand the importance of NTE in cancer risks. No recommendation to use NTEs for mission requirements is made at this time; however, NTEs should be considered when deciding on research emphasis.

8. References

[1]National Academy of Sciences Space Science Board, Report of the Task Group on the Biological Effects of Space Radiation. *Radiation Hazards to Crews on Interplanetary Mission*. Washington DC: National Academy of Sciences; 1996.

[2]Cucinotta FA, Durante M. Cancer risk from exposure to galactic cosmic rays: implications for space exploration by human beings. *The Lancet Onc.* 2006;7:431-435.

[3]Durante M, Cucinotta FA. Heavy ion carcinogenesis and human space exploration *Nat Rev Cancer*. 2008;8:465-472.

[4]Schimmerling W, Wilson JW, Cucinotta FA, Kim MH. Requirements for simulating space radiations with particle accelerators. In: Fujitaka K, Majima H, Ando K, Yasuda H, Susuki M, eds. *Risk Evaluation of Cosmic-ray Exposure in Long-Term Manned Space Mission*. Tokyo: Kodansha Scientific Ltd.; 1999:1-16.

[5]*Information Needed to Make Radiation Protection Recommendations for Space Missions Beyond Low-Earth Orbit*. Bethesda, Md: National Council on Radiation Protection and Measurements; 2006. NCRP Report No. 153.

[6]NCRP*, Recommendations of Dose Limits for Low Earth Orbit*. Bethesda, Md: National Council on Radiation Protection and Measurements; 2000. NCRP Report No. 132.

[7]Cucinotta FA, Manuel F, Jones J, et al. Space radiation and cataracts in astronauts. *Radiat Res*. December 2001;156:460-466.

[8]Chylack LT, Peterson LE, Feiveson A, et al. NASCA Report 1: Cross-sectional study of relationship of exposure to space radiation and risk of lens opacity. *Radiat Res.* 2009;172:10-20.

[9]Preston DL, Shimizu Y, Pierce DA, Suyumac A, Mabuchi K. Studies of mortality of Atomic bomb survivors. Report 13: Solid cancer and noncancer disease mortality: 1950-1997. *Radiat Res.* 2003;160:381-407.

[10]Little MP, Hoel DG, Molitor J, Boice JD, Wakeford R, Muirhead CR. New models for evaluation of radiation-induced lifetime cancer risk and its uncertainty employed in the UNSCEAR 2006 report. *Radiat Res.* 2008;169:660-676.

[11]Yang VV, Ainsworth EJ. Late effects of heavy charged particles on the fine structure of the mouse coronary artery. *Radiat Res.* 1982;91:135-144.

[12]Cucinotta FA, Schimmerling W, Wilson JW, et al. Space radiation cancer risks and uncertainties for Mars missions. *Radiat Res.* 2001;156:682-688.

[13]Cucinotta FA, Schimmerling W, Wilson JW, Peterson LE, and Saganti PB. Uncertainties In estimates of the risks of late effects from space radiation. *Adv Space Res*. 2004,34:1383-1389.

[14]Cucinotta FA, Kim MY, Ren L. Evaluating shielding effectiveness for reducing space radiation cancer risks. *Radiat Meas.* 2006;41:1173-1185.

[15]NCRP. *Uncertainties in Fatal Cancer Risk Estimates Used in Radiation Protection*. Bethesda, Md: National Council on Radiation Protection and Measurements; 1997. NCRP Report No. 126.

[16]National Academy of Sciences Committee on the Biological Effects of Radiation. *Health Risks From Exposure to Low Levels of Ionizing Radiation (BEIR VII)*. Washington DC: National Academy of Sciences Press: 2006.

[17]United Nations Scientific Committee on the Effects of Atomic Radiation. *Sources and Effects of Ionizing Radiation. UNSCEAR 2006 Report to the General Assembly, with Scientific Annexes.* New York, NY: United Nations; 2008.

[18]Schimmerling W. Accepting space radiation risks. *Radiat Env Biophys.* 2010;49:325-329.

[19]Vaeth M, Pierce DA. Calculating excess lifetime risk in relative risk models. *Environ Health Per.* 1990;87:83-94.

[20]Peterson LE, Cucinotta FA. Monte Carlo mixture model of lifetime cancer incidence risks for radiation on shuttle and the International Space Station. *Mutat Res.* 1999;430:327-335.

[21]NCRP. *Potential Impact of Individual Genetic Susceptibility and Previous Radiation Exposure on Radiation Risk for Astronauts*. Bethesda MD. National Council on Radiation Protection and Measurements; 2011. Report No. 167.

[22] George KA, Elliott T, Kawata T, Pluth JM, Cucinotta FA. Biological effectiveness of low doses of γ-rays and iron nuclei for induction of chromosome aberrations in normal and repair deficient cell lines. *Radiat. Res.* 2009: 171: 752-763 2009

[23]Barcellos-Hoff MH, Park C, Wright EG. Radiation and the microenvironment – tumorigenesis and therapy. *Nat Rev Cancer*. 2005;5:867-875.

[24]Cucinotta FA, Chappell LJ, Non-targeted effects and the dose response for heavy ion tumor formation. *Mutat Res.* 2010;687:49-53.

[25]NCRP. *Operational radiation protection in low Earth orbit*. Bethesda, Md: National Council on Radiation Protection and Measurements; 2003. NCRP Report No. 142.

[26]ICRP. *1990 Recommendations of the International Commission on Radiological Protection*. Oxford: Pergamon Press; 1990. ICRP Publication 60.

[27]Cucinotta FA, Hu S, Schwadron NA, Townsend LW, Kim MY. Space radiation risk limits and Earth-moon-Mars environmental models. Available at: http://www.agu.org/pubs/crossref/2010/2010SW000572.shtml. Accessed July 18, 2011.

[28]Badhwar GD, Cucinotta FA. A comparison of depth dependence of dose and linear energy transfer spectra in aluminum and polyethylene. *Radiat Res.* 2000;153:1-8.

[29]Wilson JW, Nealy JE, Atwell W, Cucinotta FA, Shinn JL, Townsend LW. *Improved Model for solar Cosmic Ray Exposures in Manned Earth Orbital Flights*. Houston, Tx: NASA Johnson Space Center; 1990. NASA TP-1990-2987.

[30]Cucinotta FA, Kim MH, Willingham V, George KA. Physical and biological organ dosimetry analysis for International Space Station Astronauts. *Radiat Res.* 2008; 170: 127–138.

[31]ICRP, *Relative Biological Effectiveness (RBE), Quality Factor (Q), and Radiation Weighting Factor (w_R).* ICRP Publication 92. International Commission on Radiation Protection, Pergamon, 2003.

[32]Rai SN, Kreqski D. Uncertainty and variability analysis in multiplicative risk models. *Risk Analysis*. 1998;18:37-45.

[33]Wilson JW, Townsend LW, Schimmerling W, et al. *Transport Methods and Interactions for Space Radiations*. Springfield, Va: National Technical Information Service, 1991. NASA RP-1257.

[34]Cucinotta FA, Wilson JW, Williams JR, Dicello JF. Analysis of Mir-18 results for physical and biological dosimetry: radiation shielding effectiveness in LEO. *Radiat Meas.* 2000;132:181-191.

[35]Ginzburg VL. The origin of cosmic radiation. *Progr Elem Particle Cosmic Ray Phys.* 1958;4:339.

[36]Colgate SA, Grasberger WH, White RH. The dynamics of a supernova explosion. *J Phys Soc Japan*. 1963;17(suppl A-III):157.

[37]Meyer P. Cosmic rays in the galaxy. *Ann Rev Astron Astrophys*. 1969;7:1.

[38]Simpson JA. Elemental and isotropic composition of the galactic cosmic rays. In: Jackson J, Gove H, Schwitters R, eds. *Ann Rev Nucl Particle Sci*. 1983;33:323-381.

[39]Cucinotta FA, Wilson JW, Saganti P, et al. Isotopic dependence of GCR fluence behind shielding. *Radiat Meas.* 2006;41:1235-1249.

[40]Webber WR, Southoul A, Ferrando P, Gupta M. The source charge and isotopic abundances of cosmic rays with Z = 9–16: a study using new fragmentation cross-sections. *Astrophys J.* 1990;348, 611-620.

[41]Fields BD, Olive KA, Schramm DN. Cosmic ray models for early galactic lithium, beryllium and boron production. *Astrophys J*. 1994;435:185-202.

[42]Wiedenback ME, Greiner DE. High-resolution observations of the isotopic composition of carbon and silicon in the galactic cosmic rays. *Astrophys J*. 1981;247:L119-L122.

[43]Wiedenback ME. The isotopic composition on cosmic ray chlorine. Paper presented at: 19th International Cosmic Ray Conference; August 11-23, 1985; La Jolla, Calif.

[44]Webber WR, Kish JC, Schrier DA. Cosmic ray isotope measurements with a new Cerenkov total energy telescope. Paper presented at: 19th International Cosmic Ray Conference; August 11-23, 1985; La Jolla, Calif.

[45]Hesse A, Acarya BS, Heinbach U, et al. The isotopic composition of silicon and iron in the cosmic radiation as measured by the ALICE experiment. *Proc 22nd Internat Cosmic Ray Conf (Dublin, Ireland)*. 1991;1:596-599 (1991).

[46]Lukasiak A, Ferrando P, McDonald FB, Webber WR. Cosmic ray composition of $6<Z<8$ nuclei in the energy range 50-150 MeV/n by the Voyager spacecraft during the solar minimum and maximum periods. Paper presented at: 23rd International Cosmic Ray Conference; July 19-30, 1993; La Jolla, Calif.

[47]Lukasiak A, McDonald FB, Webber WR, Ferrando P. Voyager measurements of the isotopic composition of Sc, Ti, V, Cr, Mn, and Fe nuclei. Iucci N, Lamanna, eds. *Proceedings of the Twenty-fourth International Cosmic Ray Conference*. Vol. 2. Rome: International Union of Pure and Applied Physics; 1995:576-579.

[48]Labrado AW, et al. Extended energy spectrum measurements of elements with the cosmic ray isotope spectrometer (CRIS). *Proc 28th Int Cosmic Ray Conf (Tsukuba, Japan)*. 2003:1773-1776.

[49]Zeitlin C, Cleghorn T, Cucinotta F, et al. Overview of the Martian radiation environment experiment. *Adv Space Res.* 2004;33:2204-2210.

[50]Badhwar GD, O'Neill PM. An improved model of GCR for space exploration missions. *Nucl Tracks Radiat Meas.* 1992;20:403-410.

[51]O'Neill P. Badhwar–O'Neill. Galactic cosmic ray model update based on advanced composition explorer (ACE) energy spectra from 1997 to present. *Adv Space Res.* 2006;37:1727-1733.

[52]Parker EN. The passage of energetic charged particles through interplanetary space. *Planet Space Sci.* 1965:13:9-49.

[53]Bobcock HW. The topology of the Sun's magnetic field and the 22-year cycle. *Astrophys J.* 1961;133(2):572-587[54] Badhwar, G. B.; Cucinotta, F.A., and O'Neill, P. M.: An Analysis of Interplanetary Space Radiation Exposure for Various Solar Cycles. *Radiat Res.* 1994;138: 201-208.

[55]Kim MY, De Angelis G, Cucinotta FA. Probabilistic risk assessment for astronauts on deep space missions. *Acta Astron.* 2011;68: 747-759.

[56]Castagnoli GC, Cane D, Taricco C, Bhandari N. GCR flux decline during the last three centuries: extraterrestrial and terrestrial evidences. In: Kajita, T., Asaoka, Y., Kawachi, A., Matsubara, Y., Sasaki, M. (Eds.), GCR Flux Decline during the last Three Centuries: Extraterrestrial and Terrestrial Evidences. Universal Academy Press, Inc., 2003; 4045–4048.

[57]Valtonen V, Nurmi P, Zheng JQ, et al. Natural transfer of viable microbes in space from planets in extra-solar systems to a planet in our solar system and vice versa. *Astrophys J.* 2009;690:210-215.

[58]Forbush SE. On the effects in cosmic-ray intensity observed during the recent magnetic storm. *Phys Rev.* 1937;51:1108-1109.

[59]Shea M, Smart DF. A summary of major proton events. *Solar Phys.* 1990;127:297-320.

[60]Kim MY, Hayat MJ, Feiveson AH, Cucinotta FA. Prediction of frequency and exposure level of solar particle events. *Health Phys.* 2009;97:68-81.

[61]McCracken KG, Dreschhoff G, Zeller EJ, Smart DF, Shea MA. 2001. Solar cosmic ray events for the period 1561-1994. 1. Identification in polar ice, 1561–1950. *J Geophys Res.* 2001;106(A10):21585-21598.

[62]Goswami JN, McGuire RE, Reedy RC, Lal D, Jha R. Solar flare protons and alpha particles during the last three solar cycles. *J Geophys Res.* 1988;93:7195-7205.

[63]National Geophysical Data Center (NGDC), National Oceanic and Atmospheric Administration (NOAA): GOES Space Environment Monitor (SEM) data archive directories. Available at: http://goes.ngdc.noaa.gov/data/. Accessed July 18, 2011.

[64]Feynman J, Spitale G, Wang J, and S. Gabriel. Interplanetary proton fluence model: JPL 1991. *J. Geophys Res*. 1993, **98**: 281-294.

[65]King JH. Proton fluences for 1977-1983 space missions. *J Spacecraft*. 1974;11:401-408.

[66] Wilson JW, Cucinotta FA, Kim M, Shinn JL, Jones TD, and Chang CK. Biological response to SPE exposure. *Radiat Meas.* 1999;30:361-370.

[67]Band D, et al. Baste Observations of gamma-rays burst spectra. I. Spectral diversity. *Astrophys J.* 1993;413:281-292.

[68]Tylka AJ, Dietrich A. New comprehensive analysis of proton spectra in ground-level enhanced (GLE) solar particle events. The Proceedings of the 31st International Cosmic Ray Conference, Lodz, Poland, July 7-15, 1999.

[69]Wilson JW, Kim MH, Schimmerling W, et al. Issues in space radiation protection. *Health Phys.* 1995;68:50-58.

[70]Cucinotta FA, Plante I, Ponomarev AL, Kim MY. Nuclear interactions in heavy ion transport and event-based risk models. *Radiat Prot Dosim*. Doi: February 2011;143(2-4):384-390.

[71]Tripathi RK, Cucinotta FA, and Wilson JW. Accurate universal parameterization of absorption cross sections. *Nuclear Instrum Meth Phys Res. 1996;* B117:347-349.

[72]Cucinotta FA, Kim MY, Schneider SI, Hassler DM. Description of light ion production cross sections and fluxes on the Mars surface using the QMSFRG model. *Radiat Environ Biophys.* 2007;46:101-106.

[73]Cucinotta FA, Wilson JW, Katz R, Atwell W, and Badhwar G D. Track structure and radiation transport models for space radiobiology studies. *Adv Space Res.* 1995;18:183-194.

[74]Benton EV. Summary of radiation dosimetry results on the U.S. and Soviet manned spacecraft. *Adv Space Res.* 1986;6:315-328.

[75]Zeitlin CJ, Sihver L, La Tessa C. Comparisons of fragmentation spectra using 1 GeV/amu ^{56}Fe data and the PHITS model. *Radiat Meas.* 2008;43:1242-1253.

[76]Wilson JW, Cucinotta FA, Tai H, Shinn JL, Chun SY, Sihver L. Transport properties of light ions in matter. *Adv Space Res.* 1998;21:1763-1771.

[77]Walker SA, Tweed J, Wilson JW. Validation of the HZETRN code for laboratory exposures with 1 GeV/u iron with several targets. *Adv Space Res*. 2005;35:202-207.

[78]Townsend LW, Miller TM, Gabriel TA. Modifications to the HETC radiation transport code for space radiation shielding applications: A status report. Paper presented at: 12th Biennial ANS Radiation Protection and Shielding Division Topical Meeting; April 14-18, 2002; Santa Fe, NM.

[79]Ballarini F, Battistoni G, Brugger M, et al. The physics of the FLUKA code: recent developments. *Adv Space Res.* 2007;40:1339-1349.

[80]Niita K, Sato T, Iwase H, Nose H, Nakashima H, Sihver L. PHITS – a particle and heavy ion transport code system. *Radiat Meas*. 2006;41:1080-1090.

[81]Badhwar GD, Atwell W, Badavi FF, Yang TC, Cleghorn TF. Space radiation dose in a human phantom. *Radiat Res.* 2002;157:76-91.

[82]Yasuda H, Badhwar GD, Komiyama T, Fujitaka K. Effective dose equivalent on the ninth shuttle-Mir mission (STS 91). *Radiat Res.* 2000;154:705-713.

[83]Reitz G, et al. Astronaut's organ doses inferred from measurements in a human phantom outside the international space station. *Radiat Res.* 2009;171:225-235.

[84]Badhwar GD, Patel JU, Cucinotta FA, Wilson JW. Measurements of secondary particle energy spectrum in the space shuttle. *Radiat Meas.* 1995;24:129-138.

[85]Shinn JL, Badhwar GD, Xapsos MA, Cucinotta FA, Wilson JW. An analysis of energy deposition in a tissue equivalent proportional counter onboard the space shuttle. *Radiat. Meas*. 1999; 30:19-28.

[86]Nikjoo H, Khvostunov IK, Cucinotta FA. The response of (TEPC) proportional counters to heavy ions. *Radiat Res.* 2002;157:435-445.

[87]Wilson JW, et al. Time serial analysis of the induced LEO environment within the ISS 6A. *Adv Space Res*. 2007;40:1562-1570.

[88]Kim MY, George KA, Cucinotta FA. Evaluation of skin cancer risks from lunar and Mars missions. *Adv Space Res.* 2006;37:1798-1803.

[89]Saganti PB, Cucinotta FA, Wilson JW, Simonsen LC, and Zeitlin CJ. Radiation climate map for analyzing risks to astronauts on the Mars surface from galactic cosmic rays. *Space Science Rev.* 2004; 110:143-156.

[90]Kim MY, Cucinotta FA, Wilson JW. A temporal forecast of radiation environments for future space exploration missions. *Radiat Environ Biophys*. 2007;46:95-100.

[91]Ponomarev A, Nounu HN, Hussein HF, Kim MY, Atwell W, Cucinotta FA. *NASA-developed ProE-based Tool for the Ray-tracing of Spacecraft Geometry to Determine Radiation Doses and Particle Fluxes in Habitable Area of Spacecraft and the Human Body*. Houston, Tx: NASA Johnson Space Center; 2007. NASA TP-2007-214770.

[92]Preston DL, Ron E, Tokuoka S, et al. Solid cancer incidence in atomic bomb survivors: 1958-1998. *Radiat Res.* 2007;168:1-64.

[93]NIH. *Report of the NCI-CDC Working Group to Revise the 1985 NIH Radioepidemiological Tables*. Washington, DC: U.S. Department of Health and Human Services, National Institutes of Health, National Cancer Institute; 2003. NIH Publication No. 03-5387.

[94]Little MP. Heterogeneity of variation of relative risk by age at exposure in the Japanese atomic bomb survivors. *Radiat Environ Biophys.* 2010;48:253-262.

[95]Pawel D, Preston D, Pierce D, Cologne J. Improved estimates of cancer site-specific risks for A-bomb survivors. *Radiat Res.* 2008;169:87-98.

[96]Preston DL, Pierce DA, Shimizu Y, et al. Recent changes in atomic bomb survivor dosimetry on cancer mortality risk estimates. *Radiat Res.* 2004;162:377–389.

[97]Jacob P, Ruhm W, Walsh L, Blettner M, Hammer G, Zeeb H. Is cancer risk of radiation workers larger than expected? *Occup Env Med.* 2009;66:789-796.

[98]NCRP. *Guidance on Radiation Received in Space Activities*. Bethesda, Md: National Council on Radiation Protection and Measurements; 1989. NCRP Report No. 98.

[99]SEER, Surveillance, Epidemiology, and End Results: Cancer Statistics Review, 2005. Bethesda, Md: Cancer Surveillance Research Program, National Cancer Institute; 2006.

[100]Kort EJ, Paneeth N, Vande Woude GF. The decline in U.S. cancer mortality in people born since 1925. *Cancer Res.* 2009;69:6500-6505.

[101]Centers for Disease Control (CDC), Compressed Mortality File 1999-2005. CDC WONDER On-line Database, compiled from Compressed Mortality File 1999-2005 Series 20 No. 2K, 2008. Available at: http://wonder.cdc.gov/cmf-icd10.html. Accessed July 18, 2011.

[102]Barcellos-Hoff MH, Ravini SA. Irradiated mammary gland stroma promotes the expression of tumorigenic potential by unirradiated epithelial cells. *Cancer Res*. 2000;60:1254-1260.

[103]Thun MJ, Hannan LM, Adams-Campbell LL, et al. Lung cancer occurrence in never-smokers: an analysis of 13 cohorts and 22 cancer registry studies. *PLoS Med.* 2008;5:1357-1371.

[104]Furukawa K, Preston DL, Lonn S, et al. Radiation and smoking effects on lung cancer incidence among atomic bomb survivors. *Radiat Res.* 2010;174:72-82.

[105]CDC-MMWR. *Morbidity Weekly Report. Centers of Disease Control*. 2008;57(45):1226-1228.

[106]Terry PD, Rohan TE. Cigarette smoking and the risk of breast cancer in women: a review of the literature. *Cancer Epidem Biomark Prev.* 2002;11:953-971.

[107]Subramanian J, Gavindan R. Molecular genetics of lung cancer in people who never have smoked. *Lancet Oncol.* 2008;9:676-682.

[108]Land CE, Shimosatao Y, Saccomanno G, et. al. Radiation-associated lung cancer: a comparison of the histology of lung cancers in uranium miners and survivors of the atomic bombings of Hiroshima and Nagasaki. *Radiat Res.* 1993;134:234-243.

[109]Gilbert ES, Stovall M, Gospodarowicz M, et al. Lung cancer after treatment for Hodgkin's disease: focus on radiation effects. *Radiat Res.* 2003;159:161-173.

[110]National Academy of Sciences, National Research Council, Committee on Health Risks of Exposure to Radon. *Health Effects of Exposure to Radon (BEIR VI)*. Washington, DC: National Academy Press: 1999.

[111]Preston DL, Krestnina LY, Sokolnikov ME, et al. How much can we say about site-specific cancer radiation risks? *Radiat Res*. December 2010;174(6):816-824.

[112]Suzuki, MS, Nomura T, Ejima Y, et al. Experimental derivation of relative biological effectiveness of A-bomb neutrons in Hiroshima and Nagasaki and Implications for risk assessment. *Radiat Res*. 2008;170: 101-117.

[113]EPA. "EPA Radiogenic Cancer Risk Models and Projections for the U.S. Population". U.S. Environmental Protection Agency, Washington DC. (Draft report), 2008.

[114]Kellerer AJ, Walsh L. Solid cancer risk coefficient for fast neutrons in terms of effective dose. *Radiat Res*. 2002;158:61-68.

[115]Goodhead DT, Thacker J, Cox R. Effectiveness of 0.3 keV carbon ultrasoft x-rays for the inactivation and mutation of cultured mammalian cells. *Int. J. Radiat. Biol.* 1979; 36: 101–114.

[116]Hill MA. The variation in biological effectiveness of X-rays and gamma rays with energy. *Radiat. Prot. Dosim.* 2004;112:471-481.

[117]ICRP. *The 2007 Recommendations of the International Commission on Radiological Protection. International Commission on Radiological Protection.* Annals of the ICRP 37, Nos. 2-4; 2007. ICRP Publication 103.

[118]Loucas BD, Eberle R, Bailey SM, Cornforth MN. Influence of dose rate on the induction of simple and complex chromosome exchanges by gamma rays. *Radiat Res.* 2004;162:339-349.

[119]Cornforth M, Bailey SM, Goodwin EH. Dose responses for chromosome aberrations produced in noncycling primary human fibroblasts by alpha particles, and by gamma rays delivered at sublimiting low dose rates. *Radiat Res.* 2002; 158: 45-53.

[120]NCRP, *Influence of Dose and Its Distribution in Time on Dose-Response Relationships for Low LET Radiation*. Bethesda, Md: National Council on Radiation Protection and Measurements; 1980. NCRP Report No. 64.

[121]Storer JB, Mitchell TJ, Fry RJ. Extrapolation of the relative risk of radiogenic neoplasms across mouse strains and to man. *Radiat Res.* 1988;113:331-353.

[122]Social Security Administration. A stochastic model of the long-range financial status of the OASDI program actuarial study no. 117. Washington, DC: Social Security Administration, Office of the Chief Actuary; September 2004. SSA Pub. No. 11-11555.

[123]Yamane GK. Cancer incidence in the U.S. Air Force: 1989-2002. *Aviat Space Env Med*. 2006;77:789-794.

[124]Bissell M, et al. *Modeling Human Risk: Cell & Molecular Biology in Context*. NASA and LBNL Publication 40278; Oak Ridge, TN. 1997.

[125]Fry RJM, Storer JB. External radiation carcinogenesis. In: Lett JT, ed. *Advances in Radiation Biology*. Vol. 13. New York, NY: Academic Press; 1987:31-90.

[126]Boice JD Jr. Leukemia risks in thorotrast patients. *Radiat Res.* 1993;136:301-302.

[127]Grogan HA, Sinclair WK, Voilleque PG. Risks of fatal cancer from inhalation of ^{239,240}plutonium by humans: a combined four-method approach with uncertainty evaluation. *Health Phys*. 2001;80:447-461.

[128] Burns F, Yin Y, Garte SJ, Hosselet S. Estimation of risk based on multiple events in radiation carcinogenesis of rat skin. *Adv Space Res.* 1994; 14: 507–519.

[129]Burns FJ, Jin Y, Koenig KL et al. The low carcinogenicity of electron radiation relative to argon ions in rat skin. *Radiat Res.* 1993; 135: 178-188.

[130]Fry RJM, Powers-Risius P, Alpen EL, Ainsworth EJ. High LET radiation carcinogenesis. *Radiat Res.* 1985;104:S188-S195.

[131]Alpen EL, Powers-Risius P, Curtis SB, DeGuzman R. Tumorigenic potential of high-Z, high-LET charged particle radiations. *Radiat Res.* 1993;88:132-143.

[132]Alpen EL, Powers-Risius P, Curtis SB, DeGuzman R, Fry RJM. Fluence-based relative biological effectiveness for charged particle carcinogenesis in mouse Harderian gland. *Adv Space Res.* 1994;14:573-581.

[133]Dicello JF, et al. *In vivo* mammary tumorigenesis in the Sprague-Dawley rat and microdosimetric correlates. *Phys Med Biol.* 2004;49:3817-3830.

[134]Weil MM, Bedford JS, Bielefeldt-Ohmann H, Ray AF, Gernik PC, Ehrhart EJ, Falgren CM, Hailu F, Battaglia CLR, Charles C, Callan MA, Ullrich RLet al. Incidence of acute myeloid leukemia and hepatocellular carcinoma in mice irradiated with 1 GeV/nucleon ^{56}Fe ions. *Radiat Res.* 2009;172:213-219.

[135]Ainsworth EJ. Early and late mammalian responses to heavy charged particles. *Adv Space Res.* 1986;6:153-162.

[136]Burns FJ, Hosselet S, Jin Y, Dudas G, Garte SJ. Progression and multiple events in radiation carcinogenesis of rat skin. *J Radiat Res.* 1991*;* **32**, S202–S216.

[137]Burns F, Zhao P, Xu G, Roy N, Loomis C. Fibroma induction in rat skin following single or multiple doses of 1.0 GeV/nucleon ^{56}Fe ions from the Brookhaven alternating gradient synchrotron. *Physica Medica*. 2001;XVII:194-195.

[138]Mole RH, Papworth, DG Corp MJ. The dose-response for X-ray induction of myeloid-leukemia in male CBA/H mice. *Br. J. Cancer* 1983; 47: 285–291.

[139]Ullrich RL Preston RJ. Myeloid leukemia in male RFM mice following irradiation with fission spectrum neutrons or gamma rays. *Radiat Res.* 1987;109:165–170.

[140]Griffiths SD, Marsden SJ, Wright EG, Greaves MF, Goodhead DT. Lethality and mutagenesis of B lymphocyte progenitor cells following exposures to α-particles and X-rays. *Int J Radiat Biol*. 1994;66:197-205.

[141]Peng, Y, Brown N, Finnon, F et al., Radiation leukemogenesis in mice: Loss of *PU.1* on chromosome 2 in CBA and C57BL/6 mice after irradiation with 1 GeV/nucleon 56Fe ions, X rays or γ rays. Part I. experimental observations. *Radiat Res.* 2009; 171:474–483.

[142]Edwards AA. RBE of space radiations and the implications for space travel. *Physica Medica*. 2001;XVII(suppl 1):147-152.

[143]Fry RJM, Garcia AG, Allen KH, et al. The effect of pituitary isografts on radiation carcinogenesis in the mammary and Harderian glands of mice. In: *Biological Effects of Low Level Radiation Pertinent to Protection of Man and His Environment*. Vol. I. Vienna, Austria: International Atomic Energy Agency; 1976:213-227.

[144]George KA, Cucinotta FA. The influence of shielding on the biological effectiveness of accelerated particles for the induction of chromosome damage. *Adv Space Res.* 2007;39:1076-1081.

[145]George K, Durante M, Willingham V, Wu H, Yang T, Cucinotta FA. Biological effectiveness of accelerated particles for the induction of chromosome damage measured in metaphase and interphase human lymphocytes. *Radiat Res.* 2003;160:425-435.

[146]Yang TC, Craise LM, Mei M, Tobias CA. Neoplastic cell transformation by heavy charged particles. *Radiat Res.* 1985;104:S177-S187.

[147]Kiefer J, Stoll U, Schneider E. Mutation induction by heavy Ions. *Adv Space Res*. 1994;14(10):257-265.

[148]Kiefer J, Schmidt P, Koch S. Mutations in mammalian cells induced by heavy charged particles: An indicator for risk Assessment in Space. *Radiat Res.* 2001;156:607-611.

[149]Cucinotta FA, Wilson JW, Shavers MR, Katz R. Effects of track structure and cell inactivation on the calculation of heavy ion mutation rates in mammalian cells. *Int J Radiat Biol.* 1996;69:593-600.

[150]Anderson R, Stevens DL, Goodhead DT. M-FISH analysis shows that complex chromosome aberrations induced by α-particle tracks are cumulative products of localized rearrangements. *Proc Natl Acad Sci USA*. 2002;99:12167-12172.

[151]Durante M, George K, Wu H, Cucinotta FA. Karyotypes of human lymphocytes exposed to high-energy iron ions. *Radiat Res.* 2002;158:581-590.

[152]Durante M, George K, and Cucinotta FA. Chromosomes lacking telomeres are present in the progeny of human lymphocytes exposed to heavy ions. *Radiat. Res.* 2006; 165: 51-58.

[153]Kadhim MA, Macdonald DA, Goodhead DT, Lorimore SA, Marsden SJ, Wright EG. Transmission of chromosomal instability after plutonium a-particle irradiation. *Nature*. 1992;355:738-740.

[154] Watson GE, Lorimore SA, Clutton S, Kadhim M, Wright EG. Chromosomal instability in unirradiated cells induced in vivo by a bystander effect of ionizing radiation. *Cancer Res.* 2000;60:5608-5611.

[155]Ullrich RL, Ponnaiya B. Radiation-induced instability and its relation to radiation carcinogenesis. *Inter J Radiat Biol.* 1998;74:747-754.

[156]Brooks AL, Bao S, Rithidech K, Couch LA, Braby LA. Relative effectiveness of HZE iron-56 particles for the induction of cytogenetic damage *in vivo*. *Radiat Res.* 2001;155:353-359.

[157]Evans HH, Horng M, Ricanati M, Diaz-Insua R, Scwarz JL. Characteristics of genomic instability in clones of TK6 human lymphoblasts surviving exposure to ^{56}Fe ions. *Radiat Res.* 2002;158:687-698.

[158]Sudo H, Garbe J, Stampfer MR, Barcellos-Hoff MH, Kronenberg A. Karyotypic instability and centrosome aberrations in the progeny of finite life-span human mammary epithelial cells exposed to sparsely or densely ionizing radiation. *Radiat Res.* 2008;170:23-32.

[159]Ullrich RL. Tumor induction in BAL/c mice after fractionated neutron or gamma irradiation. *Radiat Res*. 1984;93:506-512.

[160]NCRP. *Relative Biological Effectiveness of Radiations of Different Quality*. Bethesda, Md: National Council on Radiation Protection and Measurements; 1990. NCRP Report No. 104.

[161]Cucinotta FA, Wilson JW. Initiation-promotion model for tumor prevalence from high energy and charge radiation. *Phys Med Biol.* 1994;39:1811-1831.

[162]Katz R, Ackerson B, Homayoonfar M, Scharma SC. Inactivation of cells by heavy ion bombardment. *Radiat Res.* 1971;47:402-425.

[163]Goodhead DT, Nikjoo H. Track structure analysis of ultrasoft X-rays compared to high- and low-LET radiations. *Int J Radiat Biol.* 1989;55:513-529.

[164]Plante I, Cucinotta FA. Ionization and excitation cross sections for the interaction of HZE particles in liquid water and application to Monte-Carlo simulation of radiation tracks. *New J Phys.* 2008;10:125020 doi: 10.1088/1367-2630/10/12/125020.

[165]Butts JJ, Katz R. Theory of RBE for heavy ion bombardment of dry enzymes and viruses. *Radiat Res.* 1967;30:855-871.

[166]Cheung WK, Norbury JW. Stopping powers and cross sections due to two-photon processes in relativistic nucleus-nucleus collisions. Washington DC: NASA Headquarters, 1994. NASA CP 4574.

[167]Kobetich R, Katz R. Energy deposition by electron beams and δ-rays. *Phys Rev.* 1968;170:391-396.

[168]Brandt W, Ritchie HR. Primary processes in the physical stage. In: Cooper RD, Woods R, eds. *Physical Mechanisms in Radiation Biology*. Washington, DC: Technical Information Center, Atomic Energy Commission, U.S. Department of Energy; 1974:20-29.

[169]Cucinotta FA, Nikjoo H, Goodhead DT. Applications of amorphous track models in radiobiology. *Radiat Environ Biophys.* 1999;38:81-92.

[170]Chatterjee A, Maccabee D, Tobias CA. Radial cutoff LET and radial cutoff dose calculations for heavy charged particles in water. *Radiat Res*. 1973;54:479-494.

[171]Kraft G, Kramer M. LET and track structure. In: Lett J, Sinclair WK, eds. *Advances in Radiation Biology*. San Diego, Calif: Academic Press; 1993:1-50.

[172]Cucinotta FA, Nikjoo H, Goodhead DT. Model of the radial distribution of energy imparted in nanometer volumes from HZE particles. *Radiat Res.* 2000;153:459-468.

[173]Goodhead DT, Munson RJ, Thacker J, Cox R. Mutation and inactivation of cultured mammalian cells exposed to beams of accelerated heavy ions. IV. Biophysical interpretation. *Int J Radiat Biol.* 1980;37:135-167.

[174]Katz R RBE, LET, and z/β^{α}. *Health Phys*. 1970;18:175.

[175]Thacker J, Stretch A, Stephens MA. Mutation and inactivation of cultured mammalian cells exposed to beams of accelerated heavy ions. II. Chinese hamster V79 cells. *Int J Radiat Biol.* 1979;38:137-148.

[176]Belli M, Goodhead DT, Ianzini F, Simone G, Tabocchini MA. Direct comparison of biological effectiveness of protons and alpha-particles of the same LET. II. Mutation induction at the HPRT locus in V79 cells. *Int J Radiat Biol*. 1992;61:625-629.

[177]Belli M, Cera F, Cherubini R, et al. Inactivation and mutation induction In V79 cells by low energy protons: re-evaluation of the results at the LNL facility. *Int J Radiat Biol*. 1993;63:331-337.

[178]Schafer M, Schmitz C, Bucker H. DNA double strand breaks induced in *Escherichia Coli* cells by radiations of different quality. *Radiat Prot Dosim.* 1994;52:233-236.

[179]Baltschukat K, Horneck G. Response to accelerated heavy ions of spores of *Bacillus-Subtilis* of different repair capacity. *Radiat Env Biophys.* 1991;30:87-104.

[180]Kranert T, Schneider E, Kiefer J. Mutation induction in V79 Chinese hamster cells by very heavy ions. *Int J Radiat Biol.* 1990;58:975-987.

[181]Cucinotta FA, Wilson JW, Shavers MR, Katz R. *The Calculation of Heavy Ion Inactivation and Mutation Rates in the Track Structure Model*. Houston, Tex: NASA Johnson Space Center; 1997. NASA TP-1997-3630.

[182]Holley WR, Chatterjee A. Clusters of DNA damage induced by ionizing radiation: formation of short DNA fragments. I. Theoretical modeling. *Radiat Res.* 1996;145:188-189.

[183]LaVerne JA. Review: Track effects of heavy ions in liquid water. *Radiat Res*. 2000;153:487-496.

[184]Katz R, Cucinotta FA. RBE vs. dose for low doses of high LET radiation. *Health Phys.* 1991;60:717-719.

[185]Katz R, Zachariah R, Cucinotta FA, Chanxiang Z. Survey of radiosensitivity parameters. *Radiat Res.* 1994;14:356-365.

[186]Goodhead DT. Relationship of radiation track structure to biological effect: a re-interpretation of the parameters of the Katz model. *Nuclear Tracks Radiat Meas.* 1989;116:177-184.

[187]Goodhead DT. Energy deposition stochastics and track structure: What about the target? *Radiat Prot Dosim*. 2006;122:3-15.

[188]Wilson JW, Cucinotta FA, Shinn JL. Cell kinetics and track structure. In: Swenberg CE, et al, eds. *Biological Effects and Physics of Solar and Galactic Cosmic Rays*. New York, NY: Plenum Press, New York; 1993:295-338.

[189]Cucinotta FA, Wilson JW. Initiation-promotion model of tumor prevalence in mice from space radiation exposure. *Radiat Environ Biophys.* 1995;34:145-149.

[190] Morgan WF. Non-targeted and delayed effects of exposure to ionizing radiation: I. Radiation-induced genomic instability and bystander effects in vitro. *Radiat Res.*2003; 159:567-580.

[191]Prise KM, Belyakov OV, Folkard M, Michael BD. Studies on bystander effects in human fibroblasts using a charged particle microbeam. *Int J Radiat Biol.* 1998;74:793-798.

[192]Belyakov OV, et al. Biological effects of unirradiated human tissue by radiation damage up to 1 mm away. *Proc Natl Acad Sci USA*. 2005;102:14203-14208.

[193]Nagasawa H, Little JB. Induction of sister chromatid exchanges by extremely low doses of α-particles. *Cancer Res.* 1992;52:6394-6396.

[194]Lehnert BE, Goodwin EH, Desphande A. Extracellular factors following exposure to α-particles can cause sister chromatid exchanges in normal human cells. *Cancer Res.* 1997;57:2164-2171.

[195]Nagasawa H, Little JB. Bystander effect for chromosomal aberrations induced in wild-type and repair deficient CHO cells by low fluences of alpha particles. *Mutat Res.* 2002;508:121-129.

[196]Miller RC, Marino SA, Brenner DJ, et al. The biological effectiveness of radon-progeny alpha particles. II. Oncogenic transformation as a function of linear energy transfer. *Radiat Res*. 1995;142:54-60.

[197]Brenner DJ, Little JB, Sachs RK. The bystander effect in radiation oncogenesis. II. A quantitative model. *Radiat Res.* 2001;155:402-408.

[198]Katz R, Scharma SC, Homayoonfar M. The structure of particle tracks. In: Attix FH, ed. *Topics in Radiation Dosimetry*, Supplement 1. New York, NY: Academic Press; 1972:317-383.

[199]Hoffman W, Katz R, Chunxiang Z. Lung cancer risk at low doses of α-particles. *Health Phys*. 1986;51:457-468.

[200]Curtis SB, Nealy JE, Wilson JW. Risk cross sections and their application to risk estimation in the galactic cosmic-ray environment. *Radiat Res.* 1995;141:57-65.

[201]NCRP. *Fluence-based Microdosimetric Event-based Methods for Radiation Protection in Space*. Bethesda, Md: National Council on Radiation Protection and Measurements; 2001. NCRP Report No. 137.

[202]Edwards AA. The use of chromosomal aberrations in human lymphocytes for biological dosimetry. Radiat. Res. 1997;148:S39-S44.

[203]Sasaki MS, Takatsuji T, Ejima Y. The F value cannot be ruled out as a chromosomal fingerprint of radiation quality. *Radiat Res.* 1998;150:253-258.

[204]Cox R, Masson WK. Mutation and inactivation of cultured mammalian cells exposed to beams of accelerated heavy Ions. *Int J Radiat Biol.* 1979;36:149-160.

[205]Tsuboi K., Yang TC, Chen DJ. Charged-particle mutagenesis. I. cytoxic and mutagenic effects of high-LET charged iron particles on human skin fibroblasts. *Radiat Res.* 1992;129:171-176.

[206]Kronenberg A. Mutation induction in human lymphoid cells by energetic heavy ions. *Adv Space Res.* 1994;14:339-346.

[207]Yang TC, Craise LM, Mei M, Tobias CA. Neoplastic transformation by high LET radiation: Molecular mechanisms. *Adv Space Res.* 1989;9:131-140.

[208]Miller RC, Marino S., Brenner DJ, et al. The biological effectiveness of radon-progeny alpha particles III. quality factors. *Radiat. Res.*1995;142: 61–69.

[209]Waligorski MP, Sinclair GL, Katz R. Radiosensitivity parameters for neoplastic transformations in C3H10T1/2 cells. *Radiat Res.* 1987;111:424-437.

[210]Barkas H. *Nuclear Research Emulsions.* Vol. 1. New York, NY: Academic Press Inc.; 1963:chap 9.

[211]SEER, Horner MJ, Ries LAG, Krapcho M, Neyman N, Aminou R, Howlader N, Altekruse SF, Feuer EJ, Huang L, Mariotto A, Miller BA, Lewis DR, Eisner MP, Stinchcomb DG, Edwards BK (eds). SEER Cancer Statistics Review, 1975-2006, National Cancer Institute. Bethesda, MD, http://seer.cancer.gov/csr/1975_2006/, based on November 2008 SEER data submission, posted to the SEER web site, 2009

[212]Han, Z, Suzuki H, Suzuki F, et al. Neoplastic transformation of hamster embryo cells by heavy ions. *Adv Space Res*. 1998;22:1725-1732.

[213]Billings MP, Yucker WR, Heckman BR. Body self-shielding data analysis. Huntington Beach, Calif: McDonald Douglas Astronautics Company West; 1973. MDC-G4131.

[214]Smith AE, Ryan PB, Evans JS. The effect of neglecting correlations when propagating uncertainty and estimating the population distribution of risk. *Risk Analysis*. 1992;12:467-474.

Appendix A

The following tables list REIC and REID values for 1-y missions in deep space at solar minimum for 20 g/cm^2 of aluminum shielding. Calculations for the average U.S. and never-smoker populations are listed.

Table A1. %REIC for average U.S. males vs. age at exposure (y).

Tissue	30	35	40	45	50	55	60
Stomach	0.357	0.344	0.327	0.306	0.281	0.252	0.218
Colon	0.616	0.564	0.515	0.464	0.41	0.351	0.285
Liver	0.153	0.15	0.146	0.14	0.131	0.121	0.108
Lung	0.783	0.782	0.775	0.761	0.735	0.693	0.63
Prostate	0.312	0.309	0.302	0.29	0.272	0.246	0.211
Bladder	0.682	0.687	0.69	0.692	0.687	0.671	0.631
Esophagus	0.114	0.114	0.113	0.111	0.106	0.099	0.088
Brain-CNS	0.064	0.056	0.048	0.041	0.035	0.029	0.023
Thyroid	0.07	0.044	0.027	0.016	0.009	0.005	0.003
Oral Cavity	0.026	0.023	0.02	0.018	0.015	0.013	0.01
Remainder	0.659	0.544	0.445	0.36	0.286	0.222	0.166
Leukemia	0.71	0.682	0.652	0.617	0.576	0.528	0.471
Total Solid	3.836	3.616	3.408	3.198	2.968	2.7	2.373
Total	4.547	4.298	4.06	3.816	3.544	3.228	2.844

Table A2. %REIC for never-smoker males vs. age at exposure (y).

Tissue	30	35	40	45	50	55	60
Stomach	0.339	0.327	0.31	0.29	0.266	0.239	0.207
Colon	0.617	0.566	0.516	0.465	0.411	0.352	0.285
Liver	0.153	0.151	0.146	0.14	0.132	0.121	0.108
Lung	0.349	0.348	0.345	0.339	0.331	0.319	0.3
Prostate	0.313	0.309	0.303	0.291	0.273	0.246	0.212
Bladder	0.406	0.408	0.41	0.411	0.408	0.399	0.377
Esophagus	0.035	0.035	0.034	0.033	0.031	0.029	0.026
Brain-CNS	0.064	0.056	0.048	0.041	0.035	0.029	0.023
Thyroid	0.071	0.044	0.027	0.016	0.009	0.005	0.003
Oral Cavity	0.025	0.022	0.02	0.017	0.015	0.012	0.01
Remainder	0.661	0.545	0.446	0.361	0.287	0.222	0.166
Leukemia	0.711	0.683	0.654	0.619	0.577	0.529	0.472
Total Solid	3.033	2.811	2.605	2.405	2.197	1.973	1.717
Total Cancer	3.745	3.494	3.259	3.023	2.775	2.502	2.189

Table A3. %REIC for average U.S. females vs. age at exposure (y).

Tissue	30	35	40	45	50	55	60
Stomach	0.381	0.367	0.349	0.328	0.303	0.274	0.242
Colon	0.623	0.555	0.495	0.439	0.385	0.331	0.274
Liver	0.125	0.124	0.122	0.119	0.115	0.109	0.1
Lung	2.217	2.207	2.182	2.133	2.049	1.914	1.724
Breast	1.405	1.075	0.813	0.605	0.425	0.292	0.195
Uterus	0.158	0.151	0.141	0.13	0.117	0.102	0.086
Ovary	0.179	0.173	0.164	0.154	0.142	0.128	0.112
Bladder	0.343	0.344	0.344	0.343	0.338	0.329	0.312
Esophagus	0.037	0.037	0.036	0.035	0.034	0.032	0.029
Brain-CNS	0.063	0.055	0.048	0.042	0.036	0.03	0.024
Thyroid	0.409	0.244	0.142	0.08	0.044	0.023	0.012
Oral Cavity	0.03	0.027	0.024	0.021	0.018	0.015	0.013
Remainder	0.814	0.656	0.522	0.41	0.317	0.239	0.175
Leukemia	0.459	0.441	0.424	0.405	0.38	0.349	0.312
Total Solid	6.785	6.014	5.382	4.839	4.322	3.82	3.299
Total	7.244	6.455	5.806	5.244	4.702	4.168	3.611

Table A4. %REIC for never-smoker females vs. age at exposure (y).

Tissue	30	35	40	45	50	55	60
Stomach	0.378	0.364	0.346	0.325	0.301	0.272	0.24
Colon	0.627	0.559	0.498	0.442	0.388	0.333	0.276
Liver	0.126	0.125	0.123	0.12	0.116	0.11	0.101
Lung	0.808	0.805	0.797	0.784	0.763	0.731	0.686
Breast	1.413	1.081	0.817	0.608	0.427	0.294	0.196
Uterus	0.159	0.151	0.142	0.131	0.117	0.102	0.087
Ovary	0.18	0.174	0.165	0.155	0.143	0.129	0.113
Bladder	0.284	0.285	0.285	0.284	0.281	0.274	0.261
Esophagus	0.018	0.017	0.016	0.016	0.015	0.013	0.012
Brain-CNS	0.063	0.055	0.048	0.042	0.036	0.03	0.024
Thyroid	0.41	0.245	0.142	0.08	0.044	0.023	0.012
Oral Cavity	0.03	0.027	0.024	0.021	0.018	0.015	0.013
Remainder	0.818	0.659	0.525	0.412	0.319	0.241	0.176
Leukemia	0.461	0.443	0.426	0.406	0.381	0.35	0.313
Total Solid	5.314	4.547	3.93	3.42	2.967	2.568	2.196
Total	5.774	4.99	4.356	3.827	3.348	2.918	2.51

Table A5. %REID for average U.S. males vs. age at exposure (y).

Tissue	30	35	40	45	50	55	60
Stomach	0.21	0.201	0.19	0.178	0.165	0.152	0.137
Colon	0.259	0.236	0.215	0.196	0.177	0.156	0.134
Liver	0.125	0.125	0.124	0.121	0.116	0.109	0.1
Lung	0.635	0.638	0.638	0.636	0.628	0.608	0.571
Prostate	0.052	0.052	0.053	0.054	0.055	0.056	0.056
Bladder	0.156	0.157	0.158	0.159	0.16	0.161	0.16
Esophagus	0.107	0.107	0.106	0.104	0.1	0.094	0.085
Brain-CNS	0.05	0.044	0.039	0.034	0.03	0.025	0.02
Thyroid	0.009	0.006	0.004	0.003	0.002	0.001	0.001
Oral Cavity	0.006	0.006	0.005	0.005	0.004	0.004	0.003
Remainder	0.19	0.161	0.135	0.112	0.092	0.074	0.058
Leukemia	0.477	0.469	0.458	0.447	0.432	0.413	0.387
Total Solid	1.799	1.733	1.668	1.602	1.528	1.44	1.325
Total	2.276	2.201	2.127	2.049	1.96	1.854	1.713

Table A6. %REID for never-smoker males vs. age at exposure (y).

Tissue	30	35	40	45	50	55	60
Stomach	0.2	0.191	0.181	0.169	0.157	0.144	0.13
Colon	0.26	0.237	0.216	0.197	0.177	0.157	0.135
Liver	0.125	0.125	0.124	0.121	0.116	0.11	0.101
Lung	0.317	0.315	0.312	0.306	0.296	0.283	0.264
Prostate	0.052	0.053	0.053	0.054	0.055	0.056	0.057
Bladder	0.094	0.095	0.095	0.096	0.096	0.097	0.097
Esophagus	0.033	0.033	0.032	0.031	0.03	0.028	0.025
Brain-CNS	0.05	0.044	0.039	0.034	0.03	0.025	0.02
Thyroid	0.009	0.006	0.004	0.003	0.002	0.001	0.001
Oral Cavity	0.006	0.005	0.005	0.005	0.004	0.004	0.003
Remainder	0.19	0.161	0.135	0.113	0.093	0.075	0.059
Leukemia	0.478	0.47	0.459	0.448	0.433	0.414	0.388
Total Solid	1.336	1.265	1.197	1.128	1.056	0.978	0.89
Total	1.814	1.735	1.656	1.576	1.489	1.393	1.278

Table A7. %REID for average U.S. females vs. age at exposure (y).

Tissue	30	35	40	45	50	55	60
Stomach	0.219	0.213	0.206	0.197	0.187	0.175	0.16
Colon	0.241	0.216	0.194	0.174	0.157	0.14	0.123
Liver	0.113	0.112	0.111	0.109	0.105	0.101	0.094
Lung	1.71	1.709	1.701	1.682	1.641	1.566	1.446
Breast	0.354	0.274	0.21	0.16	0.117	0.085	0.06
Uterus	0.017	0.017	0.016	0.016	0.015	0.014	0.012
Ovary	0.136	0.135	0.133	0.129	0.124	0.115	0.104
Bladder	0.108	0.108	0.108	0.108	0.108	0.108	0.106
Esophagus	0.033	0.032	0.032	0.031	0.03	0.029	0.027
Brain-CNS	0.047	0.043	0.039	0.034	0.03	0.026	0.022
Thyroid	0.023	0.015	0.01	0.007	0.004	0.003	0.002
Oral Cavity	0.007	0.007	0.006	0.006	0.005	0.005	0.004
Remainder	0.293	0.246	0.205	0.169	0.137	0.109	0.084
Leukemia	0.306	0.3	0.293	0.284	0.274	0.261	0.244
Total Solid	3.302	3.127	2.971	2.822	2.661	2.475	2.246
Total	3.608	3.428	3.264	3.106	2.935	2.736	2.49

Table A8. %REID for never-smoker females vs. age at exposure (y).

Tissue	30	35	40	45	50	55	60
Stomach	0.217	0.211	0.204	0.195	0.185	0.173	0.159
Colon	0.243	0.218	0.195	0.175	0.158	0.141	0.124
Liver	0.114	0.113	0.112	0.11	0.106	0.102	0.095
Lung	0.676	0.675	0.672	0.665	0.654	0.636	0.606
Breast	0.357	0.276	0.212	0.161	0.118	0.086	0.061
Uterus	0.017	0.017	0.016	0.016	0.015	0.014	0.012
Ovary	0.137	0.136	0.134	0.13	0.125	0.116	0.105
Bladder	0.09	0.091	0.091	0.091	0.091	0.091	0.09
Esophagus	0.015	0.015	0.014	0.014	0.013	0.012	0.011
Brain-CNS	0.047	0.043	0.039	0.035	0.03	0.026	0.022
Thyroid	0.023	0.016	0.01	0.007	0.004	0.003	0.002
Oral Cavity	0.007	0.007	0.006	0.006	0.005	0.005	0.004
Remainder	0.295	0.248	0.206	0.17	0.138	0.11	0.085
Leukemia	0.308	0.302	0.294	0.286	0.275	0.262	0.245
Total Solid	2.24	2.065	1.911	1.774	1.643	1.513	1.375
Total	2.548	2.366	2.206	2.06	1.918	1.776	1.621

Appendix B

Using the methods described in the text, risk calculations were made for each U.S. state and the District of Columbia using the NCRP No. 132 Model (as described in the text) and the BEIR VII model. The following tables show REID results for females and males at ages of exposure of 35, 45, and 55 y. The median life span and age-adjusted cancer mortality rate are also shown.

Table B1. REID per Sv for males at different ages at exposure in NCRP and BEIR VII models**.**

			BEIR VII			NCRP 132		
State	Median lifespan	Cancer rate	35	45	55	35	45	55
Utah	80.2	96.0	3.78	3.69	3.46	3.69	2.85	1.95
North Dakota	79.2	103.8	3.98	3.86	3.64	3.96	3.03	2.05
Colorado	79.7	107.4	3.90	3.80	3.57	3.86	2.97	2.02
Wyoming	78.3	108.2	3.84	3.76	3.54	3.78	2.91	1.96
Alaska	78.4	112.8	4.03	3.93	3.69	4.08	3.13	2.14
Montana	78.5	113.5	3.92	3.85	3.66	3.88	2.97	2.02
Minnesota	80.1	115.0	4.18	4.06	3.84	4.09	3.12	2.11
Idaho	79.2	118.1	4.01	3.90	3.74	3.89	2.98	2.03
Connecticut	79.4	120.8	4.09	3.99	3.75	4.07	3.10	2.10
California	79.4	123.0	3.92	3.81	3.57	3.91	3.00	2.05
Vermont	79.6	123.9	4.08	3.94	3.73	4.02	3.06	2.06
Nebraska	79.0	125.8	3.96	3.85	3.59	3.90	2.96	1.99
New Mexico	78.1	126.0	3.76	3.69	3.48	3.76	2.91	2.01
Washington	79.3	126.5	4.06	3.95	3.73	3.99	3.04	2.07
New Hampshire	79.4	129.1	4.14	4.01	3.76	4.11	3.12	2.10
Wisconsin	78.9	130.6	4.10	3.99	3.76	3.99	3.03	2.04
New Jersey	78.7	132.7	3.99	3.88	3.65	3.97	3.02	2.04
Arizona	78.7	134.2	3.85	3.76	3.55	3.89	2.99	2.06
South Dakota	78.6	135.0	4.03	3.93	3.70	3.96	3.02	2.04
Oregon	78.8	135.9	3.98	3.87	3.63	3.95	3.01	2.04
Iowa	78.9	140.4	4.12	4.01	3.78	3.99	3.02	2.04
Nevada	76.5	140.4	3.70	3.61	3.40	3.68	2.80	1.91
Massachusetts	79.0	141.0	4.06	3.94	3.70	4.06	3.08	2.09
New York	79.1	141.5	3.96	3.84	3.60	3.92	2.99	2.03
Hawaii	80.3	144.5	3.91	3.76	3.53	3.99	3.07	2.11
Kansas	78.2	144.9	3.95	3.84	3.61	3.86	2.93	1.98
Texas	77.4	149.1	3.84	3.73	3.50	3.80	2.89	1.95
Maryland	77.7	150.2	3.89	3.78	3.55	3.90	2.97	2.02
Virginia	77.9	150.6	3.94	3.81	3.55	3.93	2.97	2.00
Illinois	77.8	151.2	3.99	3.88	3.65	3.92	2.97	2.00
Rhode Island	78.5	152.7	4.00	3.86	3.57	4.04	3.06	2.07
Michigan	77.7	157.0	3.90	3.79	3.56	3.84	2.91	1.97
Pennsylvania	77.3	158.8	3.91	3.80	3.56	3.86	2.92	1.96
Indiana	76.8	158.9	3.89	3.79	3.55	3.83	2.89	1.94
Maine	78.3	165.3	4.11	3.98	3.72	4.03	3.04	2.04
Ohio	76.9	168.3	3.87	3.76	3.52	3.83	2.88	1.94
Georgia	76.1	169.1	3.70	3.58	3.34	3.70	2.79	1.88
Delaware	77.4	170.9	3.97	3.88	3.63	3.96	3.00	2.03
Missouri	76.7	171.5	3.88	3.78	3.54	3.81	2.88	1.94
Florida	78.4	174.1	3.99	3.88	3.67	3.95	3.02	2.08
North Carolina	76.5	175.1	3.80	3.68	3.44	3.78	2.85	1.92
Kentucky	75.2	185.1	3.80	3.69	3.45	3.79	2.86	1.91
West Virginia	75.3	185.2	3.69	3.59	3.32	3.66	2.77	1.85
Oklahoma	75.4	187.5	3.66	3.56	3.34	3.60	2.72	1.82
South Carolina	75.5	196.2	3.77	3.66	3.45	3.74	2.82	1.91
Alabama	74.6	196.2	3.64	3.53	3.30	3.63	2.73	1.84
Tennessee	75.2	196.7	3.74	3.64	3.43	3.70	2.79	1.88
Arkansas	75.4	202.0	3.82	3.71	3.49	3.75	2.83	1.91
District of Columbia	73.2	205.0	3.48	3.41	3.29	3.56	2.72	1.90
Louisiana	74.2	212.3	3.67	3.57	3.34	3.68	2.77	1.87
Mississippi	73.7	219.0	3.59	3.49	3.27	3.59	2.70	1.81

Table B2. REID per Sv for females at different ages at exposure in NCRP and BEIR VII models.

			BEIR VII			NCRP 132		
State	Median lifespan	Cancer rate	35	45	55	35	45	55
Alaska	82.6	89.6	5.43	5.26	4.85	4.82	3.62	2.42
Utah	83.1	99.4	4.84	4.64	4.21	4.27	3.22	2.13
Colorado	83.1	108.6	5.34	5.14	4.72	4.72	3.52	2.34
North Dakota	84.0	109.6	5.60	5.40	4.92	4.98	3.72	2.46
Idaho	83.0	111.5	5.45	5.25	4.86	4.71	3.52	2.33
Nebraska	83.2	114.3	5.47	5.27	4.84	4.80	3.58	2.37
Hawaii	85.6	114.4	5.46	5.22	4.76	4.93	3.73	2.50
Minnesota	84.0	117.1	5.74	5.54	5.09	5.04	3.76	2.49
Montana	82.8	117.5	5.50	5.32	4.91	4.85	3.62	2.40
Oregon	82.5	119.7	5.52	5.32	4.87	4.89	3.63	2.40
Connecticut	83.6	120.6	5.69	5.48	5.03	5.05	3.76	2.49
Washington	82.9	120.8	5.58	5.38	4.94	4.94	3.67	2.44
Wyoming	82.2	121.1	5.33	5.16	4.73	4.68	3.50	2.32
California	83.4	123.8	5.46	5.25	4.80	4.84	3.61	2.40
Maine	82.3	123.9	5.65	5.44	4.97	4.97	3.68	2.41
Wisconsin	83.3	126.0	5.61	5.40	4.95	4.91	3.65	2.41
Arizona	83.4	126.3	5.33	5.13	4.70	4.72	3.54	2.36
Vermont	83.3	127.4	5.53	5.31	4.83	4.89	3.63	2.39
New Mexico	83.1	127.5	5.25	5.05	4.62	4.67	3.50	2.33
Texas	82.2	128.8	5.18	4.96	4.52	4.56	3.39	2.24
Massachusetts	83.2	129.0	5.66	5.44	4.98	5.01	3.72	2.45
New Hampshire	83.1	129.2	5.64	5.39	4.92	5.01	3.71	2.45
Nevada	81.5	129.8	5.32	5.13	4.69	4.73	3.51	2.32
South Dakota	83.6	130.2	5.59	5.39	4.92	4.91	3.67	2.43
Rhode Island	83.0	130.7	5.64	5.44	5.00	4.92	3.65	2.41
Iowa	83.4	131.7	5.62	5.41	4.94	4.90	3.65	2.41
Virginia	82.2	135.2	5.37	5.14	4.67	4.74	3.51	2.31
New York	83.3	135.6	5.51	5.29	4.82	4.88	3.63	2.40
New Jersey	82.8	135.6	5.64	5.43	4.96	4.98	3.70	2.44
Kansas	82.4	135.9	5.36	5.15	4.71	4.68	3.48	2.30
Michigan	82.0	138.6	5.37	5.16	4.72	4.70	3.48	2.30
Illinois	82.4	139.5	5.50	5.28	4.82	4.84	3.58	2.36
Maryland	82.2	140.6	5.42	5.20	4.75	4.80	3.56	2.35
Pennsylvania	82.2	140.6	5.46	5.25	4.77	4.81	3.56	2.35
Georgia	81.2	142.7	5.07	4.85	4.41	4.43	3.28	2.16
North Carolina	81.7	143.6	5.18	4.96	4.51	4.56	3.39	2.23
Indiana	81.6	143.7	5.38	5.15	4.68	4.72	3.49	2.29
Missouri	81.7	145.3	5.34	5.12	4.65	4.69	3.47	2.28
Oklahoma	80.7	146.4	5.02	4.81	4.36	4.39	3.25	2.14
Florida	83.7	146.4	5.50	5.29	4.85	4.86	3.64	2.43
Ohio	81.5	147.2	5.36	5.14	4.67	4.70	3.47	2.28
Delaware	82.2	150.0	5.54	5.33	4.85	4.84	3.59	2.37
Alabama	80.5	152.2	4.97	4.77	4.33	4.33	3.21	2.11
West Virginia	80.4	153.1	5.21	5.01	4.54	4.56	3.36	2.19
South Carolina	81.3	154.0	5.11	4.88	4.44	4.50	3.34	2.21
Kentucky	80.8	156.9	5.34	5.13	4.62	4.66	3.43	2.24
Tennessee	80.8	158.6	5.15	4.93	4.48	4.52	3.34	2.20
Louisiana	80.1	161.7	5.10	4.87	4.42	4.48	3.31	2.17
Arkansas	81.3	163.5	5.24	5.02	4.56	4.58	3.39	2.23
Mississippi	80.4	165.1	5.04	4.82	4.38	4.36	3.23	2.13
District of Columbia	81.6	165.6	5.22	5.05	4.72	4.58	3.44	2.33

The CDC[101] has published life-table and cancer mortality rates for different levels of urbanization. We applied these rates using the NCRP No. 132 model with the LSS report solid cancer (DDREF=2) and the BEIR VII model (DDREF=1.5) to study age and gender dependence of REID values (Figures B1 and B2) for different locality as described by the CDC.

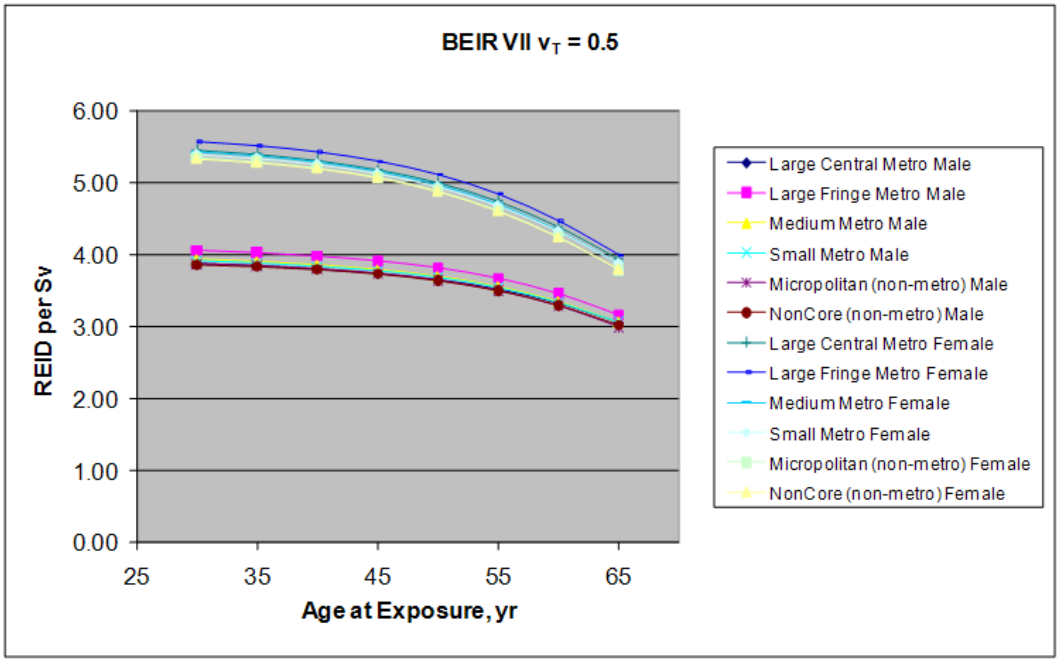

Figure B1. %REID per Sv for males and females in BEIR VII model with v_T=0.5.

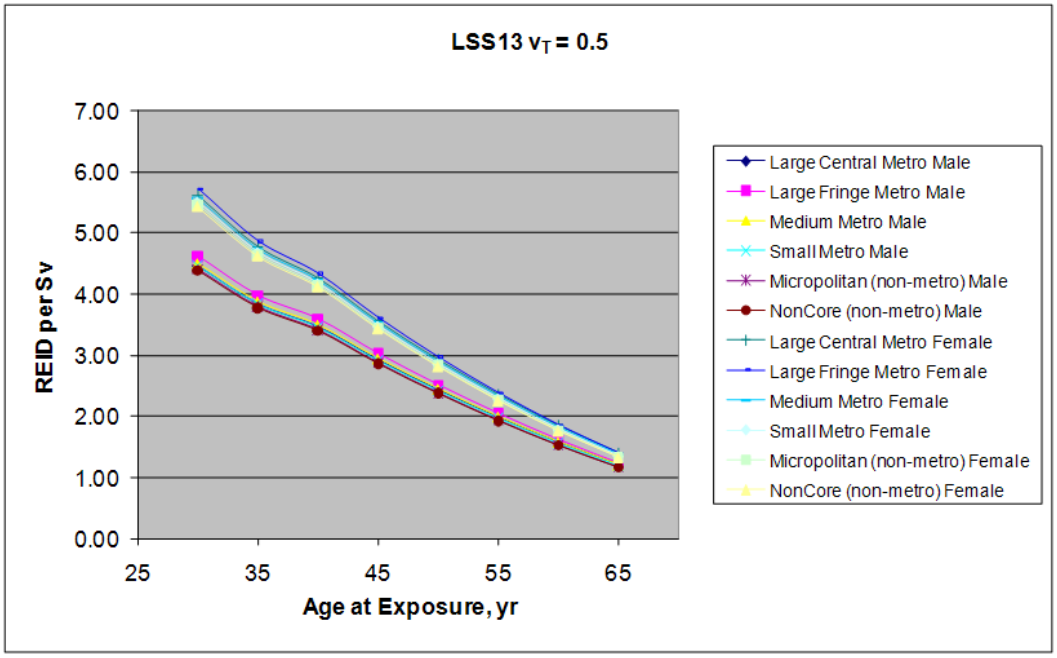

Figure B2. %REID per Sv for males and females in NCRP[6] model with v_T=0.5.